An investigation of evanescent wave gas sensing using Zirconium Fluoride Optical fibre.

by
Simon P. McCabe BSc (Hons)

A thesis presented
to
Dublin City University

For the degree of Doctor of Philosophy.

March 1994

School of Physical Sciences
Dublin City University
Ireland

I hereby certify that this material , which I now submit for assessment on the programme of study leading to the award of Doctor of Philosophy is entirely my own work and has not been taken from the work of others save and to the extent that such work has been cited within the text of my work.

Signed: Simon McCabe Date: 11-3-94

Date:

Acknowledgements

Firstly I want to thank my parents and sisters for all their help through my post graduate years and for never asking why. Special thanks also to Terri who helped me greatly and always kept me smiling.

Thanks to all my fellow postgrads especially those in the optical sensors group. A special thanks to Brian Hurley, Dave Connolly, Kieran O'Dwyer, Dave Farrell and, of course, Liam Roberts and Charles Markham.

What would this thesis be without Dr. Brian MacCraith who has been a lot more than just a supervisor. Thanks Brian, I know you worked almost as much as I did for this. Thanks also to Dr. Vince Ruddy and Dr. Brian Lawless for your many ideas and helpful comments.

Finally thanks to all the academic staff and technicians for their willingness to help with queries and problems.

DON'T PANIC !

'The Hitchhikers Guide to the Galaxy', Douglas Adams

Abstract

A study of zirconium fluoride fibre for evanescent wave gas sensing in the 3 to 4μm region of the optical spectrum is presented. A range of fibre types and methods of evanescent field access is investigated both experimentally and theoretically. The methods of evanescent wave access include side-polishing of all glass monomode, tapering of all glass monomode and the use of porous clad multimode optical fibre. Preparation of zirconium fluoride fibres for sensing requires great care and the polishing and tapering techniques presented are substantially different from those currently used for Silica fibre. A number of experimental systems have been employed, using both broadband and laser sources, with thermoelectrically and liquid nitrogen cooled detectors. side-polished and tapered monomode fibre sensors are shown to have very low sensitivty to gaseous analytes. The use of a novel mid-IR LED source is also reported. The effect of analyte refractive index on evanescent wave sensitivity is discussed. It is shown that the larger the refractive index difference between fibre and analyte the greater the optical mode confinement. This results in a reduced evanescent wave penetration into the analyte. Methods are presented to overcome this mode confinement by use of porous claddings and overlayers. In particular, the use of a teflon clad fibre and sol-gel porous glass structures is proposed. A viable gas sensor based on Teflon clad fibre with a LED source is presented. This evanescent wave gas sensor has a limit of detection per unit length better than 1% propane in air.

Table of Contents

Chapter 1 Introduction

1.1 Optical fibres

Optical information transmission has been used by man for centuries. Through the use of simple tools it became a powerful method of long distance communication especially at sea where there are no obstructions. Early optical communication was unreliable due to the variable quality of the optical transmission medium, air, and the requirement of line of sight operation. The human eye with a maximum frequency response of approximately 30Hz limited the data transfer rate in early optical communication. The telegraph, telephone and radio made possible by the discovery and application of electricity easily supplanted early optical communications and are still in use today. Over the last 25 years optical communication has undergone a renaissance as a direct result of the twin developments of the laser and optical fibre. Optical fibres, the new transmission medium for optical information, provide much lower losses than air and remove the need for line of sight transmission. Modern optical communications use laser diodes to modulate the light at frequencies of 100's of MHz and photodiodes to convert the optical signal to a voltage.

The drawing of silica glasses into optical fibres for communications is a recent development in glass technology. The existence of glass, and in particular silica glass, has been known for many centuries. Figure 1.1 [1] shows the development of glass in terms of its attenuation from the fourth century BC to the present day. The underlying principles of optical fibre transmission have been known for more than a century. The earliest recorded public demonstration of optical guided wave transmission was by John Tyndall in a lecture that he gave at the Royal Society in England in 1870 [2] based on a previously published paper [3]. Tyndall demonstrated the transmission of light along a stream of water flowing from the bottom of an illuminated barrel. The mechanism for

guiding in Tyndall's 'light pipe' experiment is the same as that used in long haul optical fibres today. Guiding occurs because light is totally reflected at the interface between optically transparent dielectric media where there is a difference in their refractive indices. Light is guided in the medium of higher refractive index. Hence water guides light in air and a glass rod will guide light in water.

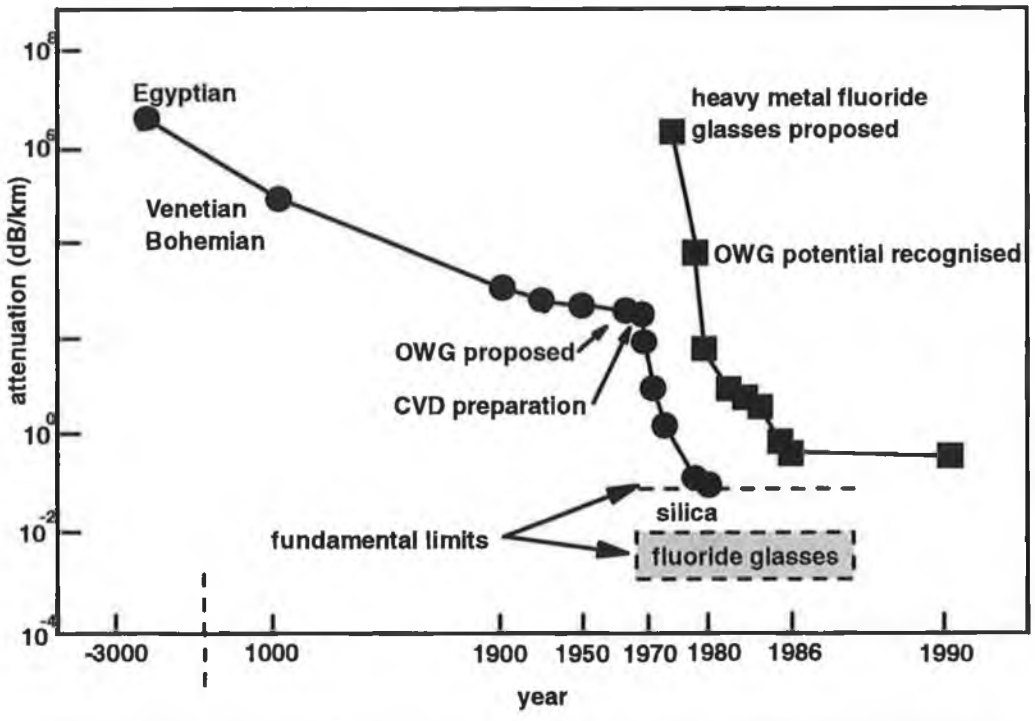

figure 1.1 Attenuation as a function of time in silica and fluoride optical waveguides (from [1]) OWG - optical waveguide.

In 1956 N. S. Kapany coined the term 'fibre optics' and defined it as *"the art of the active and passive guidance of light in the ultraviolet, visible, and infrared regions of the spectrum, along transparent fibres through predetermined paths"*. Fibre optics was not yet perceived as a basis for long haul telecommunications but rather as a method of image transmission over short distances. In 1966 Kao and Hockham [4] published a paper demonstrating low loss optical transmission through glass fibres. In 1968 Kao and Davies [5] suggested the possible use of glass fibres in long haul optical communications based on their studies of ultra low loss glasses. By the early 1970's monomode optical fibres had been manufactured with losses of less than 20 dB/km and in 1979 the intrinsic attenuation limit (0.2dB/km @ 1.55μm) of silica based glass was effectively achieved [6].

1.2 Fluoride Infrared Optical Fibres

The losses in silica optical fibres today are at the fundamental limits defined by material absorption's and Rayleigh Scattering. In the region of operation between the UV and IR material absorption bands losses by Rayleigh scattering dominate. Figure 1.2 shows a plot of the main factors affecting optical fibre attenuation (not including impurities). As impurity concentrations in silica glasses were reduced longer wavelengths of operation became more attractive due to the λ^{-4} dependence of Rayleigh scattering. In silica glasses beyond 1.55 μm the fundamental infrared multi-phonon absorption of the material dominates the losses which increase rapidly with λ. At the same time as the fundamental losses for silica glasses were realised the possibility of achieving lower fundamental losses further into the infrared were being discussed in 1978 by Pinnow *et al.* [7] among others.

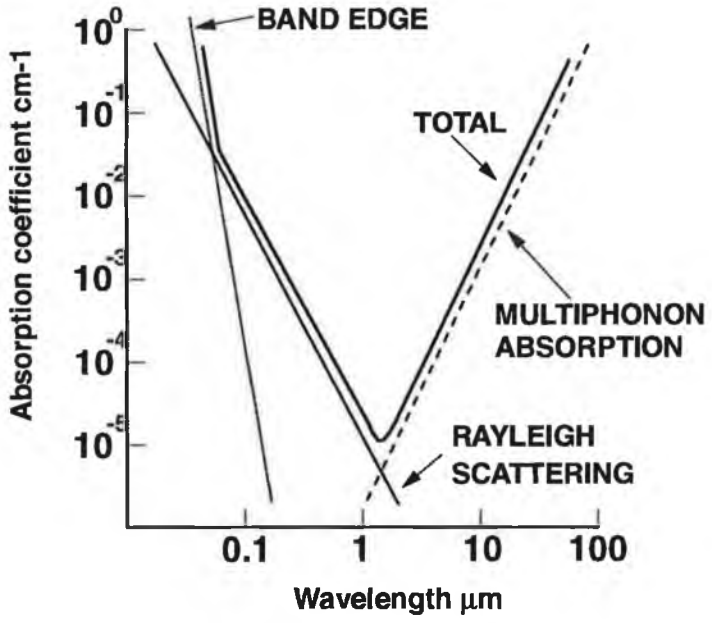

figure 1.2 plot of factors affecting glass attenuation

The principle underlying the concept of lower loss optical fibre is to operate further into the infrared where the scattering losses are smaller. To do this the spectral region at which multi-phonon absorption becomes significant must be shifted to longer

wavelengths. Multi-phonon absorption is caused by the coupling of electromagnetic energy to the dipoles created by the lattice vibrations of the material. The cut-off frequency of the fundamental phonon is given simply by

$$f_o = \frac{1}{2\pi}\left(\frac{F}{\mu}\right)^{1/2} \qquad 1.1$$

where F is the force constant between the atoms of the dipole and μ is the reduced mass of the atoms. Reducing F or increasing μ will therefore move the absorption cut-off to lower frequencies i.e. further into the infrared. To date, the range of materials that have been studied to produce ultra low loss infrared transmitting optical fibre include fluorides, heavy metal oxides, halides and chalcogenides. Of the materials studied, the most promising have been the ZrF_4 based fluoride glasses discovered by M. Poulain *et al.* in 1975 [8]. Losses of less than $1dBkm^{-1}$ have been achieved using fluoride glasses. The loss minimum for fluoride glasses is found in the 2-3 μm spectral region and reasonable losses are obtained out to 4μm.

The research into optical fibres capable of carrying longer wavelengths has led to new application areas. Fibres have been used in medicine for a number of years (for example in endoscopy) and with longer wavelength transmitting fibre it is possible to perform internal surgery with only a small incision using CO_2 lasers operating around 10 μm guided by infrared optical fibre.

1.3 Optical Fibre Sensors

Optical fibres based on silica glasses are firmly established in the telecommunications industry as high throughput transmission channels. In addition optical fibres are being increasingly used as components in optical sensor systems. Optical fibre sensors measure the modulation, caused by a parameter to be measured, which is impressed on the optical signal transmitted by the fibre. Many sensing mechanisms are used and

include, for example, phase and intensity modulation, species-selective absorption losses and Raman scattering. Optical fibres are ideal for sensor systems because they are immune to the large radio frequency and lower frequency electromagnetic interference that are present in industrial environments. In addition, optical fibres provide excellent signal integrity and the low loss transmission properties of silica fibres makes them ideal for remote sensing applications where a long repeaterless signal path is required. Optical fibre sensors may be categorised as intrinsic or extrinsic sensors as shown in figure 1.3 [9]. An extrinsic fibre sensor uses the optical fibre purely as an optical signal carrier and requires coupling optics to mate with the optical sensing device. Such an approach can be used for remote point sensing for example to determine the local O_2 concentration by measuring the fluorescence quenching of a fluorescent dye immobilised on a fibre tip. This would allow a probe to be fabricated to gain access to very small environments. An intrinsic optical fibre sensor is one in which the light is modulated within the fibre by the parameter to be measured. Examples of intrinsic optical fibre sensors include distributed temperature sensors [10,11] which operate by measurement of temperature-induced changes in the local Raman scattering signal, high current sensors using Faraday rotation [12,13] and evanescent wave sensors [14].

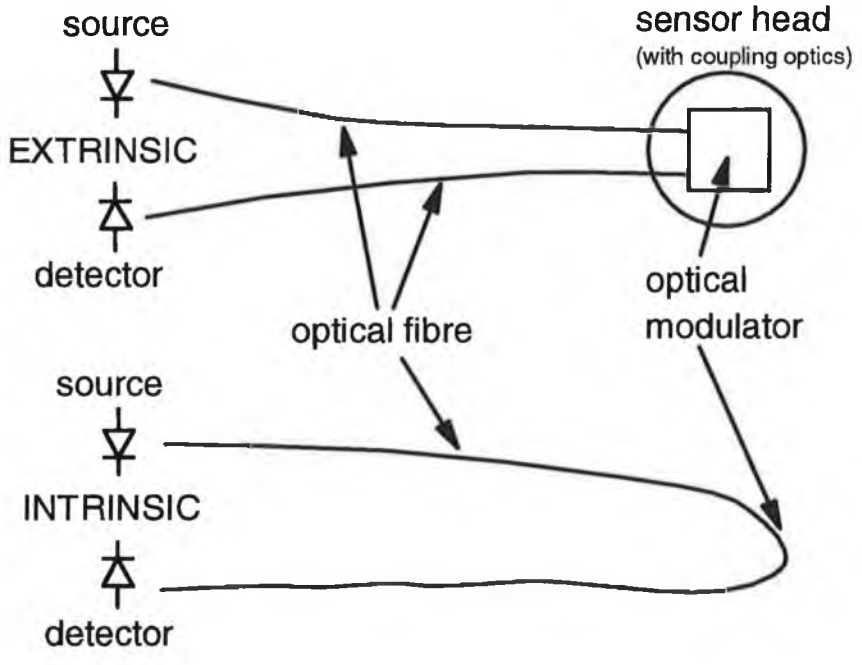

figure 1.3 Extrinsic and intrinsic optical fibre sensors

1.4 Evanescent wave sensing.

At present sensors for flammable gases are usually based on pellistors, which are electrical devices that detect the heat released when the gas is oxidised on a catalyst. These devices are however, susceptable to poisoning, have poor selectivity and require frequent calibration. Remote location of these sensors requires the installation of electrical cables, which can present difficulties in haxardous areas. This thesis examines the potential for an intrinsic form of optical fibre sensing in the mid infrared using zirconium fluoride optical fibre. Optical sensors have a number of attractive features e.g. they are immune to poisoning, potentially more stable and selective. The sensing method investigated is the interaction of the evanescent wave with an absorbing medium (analyte) external to the fibre. This method yields direct spectroscopic information about the analyte. The detected optical carrier is modulated by absorption of the guided light due to the interaction of the evanescent wave with the absorbing species. The species of interest in this work are the flammable hydro-carbon gases, with particular emphasis on Methane, propane and butane. Fluoride optical fibre is used because of the presence of strong absorption bands unique to hydro-carbons in the infrared around a wavelength of 3.4μm. These absorption bands are two orders of magnitude stronger than the related overtones at 1.66μm that are within the low loss window of silica fibres. The absolute minimum performance specification required for a viable sensor is the capability to detect 50% of the lower explosion limit for each gas (e.g.. 2.5% by volume for Methane in air). For critical commercial applications such as the monitoring of offshore installations a limit of detection lower than 1% of the LEL is required [15]. To obtain this performance in an extrinsic sensor of the type depicted in figure 1.3 is not difficult and point sensors of this type are currently used as remote sensors. The most regularly cited advantage of optical fibre sensors for flammable gas detection is their intrinsic safety. However, studies have shown that unfocused optical powers of 290mW are sufficient to ignite methane / air mixtures [16]. While this is well above the power levels to be used in the short term the power levels in future distributed sensors may approach this level.

Evanescent wave gas sensing is investigated in this thesis primarily because of the possibility of developing a fully distributed sensor using this technique. A distributed sensor based on evanescent wave sensing and Optical Time Domain Reflectometry (OTDR) would provide information on gas concentration along the whole of the optical fibres active length as shown in figure 1.4. The use of evanescent wave sensing removes the requirement for coupling optics at the sensing location this gives this type of sensor a distinct advantage over remote sensors that use open path methods.

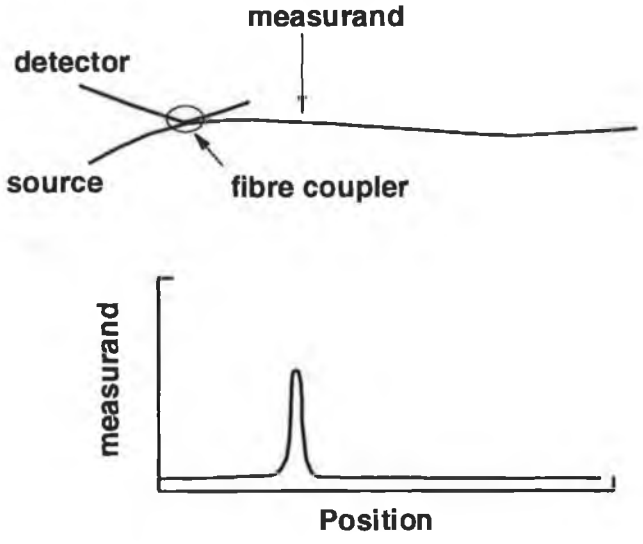

figure 1.4 Distributed optical fibre sensing.

The evanescent wave is not unique to optical fibres and was discovered long before low loss optical fibres were ever manufactured. The evanescent wave is a consequence of total internal reflection and can be generated at the interface between any two dielectric materials. The electric field that decays exponentially with perpendicular displacement from the interface and does not propagate away from the boundary at which it is generated is the evanescent wave.

Newton [17] was one of the first to note the existance of the evanescent field. He observed that total internal reflection in a prism could be frustrated by bringing a second prism close to the point of total reflection. It was not until 1933, however, that a study

of total internal reflection by Taylor [18] discussed the properties of the evanescent wave in detail. Taylor outlined the potential of the evanescent wave for spectroscopic and refractive index measurements. Taylor differentiated between the frustrated total reflection (FTR) observed by Newton and attenuated total reflection (ATR) which is the reduction of the reflected light intensity as a result of absorption in the rarer medium. Taylor discussed the use of ATR spectroscopy for measuring absorption coefficients and obtaining absorption spectra.

It was not until 1960 that Harrick [19] reported the practical use of the evanescent wave as a spectroscopic tool. Research similar to that of Harrick was conducted simultaneously by Fahrenfort [20]. Their published work sparked off a flurry of research into ATR spectroscopy which is also known as internal reflection spectroscopy (IRS), and the complementary FTR technique. This culminated in the publication of a book by Harrick [21] in 1967 devoted entirely to the subject of ATR. The book contains both theoretical and practical information for performing evanescent wave spectroscopy using bulk optics employing a single or small number of total reflections.

The sensitivity of ATR spectroscopy is normally much less than conventional direct absorption spectroscopy because the interaction occurs at the point of total internal reflection over a relatively short path length. Increasing the number of interaction points increases the sensitivity of ATR in an analogous way to increasing the path length in direct absorption. Optical fibres and waveguides are ideal for ATR spectroscopy because light propagates by means of total internal reflection with a high number of reflections per unit length. For optical fibre evanescent wave sensing it is necessary to allow the evanescent field access to the absorbing analyte to be detected in the sensing region of the fibre. Analyte absorption can then be measured as a spectroscopic modulation of the received signal. Different methods of evanescent field access are studied in this thesis and quantitative results as well as qualitative discussion of their merits are presented.

1.5 Aims of this work

In this work the application of zirconium fluoride optical fibre to evanescent wave sensing of flammable gases is investigated. The principal aim of the work is to extend current methods of silica fibre based evanescent wave spectroscopy. to zirconium fluoride fibre and to develop and characterise new sensor structures. Theoretical models of evanescent wave sensing are presented and developed to model these structures. Viable evanescent wave sensors for gas sensing must be able to detect gas concentrations lower than the LEL for the gas. Therefore, where a sensor has been fabricated or modelled, it must be tested for viability using this criterion. In addition to the sensitivity criterion the practicality of the sensor fabrication and usefulness as a field device must be assessed.

1. Drexhage M.: '**The limits of fibre transparency**', Physics World, March1991, pp. 25-6

2. Boyd W.T.: '**Fiber Optics, Communications, Experiments & Projects**', Howard W. Sams & Co., Inc. U.S.A. 1982

3. Tyndall J.: '**On some phenomena connected with the motion of liquids**', Proceedings Royal Institute 1854, Vol. 1, p. 446

4. Kao C. K., Hockham G. A.: '**Dielectric fibre surface waveguides for optical frequencies**', Proc IEE, 1966, Vol. 113, p. 1151

5. Kao K. C., Davies T. W.: '**Spectrophotometric studies of ultra low loss optical glasses**', Journal Scientific Instruments (J Phys E) 1968 Series 2, Vol. 1, p. 1063

6. Miya T., Terunuma Y., Hosaka T., Miyashita T.: '**Ultimate low-loss single mode fibre at 1.55μm**', Electronics Letters 1979, Vol. 15, pp. 106-108

7. Pinnow D. A., Gentile A. L., Syandlee A. G., Timper A. J., Hobrock L. M.:'**Polycrystalline fiber optical waveguides for infrared transmission**', Applied Physics Letters, Vol. 33, pp. 28-9

8. Puolain M., Lucas J., Brun P.: '**Fluorated glass from zirconium tetrafluoride - optical properties of a doped glass in ND3+**', Materials Research Bulletin 1975, Vol. 10, No. 4, pp. 243-6

9. Culshaw B.: '**Optical fibre sensing and signal processing**', IEE 1984.

10. Dakin J.P., Pratt D.J., Bibby E.W., Ross J.N.: '**Distributed optical fibre Raman temperature sensor using a semiconductor light source and detector**', Electronics Letters, 1985, Vol. 21, NO. 13, pp. 569-570

11. Paton A.T., Scott J.C.: '**UV optical fibre distributed temperature sensor**', Proceedings SPIE, 1991, Fibre Optic and Laser Sensors VIII, Vol. 1367, pp. 274-281

12. Smith A.M., '**Polarization and magnetooptic properties of single mode optical fibre**', Applied Optics, 1978, Vol. 17, pp. 52-56

13. Dandridge A., Tveten A.B., Sigel G.H., West E.J., Giallorenzi T.G.: '**Optical fibre magnetic field sensor**', Electronics Letters, 1980, Vol. 16, pp. 408-409

14. Falco L., Berthou H., Cochet H., Scheja B., Parriaux O.: '**Temperature sensor using single mode fiber evanescent field absorption**', Proceedings SPIE 1985, Fiber Optic Sensors, Vol. 586, pp. 114-119

15. Pruss D.: '**Applications of IR-fibers in remote gas-spectroscopy**', Proceedings SPIE, 1987, New Materials for Optical Waveguides, Vol. 799, pp. 117-122

16. Hills P.C.: '**Intrinsic safety of optical fibers in combustible environments**', Electronics Letters, 1990, Vol. 26, No. 23, pp. 1982-3

17. Newton I.: '**Optiks II, Book 8**', 1817, p. 97

18. Taylor A. M., et al: '**Studies in refractive index I and II**', Journal of the Optical Society of America, 1933, Vol. 23, p. 202

19. Harrick N. J.: '**Surface Chemistry from Spectral analysis of totally internally reflected radiation**', Journal Physical Chemistry, 1960, Vol. 64, p. 1110

20. Fahrenfort J.: '**Attenuated Total Reflection: A new principal for the production of of useful infrared reflection spectra of organic compounds**', Spectrochimica Acta, 1962, pp. 698

21. Harrick N.J.: '**Internal Reflection Spectroscopy**', Harrick Scientific, 1985.

Chapter 2 Evanescent Wave Theory

2.1 Introduction

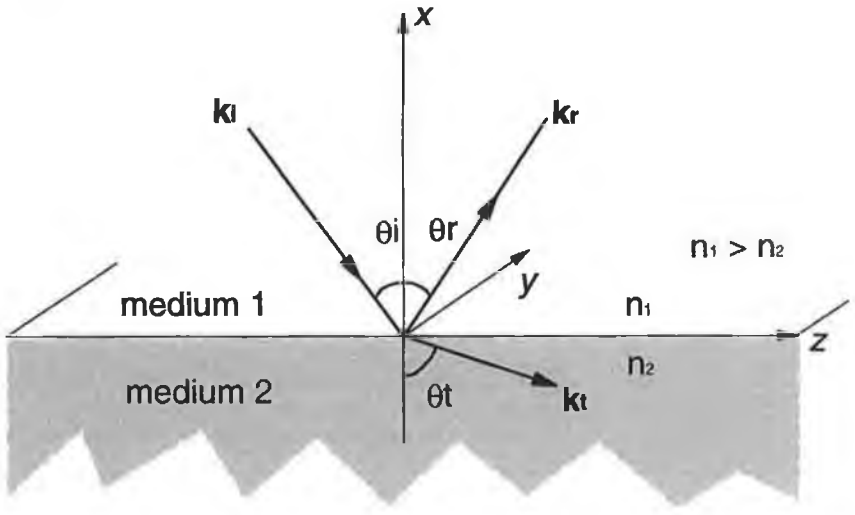

figure 2.1 Refraction and reflection at a dielectric interface

When an electromagnetic wave strikes the boundary between dielectric media of different refractive indices, n_1 and n_2, the wavefront is both reflected from and transmitted across the discontinuity. In order to obtain a mathematical description of what occurs at the interface it is convenient to take the simple case of linear, isotropic, homogenous and nonmagnetic dielectric media. For such media the electric permittivity tensor reduces to the scalar ε and the magnetic permeability has the free space value μ_o. The refractive index n is defined as $\sqrt{\frac{\varepsilon}{\varepsilon_o}}$, where ε_o is the permittivity of free space. Using Maxwell's equations, it can be shown that the tangential components of the E and H fields must be continuous across the boundary between the media [1,2,3,4]. The incident, reflected and transmitted waves as depicted in figure 2.1 may be represented by the following equations where A is the electric field amplitude and k the wave propagation vector:

$$\mathbf{E}_i(\mathbf{r}) = A_i e^{-\iota(\mathbf{k}_i \bullet \mathbf{r})} \quad 2.1$$

$$\mathbf{E}_r(\mathbf{r}) = A_r e^{-\iota(\mathbf{k}_r \bullet \mathbf{r})} \quad 2.2$$

$$\mathbf{E}_t(\mathbf{r}) = A_t e^{-\iota(\mathbf{k}_t \bullet \mathbf{r})} \quad 2.3$$

Each wave propagation vector may be split into its cartesian components k_x,k_y and k_z where x,y and z are orientated as in figure 2.1. The surface boundary is defined as the yz plane at x=0. Without loss of generality, the incident wave may be limited to the xz plane such that k_y=0. Application of the boundary condition for the tangential ***E*** field requires

$$A_i e^{-\iota k_{iz} z} + A_r e^{-\iota k_{rz} z} = A_t e^{-\iota k_{tz} z} \quad 2.4$$

As this equation must be satisfied for all z, a nontrivial solution requires that the propagation vectors k_{iz}, k_{rz}, and k_{tz} must be equal. The z components of the propagation vectors may be rewritten in terms of the angles they make with respect to the surface normal, which in this case is the x direction. Using the relation $k_m = 2\pi n_m/\lambda_0$ where k_m is the plane wave propagation constant in medium m, n_m is the refractive index of the medium and the subscript m denotes medium 1 or 2.

$$k_{iz} = k_1 \sin(\theta_i) \quad 2.5$$

$$k_{rz} = k_1 \sin(\theta_r) \quad 2.6$$

$$k_{tz} = k_2 \sin(\theta_t) \quad 2.7$$

Using $k_{iz} = k_{rz} = k_{tz}$ a number of important relationships may be derived. Firstly

$$\theta_i = \theta_r. \quad 2.8$$

i.e. the reflected and incident angles measured with respect to the normal are equal. Further, using the relation $k_m = 2\pi n_m/\lambda_0$ and equating equations 2.6 and 2.7, it can be shown that

$$n_1 \sin(\theta_i) = n_2 \sin(\theta_t) \qquad 2.9$$

which is commonly known as Snell's law.

To obtain values for the electric field amplitude coefficients (A) the arbitrarily polarised wave is reduced to orthogonal transverse electric (TE) and transverse magnetic (TM) components. TE and TM waves have respectively their electric and magnetic fields polarised perpendicular to the plane of incidence. The continuity condition for fields tangential to the boundary and the curl relationship between $\boldsymbol{E}$ and $\boldsymbol{H}$ gives relationships (the Fresnel equations) for the relative field amplitudes [5]

$$\mathbf{R}^{TE} = \frac{1-(k_{tx}/k_{ix})}{1+(k_{tx}/k_{ix})} \; ; \; \mathbf{R}^{TM} = \frac{1-(n_1/n_2)^2(k_{tx}/k_{ix})}{1+(n_1/n_2)^2(k_{tx}/k_{ix})} \qquad 2.10$$

$$\mathbf{T}^{TE} = \frac{2}{1+(k_{tx}/k_{ix})} \; ; \; \mathbf{T}^{TM} = \frac{2}{1+(n_1/n_2)^2(k_{tx}/k_{ix})} \qquad 2.11$$

where $\boldsymbol{R}$ is the amplitude reflection coefficient and $\boldsymbol{T}$ the amplitude transmission coefficient and

$$\frac{k_{tx}}{k_{ix}} = \sqrt{\frac{(n_2/n_1)^2 - \sin^2(\theta_i)}{1-\sin^2(\theta_i)}} \qquad 2.12$$

Equation 2.12 is essential for an undertstanding of total internal reflection and evanescent waves. The equation describes the relationship between the components of the incident and reflected propagation vectors in the direction normal to the dielectric

interface. The equation depends on the ratio of the refractive indices of the two media and the angle of incidence of the wave. If the ratio (k_{tx}/k_{ix}) is real the wave propagates across the boundary. In the case of total internal reflection, $R^{TE} = R^{TM} = 1$, and equation 2.10 implies that the solution of equation 2.12 must be zero or imaginary. As the denominator of equation 2.12 is positive for all θ_i the numerator determines the conditions for total internal reflection. Because the numerator must be less than or equal to zero for total internal reflection the ratio n_2/n_1 must be less than 1.

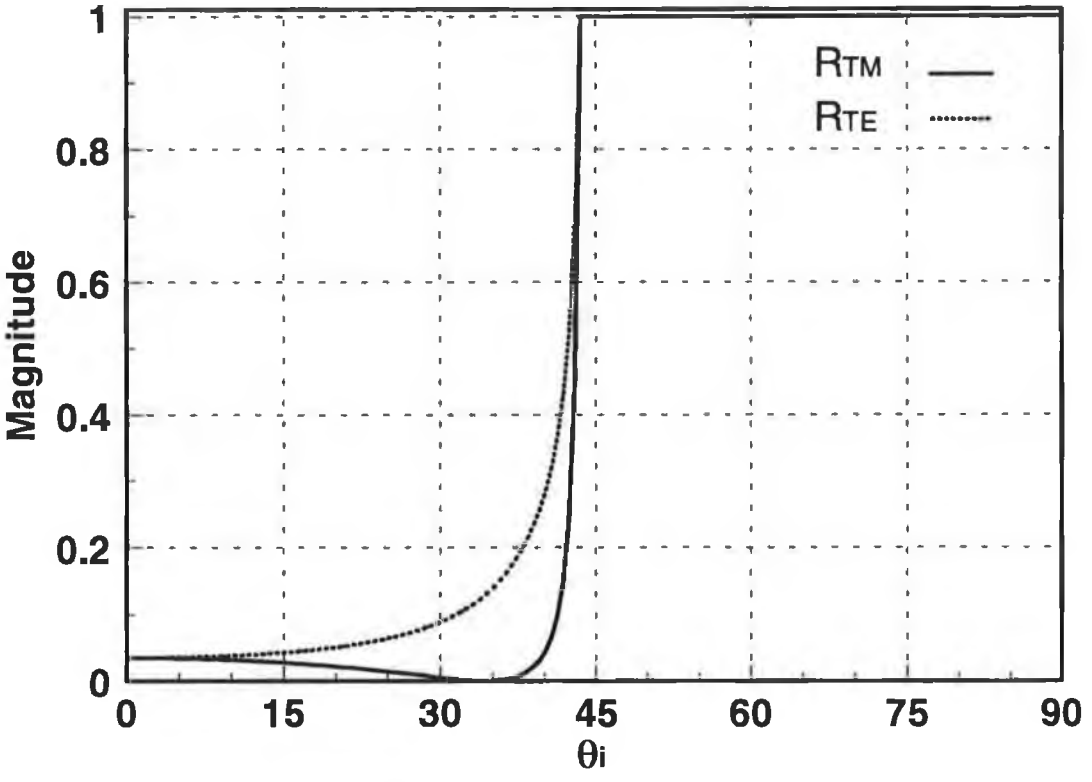

figure 2.2 reflected intensity as a function of incident angle for TE and TM waves.

A plot of the reflected intensities of TE and TM waves travelling from a medium of refractive index n_1 to a medium n_2 where $n_1 > n_2$ clearly shows the phenomenon of total internal reflection. The angle of incidence θ_i at which total internal reflection occurs is called the critical angle (θ_c) and is given by the equality

$$\sin(\theta_c) = \frac{n_2}{n_1} \qquad 2.13$$

At this angle k_{tx} goes to 0 and the values of R^{TE} and R^{TM} in equations 2.10 reduce to (1-0)/(1+0) = 1. At angles of incidence greater than θ_c, the x component of the transmitted propagation constant becomes complex and the transmitted electric field exponentially decays in the x direction. The transmitted wave is evanescent and does not propagate away from the dielectric boundary. The Fresnel equations confirm the experimental observation of total internal reflection and provide a mathematical description of the field in the medium of lower refractive index. This result will now be used to examine the properties of the evanescent wave.

2.2 Evanescent wave

In the previous section, the conditions for total internal reflection and the generation of the evanescent wave were introduced. In this section the evanescent wave will be examined in detail. The equation for the transmitted wave polarised in the xz plane is given by

$$\mathbf{E}_t = A_t e^{i(k_t \bullet \mathbf{r} - \omega t)} , \qquad 2.14$$

where the propagation vector k_t is given by

$$k_t = k_{tz} + k_{tx} = k_t \sin(\theta_t) + k_t \cos(\theta_t) . \qquad 2.15$$

Using Snell's law for refraction, the x and z components of the propagation vector of the transmitted wave can be described in terms of the angle incidence and the refractive indices of media 1 and 2. Thus,

$$k_{tz} = k_t n_{12} \sin(\theta_i) \qquad 2.16$$

$$k_{tx} = k_t \left(1 - n_{12}^2 \sin(\theta_i)\right)^{1/2} \qquad 2.17$$

where $n_{12} = n_1/n_2$ and similarly $n_{21} = n_2/n_1$.

For incident angles θ_i greater than $\sin^{-1}(n_{21})$ the x component, k_{tx}, of the propagation constant is complex and may be written $i\delta$ where δ is real. The transmitted wave electric field is then given by

$$\mathbf{E}_t = A_t \, e^{i(k_{tx}x + k_{tz}z - \omega t)} \qquad 2.18$$

$$\mathbf{E}_t = A_t \, e^{i(k_t n_{12} \sin(\theta_i) z - \omega t)} \, e^{-\delta x} \qquad 2.19$$

where

$$\delta = k_t \left(n_{12}^2 \sin^2(\theta_i) - 1 \right)^{1/2} \qquad 2.20$$

δ can take positive or negative solutions. The solutions are physically constrained such that the product δx is positive; otherwise the field would increase exponentially with distance into the second medium. This solution describes a non-propagating electric field which decays exponentially in medium 2. The exponentially decaying field is called the evanescent field.

An important parameter often used to characterise the evanescent wave is the field penetration depth d_p which is defined as the distance required for the field to drop to e^{-1} of its value at the interface. From equations 2.19 and 2.20

$$d_p = \frac{\lambda_o}{2\pi n_2 \left(n_{12}^2 \sin^2(\theta_i) - 1 \right)^{1/2}} \qquad 2.21$$

where k_t has been written in terms of the free space wavelength (λ_o). The penetration depth is an important parameter for describing evanescent wave interactions as it includes all the factors that determine the strength of such interactions. The factors that determine the penetration depth are (i) the wavelength (λ) of the incident light, (ii) the angle of incidence θ_i of the wave at the dielectric interface and (iii) the refractive indices n_1 and n_2 at the dielectric interface.

2.3 Evanescent Wave Interactions.

2.3.1 Introduction

There are two distinct ways in which perturbation of the evanescent field can result in a reduction in the intensity of the reflected optical power. These are Frustrated Total Reflection (FTR) and Attenuated Total Reflection (ATR).

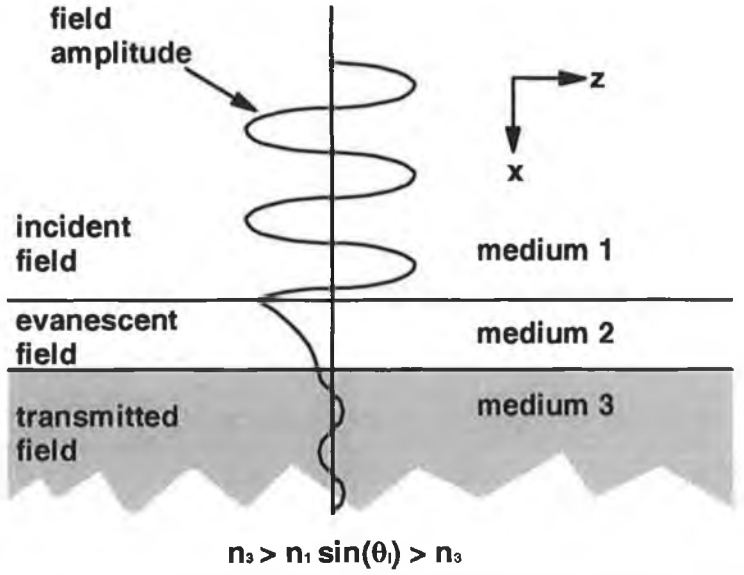

figure 2.3 FTR geometry, only x direction fields are shown

In figure 2.3 the geometry for FTR is depicted. A lossless dielectric (medium 3) with a refractive index n_3 overlaps the exponentially decaying field in medium 2. If $n_3 > n_1$ Sin (θ_i), where θ_i is the angle of incidence of the wavefront, then the evanescent condition is

not met and k_z in medium 3 is real. Therefore the wave propagates in medium 3. This reduces the intensity of the reflected wave by the conservation of energy requirement. The total reflection condition is said to be frustrated. The FTR principle is used in waveguide optical modulation [6] and as a method of coupling light into an optical cavity or waveguide [7]. Optical modulation can be controlled by varying the refractive index or the spacing between two media.

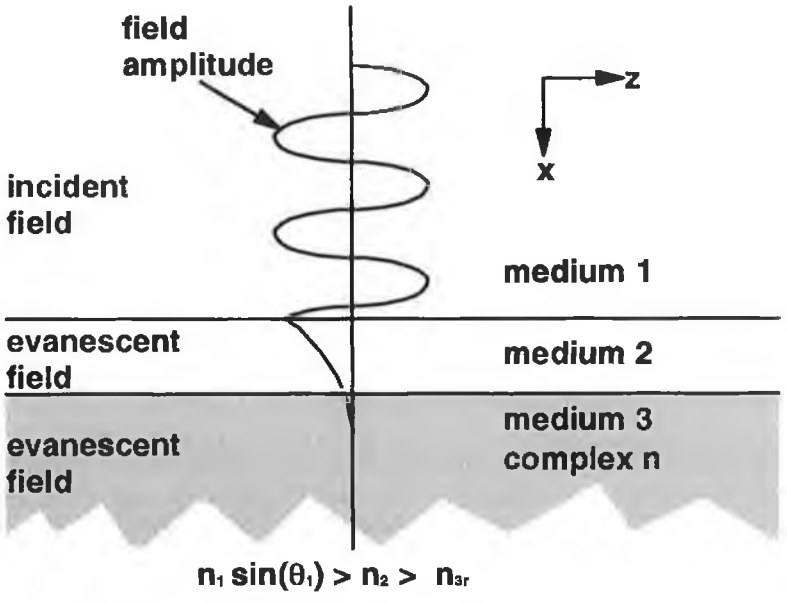

figure 2.4 ATR geometry, only x fields are shown

The ATR configuration shown in figure 2.4 is the same as for FTR except that, in this case the refractive index n_3 is complex with a real component $n_{3r} < n_1 \text{ Sin}(\theta_i)$. Complex refractive indices are used to describe absorbing media. The field in medium 3 is evanescent. The reflected wave is attenuated as the lossy medium absorbs a portion of the optical power through interaction with the evanescent field. Power absorbed is a function of the absorption coefficient of the material[1] and the depth of penetration of the evanescent field into the medium. An absorption spectrum of medium 3 can be recorded using the ATR effect. An ATR or evanescent wave spectrum is obtained by measuring

[1] The absorption coefficient of a medium is related to the complex part of the refractive, n_i, index by the formula $\alpha = 4\pi n_i/\lambda$

the internally reflected light intensity as a function of the incident wavelength. ATR spectroscopy is normally performed with no separating medium 2 as the field in medium 3 in this configuration is also evanescent and the depth of penetration greater without the intervening medium.

ATR is an important addition to the tools available to spectroscopists. Transmission and ATR spectroscopy are complementary techniques that together increase the range of materials that can be analysed. ATR is the method of choice for a range of materials which includes includes highly absorbing liquids, pastes, powders and thin films. For example, the spectra of thin films and liquids in narrow path sample cells taken with transmission instruments often have interference fringes superimposed on the absorption spectrum. Interference fringes do not appear in ATR spectra, thereby making them much simpler to analyse. Pastes and powders require extensive preparation for transmission spectroscopy but for ATR minimal preparation is required. Details of the wide range of applications may be found in Harrick's major work, 'Internal Reflection Spectroscopy' [8].

2.3.2 Effective thickness

Despite the advantages of ATR, transmission spectroscopy remains the most widely used spectroscopic technique for low loss materials. The dominance of transmission spectroscopy in the spectroscopy of low loss materials can be explained by calculating the effective thickness of an absorbing rarer medium in ATR spectroscopy. The effective thickness, d_e, is defined as the thickness of a film of the sample material which would give the same absorbance for transmission at normal incidence as that obtained in a single reflection ATR experiment. Using d_e the reflected ATR intensity is given by

$$I_r = I_o e^{-\alpha d_e} \qquad 2.22$$

The value of d_e for a TE wave is [8]

$$d_e = \frac{n_{21}\lambda\cos(\theta_i)}{\pi\left(1 - n_{21}^2\right)\left(\sin^2(\theta_i) - n_{21}^2\right)^{1/2}} \qquad 2.23$$

There are two ways to increase the effective thickness of an ATR experiment. The simplest is to increase the number of reflections by increasing the length of the cell. If this is not possible (e.g. the cell has a fixed length), then decreasing the angle will increase the number of reflections. This is self defeating as it decreases the absorption per reflection because of the dependance of d_e on angle in equation 2.23. Using angles very close to the critical angle to increase d_e is possible. However at these angles the penetration depth is very wavelength dependent. As an example consider a liquid sample (n = 1.33) and an incident angle approximately 10 degrees away from θ_c where the ATR cell is made from silica glass (n = 1.46). The effective thickness, at a wavelength of 3 μm, for this configuration is approx. 2.6 μm. Transmission spectroscopy in long pass White cells with path lengths in meters are therefore at least 5 to 6 orders of magnitude more sensitive than single reflection ATR.

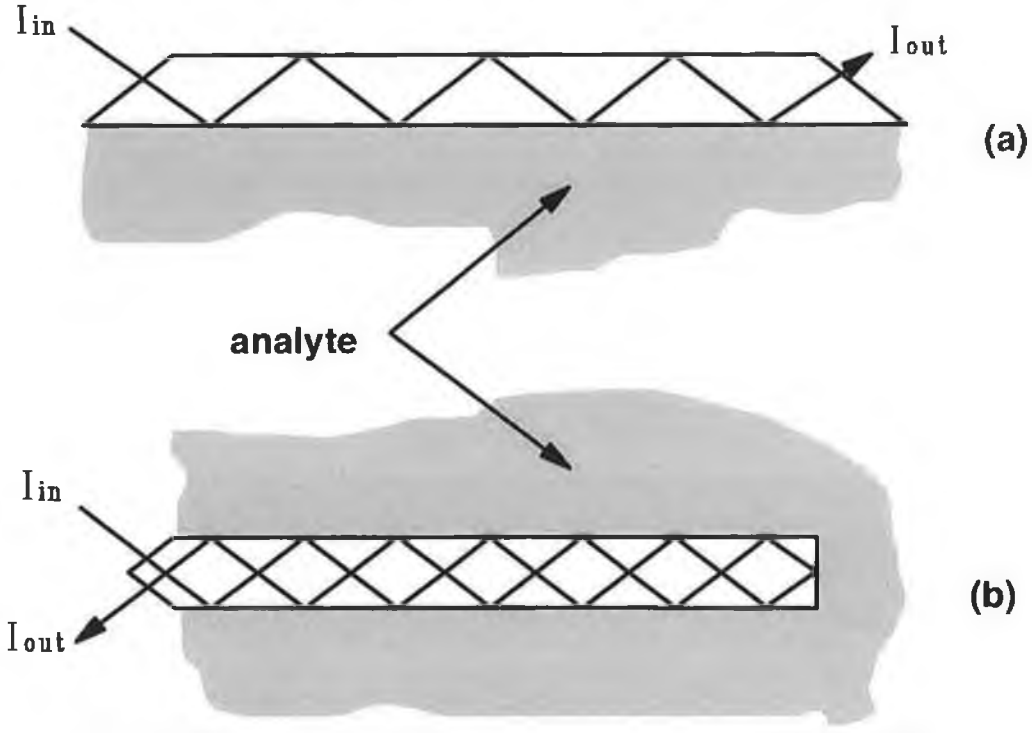

figure 2.5 Simple ATR cells (a) single pass and (b) double pass

The size of the effective thickness of ATR spectroscopy has led to the development of elaborate designs to increase the number of reflections used in an ATR experiment. As each reflection is equally strongly absorbed the total effective thickness for an N reflection ATR cell is Nd_e. A common feature of many ATR cells is that the wave enters the cell at normal incidence. This is to eliminate cell material dispersion effects in the measured spectrum. A number of ATR devices are depicted in figures 2.5 and 2.6 .

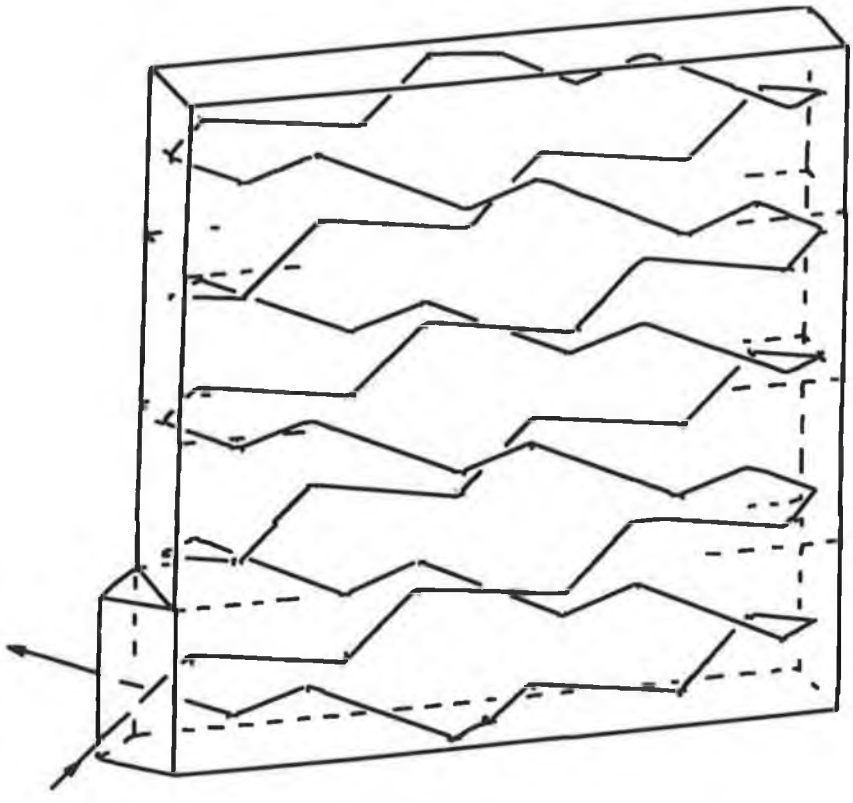

figure 2.6 Folded path multiple pass internal reflection plate for ATR , corner injection type (from Harrick [4])

2.4 Fibre optic evanescent wave spectroscopy.

2.4.1 Introduction

For a given angle and medium, ATR sensitivity is governed by the number of reflections within the interaction length of the device. The sensitivity can be increased by increasing the interaction length and reducing the width of the ATR cell. Reducing the width

increases the number of reflections per unit length. Because they can be of very small width, long length and transmit light by total internal reflection optical fibres are ideal as ATR cells. Optical fibres however are designed specifically for the lossless transmission of electromagnetic radiation. They consist of a low loss glass core surrounded by a low loss glass cladding of lower refractive index as shown in figure 2.7. The cladding diameter is determined by the extent of the evanescent field penetration such that the guided light sees an essentially infinite lossless medium. By removing some or all of the cladding and replacing it with an absorbing material the guided light may be attenuated. This is analogous to the situation in figure 2.4. In this way fibre-based ATR spectroscopy may be performed. Methods used to prepare fibre waveguides for ATR spectroscopy can be divided into two basic groups. The first involves total or partial removal of the cladding to expose the evanescent field; in this case the core is left unaltered. The second is called waveguide modification because both the core and cladding are modified e.g. fibre tapers. These methods are outlined in detail in the following sections. In addition, the design of new fibre structures for ATR spectroscopy is discussed. These do not require any further modification after they have been pulled from a preform.

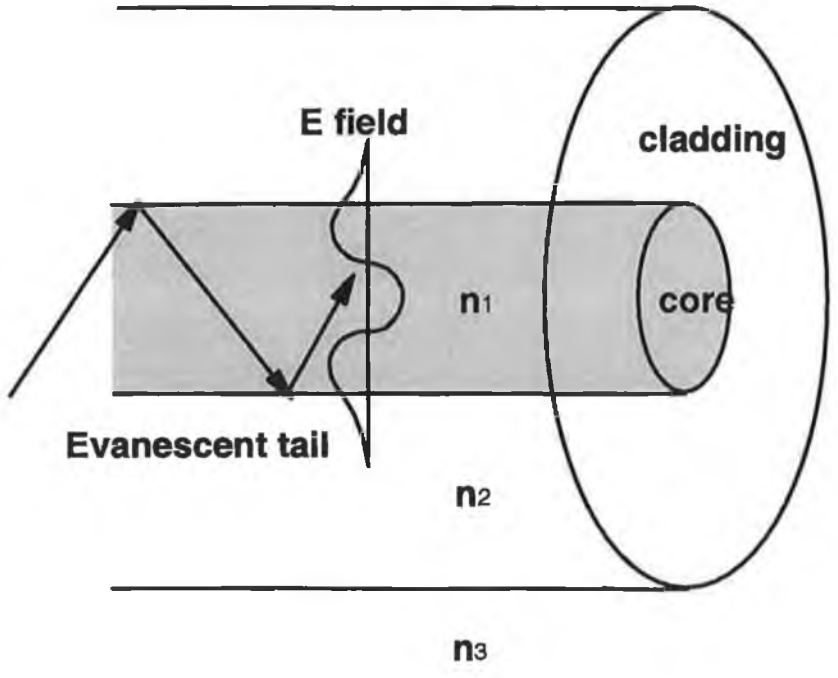

figure 2.7 fibre structure showing propagation by total internal reflection and a typical electric field amplitude

2.4.2 Cladding removal.

Cladding removal can be performed either mechanically or chemically. Mechanical cladding removal normally involves a simple polishing and lapping procedure that requires care because it is very easy to polish into the core of the fibre if it is not continuously monitored. This method is normally used in the manufacture of tunable fibre couplers which operate using the FTR effect [9,10]. The structure of a typical side-polished fibre is shown in figure 2.8. Devices made in this fashion are very robust and this is an important consideration for any device with practical applications. They are, however, difficult to model mathematically because of the non-uniform cladding thickness and fibre curvature. A disadvantage of this type of device is the short interaction length which is equivalent to a short effective path length.

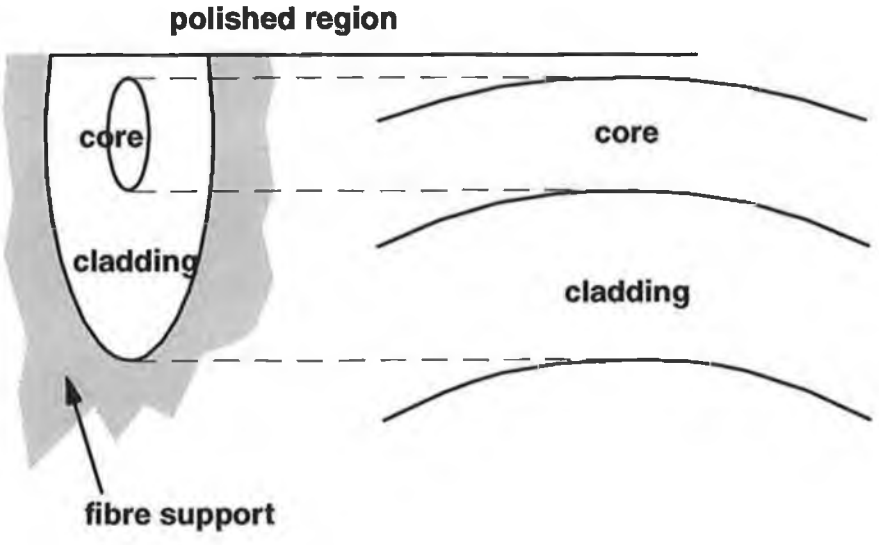

figure 2.8 cross section of polished fibre

2.4.3 Waveguide Modification.

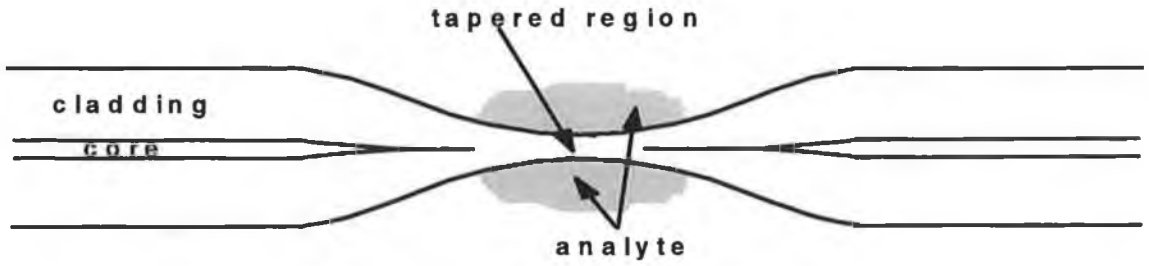

figure 2.9 fibre taper as an evanescent wave sensor

Modification of the structure of a waveguide may be used to enhance evanescent wave interactions. One method is fibre tapering as shown in figure 2.9 . In this case the diameter of the optical fibre is 'tapered' to the point where the core no longer guides and the evanescent field is forced out of the cladding. If the taper is fabricated accurately the light is recaptured by the core on the other side of the tapered region and delivered to a detector. In the tapered region the untapered fibre cladding can now be viewed as the core of the guide and the analyte is the cladding. Silica fibre tapers are commonly fused together to form fixed ratio couplers in the telecommunications industry [11]. ATR devices have already been demonstrated using silica [12] and infrared [13] fibre tapers. In this thesis methods for tapering zirconium fluoride fibres are investigated.

ATR spectroscopy using fibres with porous claddings is also investigated. An example of such a device is Teflon-clad fibre. Teflon is a gas permeable material that allows gaseous analytes to diffuse into the cladding and to interact with the evanescent wave. Teflon is not an ideal cladding material, however, because it absorbs strongly in the infra-red making long lengths of the fibre impractical. A localised sensor of this type may be made using sol-gel-derived porous claddings. To do this the cladding is removed from a section of a fibre and replaced with a microporous glass made by the sol-gel

process. The reason for using sol-gels is a result of early experiments on polished sensors and is explained in section 6.2.

2.5 Fibre ATR sensitivity

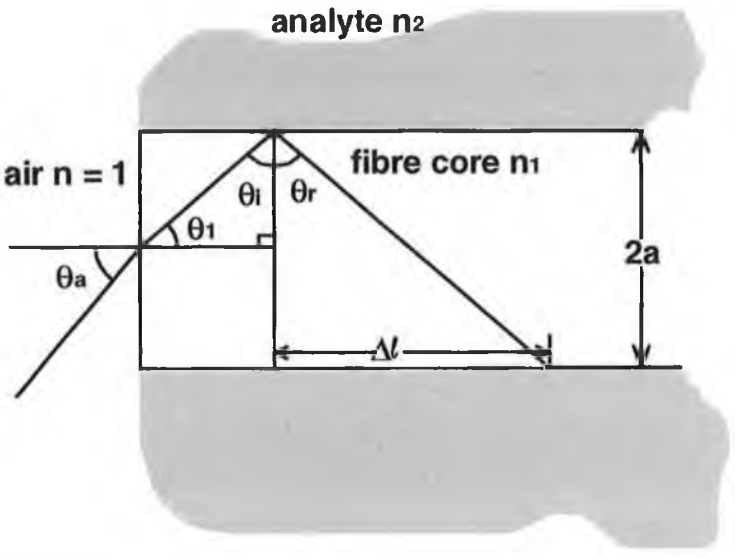

figure 2.10 Core only optical fibre. The analyte is in direct contact with the core.

The sensitivity of fibre ATR devices may be examined using the simple geometry of figure 2.10. For simplicity the cladding is assumed to be completely removed. The interaction length is L and the number of reflections is L/Δl given by

$$N = \frac{L}{2a\tan(\theta_i)} \qquad 2.24$$

where a is the fibre radius.

The absorption of the wave over the interaction length L may be calculated using $I = I_o\exp(-N\alpha d_e)$ where I_o is the intensity transmitted in the absence of absorption and d_e is the effective depth defined in equation 2.23. Thus,

$$I = I_o \exp\left[-\alpha \frac{L\lambda n_{21}}{2\pi n_1 a\left(1-n_{21}^2\right)} \frac{\cos^2(\theta_i)}{\sin(\theta_i)\left(sin^2(\theta_i)-n_{21}^2\right)^{1/2}}\right] \quad 2.25$$

The launched angle θ_a is related to the angle θ_i by the formula

$$\theta_i = 90 - \sin^{-1}\left(\frac{n_a}{n_1}\sin(\theta_a)\right) \quad 2.26$$

where n_a is the refractive index of the medium at the fibre launch interface, normally air.

The sensitivity of a fibre ATR device is a monotonically increasing function of the launch angle θ_a. The sine of the launched angle is used when describing optical fibre launch conditions. The sine of the maximum launched angle that will propagate along a fibre defines the fibre numerical aperture. In figure 2.11 the loss due to evanescent wave absorption for an interaction length of 20 cm is plotted against the sine of the launched angle. The parameters for the plot are:

- n_1 = 1.5 (Zirconium Fluoride glass @ 3.4μm)
- n_2 = 1.376 (Teflon Cladding)
- n_a = 1.00 (Absorbing gas)
- λ = 3.4 x 10^{-6}m (Approx. λ of HeNe laser)
- a = 100 x 10^{-6}m
- L = 0.2 m
- α = 443 m^{-1} atm^{-1} (Propane absorption x 0.42 @ 3.4μm approx.)

These parameters are valid for a Teflon-clad fibre with a cladding pore volume of 42% in a propane gas atmosphere and are used to indicate the dependence of fibre ATR sensitivity on launch numerical aperture.

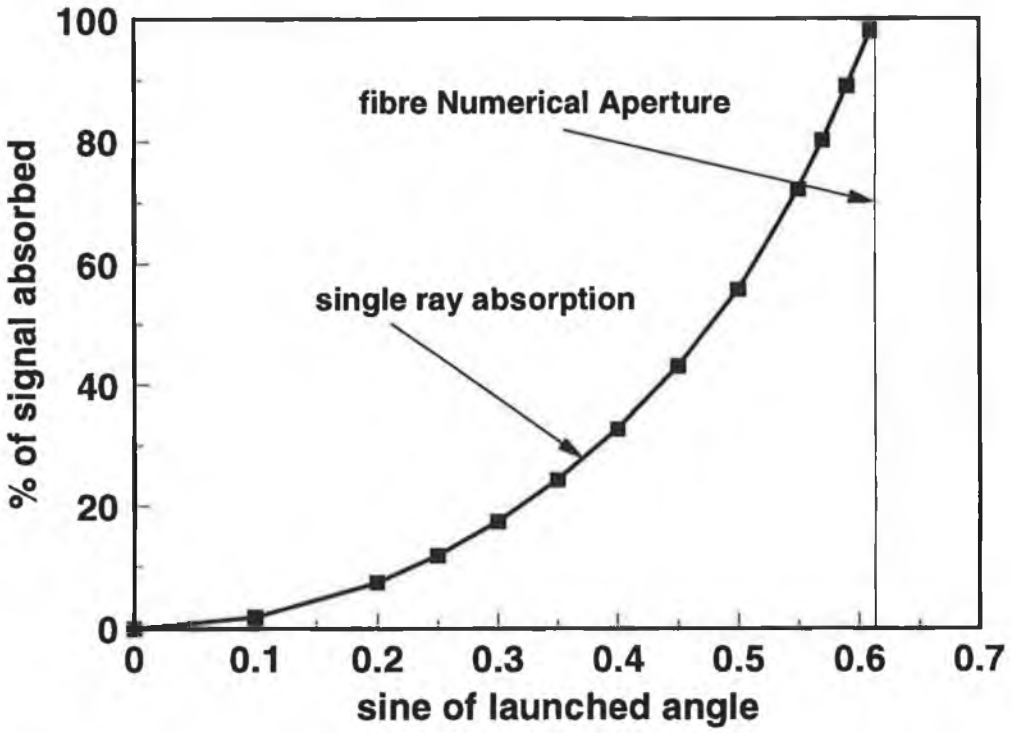

figure 2.11 fibre sensitivity as a function of launch angle expressed as numerical aperture

2.6 Conclusion

The concept of evanescent wave spectroscopy, more correctly termed attenuated total reflection spectroscopy, has been introduced. The role that optical fibres can play as ATR devices has been detailed with the geometrical and optical parameters that influence ATR sensitivity. In the next chapter the link between ATR absorption theory and a modal analysis of waveguides will be established.

1. Wangsness R. K.: '**Electromagnetic Fields**', 1979 John Wiley & Sons, Chapter 25
2. Unger H. G.: '**Planar Optical Waveguides and Fibres**', 1980 Oxford University Press, Chapter 1
3. Tamir T.: '**Guided-Wave Optoelectronics**', 1990 Springer-Verlag, Chapter 2
4. Harrick N. J.: '**Internal Reflection Spectroscopy**', 1985 Harrick Scientific Corporation, Chapter 2
5. Lee D. L.: '**Electromagnetic Principles of Integrated Optics**', 1986 John Wiley & Sons, Chapter 3
6. Wilkonson M., Hill J. R., Cassidy S. A.:'**Optical fibre modulator using electro-optic polymer overlay**', Electronics Letters, 1991, Vol. 27, No. 11, pp. 979-981
7. Berz F.: '**On A Quarter Wave Light Condenser**', British Journal of Applied Physics 1965, Vol. 16, p. 1733
8. Harrick N. J.: '**Internal Reflection Spectroscopy**', 1985 Harrick Scientific corporation Chapter 7
9. Digonnet M., Shaw H.: '**Analysis of a tunable single-mode optical fiber coupler**', IEEE Journal Quantum Electronics, 1982, Vol. 18, pp. 746-754
10. Zafirova B.S., Panajotov K.P., Andreev A.TZ.: '**Temperature-stable polished fibre-optic coupler**', Optics & Laser Technology, 1992, Vol. 24, No. 6, pp. 345-7
11. Baker D.G.: '**Monomode fibre-optic design (with local-area and long haul network applications**', Van Nostrand Reinhold Company, New York, 1987
12. Tai H., Tanaka H., Yoshino T.: '**Fibre-optic evanescent-wave methane-gas sensor using optical absorption for the 3.392-μm line of a HeNe laser**', Optics Letters, 1987, Vol. 12, No. 6, pp. 437-9
13. Bornstein A., Katz M., Baram A., Wolfman D.: '**Attenuated total reflection spectroscopy with chalcogenide bi-tapered fibers**', Proceedings SPIE, 1991, Infrared Fiber Optics III, Vol. 1591 pp. 256-262

Chapter 3 Waveguide Theory

3.1 Introduction

In chapter 2 optical fibre ATR spectroscopy was introduced. A simple ray model of electromagnetic wave propagation in optical fibres was developed to evaluate fibre sensitivity as an ATR probe. The model shows the dependence of sensitivity on the ray angle launched, the length of the fibre interaction region, and the refractive index of the analyte. In section 2.5 ATR absorption was quoted in terms of the effective thickness d_e, the analyte absorption coefficient α and the number of total reflections N in an interaction length L.

In this chapter waveguide sensitivity is analysed by solving Maxwell's equations for various waveguide structures. Solutions obtained using Maxwell's equations are essential for waveguides of small dimension for which the approximations of geometric optics are no longer valid [1]. Solutions to Maxwells equations for waveguide structures consist of a series of discrete guided field distributions or modes. Individual modes are described using the modal propagation constant β. The modal propagation constant provides a conceptual link between the modal analysis to be presented and the geometrical analysis of chapter 2. In figure 3.1 the relationship between the plane wave propagation constant and the modal propagation constant is shown. The angle θ is analogous to the ray propagation angle in the geometric

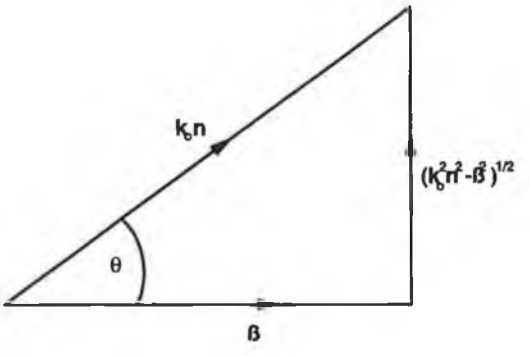

figure 3.1 Modal propagation constant β vs propagation angle

analysis. β is related to the ray propagation angle θ by the equation $\beta = k_o n_{core} \cos(\theta)$. For a guided mode β must lie between the plane wave propagation constants for the fibre core and cladding i.e. $k_o n_{cladding} < \beta < k_o n_{core}$. Another unique way of defining the propagation characteristics of a mode is to use the effective refractive index n_{eff} . The effective refractive index is obtained from the relationship $\beta = k_o n_{eff}$. For a guided mode n_{eff} must lie between n_{core} and $n_{cladding}$.

β contains all the information necessary to describe a mode including modal losses due to evanescent field interactions. The losses can be calculated explicitly using the complex representation of the refractive index of absorbing media (discussed in Chapter 2 section 2.3). The propagation constant of an electromagnetic wave in a medium of complex refractive index is itself complex. A propagation constant containing real and imaginary components represents an oscillating field with an exponentially decaying amplitude. The modal propagation constant β must be complex to satisfy the boundary conditions of a waveguide with absorbing media. The modal loss can be obtained directly from the imaginary component of β. In cases where extension of the analysis to, or computation of the boundary conditions in, the complex domain is difficult the absorption loss of the mode may be estimated by integrating over the total field in the region of the absorbing analyte [2,3].

Three distinct waveguide structures are modelled in the following sections. The first structure analysed is a multilayer planar or slab waveguide. This is the simplest of waveguides to model because it is bounded in one direction only. The model used here is based on the work of Walpita [4,5]. Walpita introduces a simple 2x2 transfer matrix method for numerically calculating the propagation constant of bound modes [4]. This is a simpler treatment of the 4x4 transfer matrix method used by Smith [6] and Vassel [7]. The 4x4 matrix allows for coupling between TE and TM polarization states which is ignored in the 2x2 matrix method. The 2x2 matrix method was devised originally by R. C. Jones [8] in 1941 for optically isotropic layers such as are analysed in this thesis. Walpita [5] expands the 2x2 matrix technique to evaluate the approximate values of the

propagation constants for weakly guiding optical fibres using a method similar to that used by Marcatili [9] to model rectangular waveguides. In this thesis, Walpita's method is applied to D-shaped and tapered fibre structures. A comparison is made between this approximation method and rigorous solutions for these structures available in literature.

Rigorous solutions to the problem of finitely clad single mode optical fibre are employed to estimate the 'cutoff diameter' of a tapered fibre that no longer supports the HE_{11} (or LP_{01}) mode by calculating the local modes of the structure as it narrows. The rigorous models are more complicated than the planar waveguide model because they solve for Maxwell's equations in the polar coordinates of the cylindrical optical fibre geometry. Two models are used to derive the local modes of tapered fibre. The first model is based on the finitely clad fibre model of Kuhn [10] using the characteristic equation published by Unger [11] in 1980. The second model uses the weakly guiding approximation as applied to doubly clad single-mode fibre by Monerie [12] in 1982. The rigorous model by Kuhn is used as a reference point to demonstrate the accuracy of the weakly guiding approximation in the case of an external medium whose refractive index is well removed from the core and cladding indices. The cutoff diameter predicts the minimum degree of tapering required to produce a tapered evanescent wave sensor where the guiding interface is now the cladding / analyte boundary. The sensitivity of the taper is then calculated by ignoring the core and reducing the Kuhn - Unger theory to a waveguide where the guided region refractive index is the untapered fibre cladding index. At all stages in the applications of these models the planar waveguide approximations are directly compared to the rigorous solutions.

The properties of polished fibre sensors are estimated using a rigorous analysis of weakly guiding D-shaped fibre originated by Vassalo [13] in 1986 and more recently generalised by Love *et al.* [14] and Marcuse *et al.* [15] in 1991. This model is used to calculate the local modes of a straight fibre where the distance from the core / cladding interface to external medium is varying. The results of this analysis are then compared to that of the extended planar waveguide model.

The models mentioned above and detailed below are used exclusively in predicting the sensitivity of single-mode fibres. The sensitivity of highly multimoded fibres is quite accurately predicted by the geometrical model of fibre ATR sensitivity in chapter 2 section 2.5. Sensitivity for highly multimoded fibres is predicted assuming a continuous uniform modal distribution over the range of allowed propagation angles dictated by the launch conditions. Sensitivity per angle is calculated as described in chapter 2.

3.2 Planar waveguide model.

The solution to the planar waveguide model is obtained by using Maxwell's equations to give the general form for a plane wave and then solving for a plane wave confined to the structure shown in figure 3.2. This is achieved by applying the continuity conditions for the tangential electric or magnetic field components at the waveguide layer boundaries. The waveguide is assumed to be made of layers of homogenous, linear, isotropic and non-magnetic media. The relative permittivity for each layer can be represented by a scalar ε_j. The integer subscript j denotes the layer number. The magnetic permeability for all layers has the free space value μ_o.

Maxwell's equations may be written for such media as

$$\nabla x E = -\mu_o \frac{\partial H}{\partial t} \qquad 3.1$$

$$\nabla x H = \varepsilon \frac{\partial E}{\partial t} + \sigma E \qquad 3.2$$

$$\nabla . D = \rho; \quad (D = \varepsilon E) \qquad 3.3$$

$$\nabla . H = 0 \quad (B = \mu_o H) \qquad 3.4$$

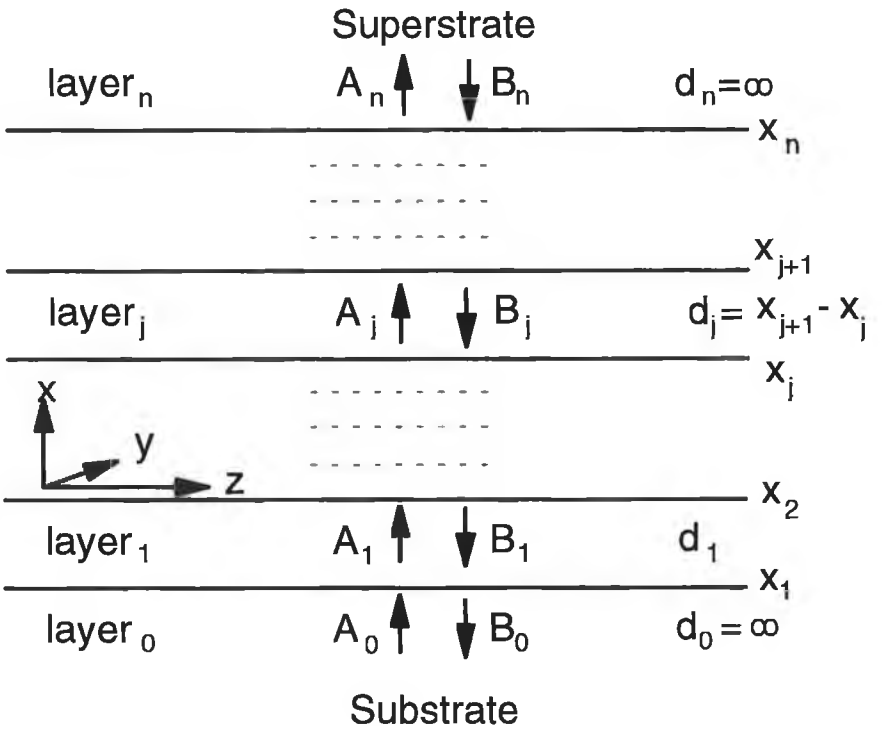

figure 3.2 n+1 layered planar waveguide structure. Layers 0 and n are the substrate and superstrate respectively and have infinite width

where $\rho = 0$ in the absence of free charges. Taking the curl of equation 3.1 and using the identity $\nabla x(\nabla x) = \nabla(\nabla .) - \nabla^2$, gives

$$\nabla(\nabla.E) - \nabla^2 = -\mu_o \varepsilon \frac{\partial^2 E}{\partial t^2} + \sigma \frac{\partial E}{\partial t} \qquad 3.5$$

Assuming a time dependence $e^{i\omega t}$, where ω is the angular frequency, and using $\nabla.E = 0$ gives

$$\nabla^2 E = -(\omega^2 \mu_o \varepsilon + i\omega\sigma)E \qquad 3.6$$

The explicit loss component ($i\omega\sigma$) may be dropped and replaced by using complex representation of the permittivity ε. The wave propagates along the waveguide axis,

denoted by the Cartesian coordinate z, with a propagation constant β. The general solution for a guided wave travelling in the positive z direction is given by

$$E = E_{(x,y)} \quad e^{\iota(\omega t + \beta z)} \qquad 3.7$$

For consistency the cartesian coordinate z is used in all models as the direction of propagation of guided waves.

Planar waveguides support two distinct types of guided mode; transverse electric (TE) and transverse magnetic (TM). The modes are distinguished by the orientation of the electric field vector with respect to the dielectric boundary. The TE and TM mode electric field vectors are perpendicular to each other. The electric field of a TE mode is parallel to and consequently continuous across the dielectric interface while the electric field of the TM mode has a component perpendicular to the interface. The analysis below is for TE modes using the continuity of the E field. TM modes may be analysed in an identical fashion by considering the continuity of the magnetic field across the dielectric interfaces. To obtain solutions for the planar waveguide structure the continuity of the first derivative of the field is also used.

Because the E field for TE waves is polarised in the y direction there is no field in the x direction i.e. $E_x = 0$. Because the waveguide is infinite in extent and uniform in the y direction, the field is uniform in the y direction, i.e. $dE/dy = 0$. The general solution for the wave equation reduces to

$$E = E_y \, e^{i(\omega t + \beta z)} \qquad 3.8$$

where E_y is a function of x only. Equation 3.6 then becomes

$$\frac{\partial^2 E_y}{\partial x^2} - (\beta^2 + \mu_o \varepsilon \omega^2) E_y = 0 \qquad 3.9$$

Solving for E_y gives

$$E_y(x) = e^{\pm i(\beta^2 - \mu_o \varepsilon \omega^2)^{1/2} x}$$

$$= e^{\pm i\left(\beta^2 - k_o^2 n^2\right)^{1/2} x} \qquad 3.10$$

where k_o is the free space wavenumber and n the refractive index of the medium. The complete solution of E_y is

$$E_y = e^{\pm i\left(\beta^2 - k_o^2 n^2\right)^{1/2} x} \quad e^{i(\omega t - \beta z)} \qquad 3.11$$

The derivative of the field (dE/dx) is continuous across the dielectric interface and is given by

$$\frac{\partial E_y}{\partial x} = \pm p x e^{\pm px} \quad e^{i(\omega t - \beta z)}; \quad \text{where } p = \left(\beta^2 - k_o^2 n^2\right)^{1/2}. \qquad 3.12$$

To distinguish between the layers in a multilayer planar wavguide a layer subscript j is used. For example, layer dependent constants, such as refactive index, are labelled n_j. The layers are numbered from the substrate (layer 0) to the superstrate (layer n). The continuity conditions for E_y and dE_y/dx can be used to relate the fields in adjacent layers of the waveguide. The field evolution within each layer is described by equations 3.11 and 3.12. The time and z dependence in these equations may be ignored as they are not functions of x (layer independent). Field amplitude coefficients A_j and B_j are used to represent counter-propagating waves in each layer j. The field amplitude coefficients are used to normalise the field amplitude at $x=x_j$. The field for each layer j is written as a function of $x-x_j$. For each layer j, E_y and dE_y/dx are written as follows:

$$E_{yj} = A_j e^{-p_j\left(x-x_j\right)} + B_j e^{p_j\left(x-x_j\right)} \qquad 3.13$$

$$\frac{\partial E_{yj}}{\partial x} = -p_j A_j e^{-p_j\left(x-x_j\right)} + p_j B_j e^{p_j\left(x-x_j\right)} \qquad 3.14$$

The counterpropagating fields are required to set up a standing wave pattern and can be considered as reflections off alternate boundaries. Writing in matrix form yields

$$\begin{pmatrix} E_{yj} \\ E'_{yj} \end{pmatrix} = \begin{pmatrix} e^{-p_j\left(x-x_j\right)} & e^{p_j\left(x-x_j\right)} \\ -p_j e^{-p_j\left(x-x_j\right)} & p_j e^{p_j\left(x-x_j\right)} \end{pmatrix} \begin{pmatrix} A_j \\ B_j \end{pmatrix} \qquad 3.15$$

Using the continuity conditions for E_y and E'_y (shorthand for dE_y/dx) at the boundary $x = x_{j+1}$ gives a relationship between the factors A and B for layer j and j+1. In equation 3.15 the value $x-x_j$ becomes d_j for the coefficients A_j and B_j and it is 0 for the coefficients A_{j+1} and B_{j+1}. d_j is the thickness of the layer j defined as $x_{j+1} - x_j$. The continuity conditions become

$$\begin{pmatrix} 1 & 1 \\ -p_{j+1} & p_{j+1} \end{pmatrix} \begin{pmatrix} A_{j+1} \\ B_{j+1} \end{pmatrix} = \begin{pmatrix} e^{-p_j d_j} & e^{p_j d_j} \\ -p_j e^{-p_j d_j} & p_j e^{p_j d_j} \end{pmatrix} \begin{pmatrix} A_j \\ B_j \end{pmatrix} \qquad 3.16$$

Using the continuity condition repeatedly a 2x2 matrix may be generated to relate the layer coefficients in the substrate (A_0,B_0) to the corresponding superstrate coefficients (A_n,B_n). This 2x2 matrix is called the waveguide transfer matrix and is used to obtain solutions for the allowed modes of the waveguide. Solutions are obtained by applying the condition for a guided wave ie. the fields are evanescent in the substrate and superstrate. To satisfy this condition, the coefficients B_n and A_0 must be 0. If these coefficients are non zero then the fields in the substrate and superstrate increase exponentially with distance from the waveguide. If the fields increase with distance from the waveguide they will become infinite at $\pm\infty$ which violates the condition for any real field distribution. Therefore

$$\begin{pmatrix} A_n \\ 0 \end{pmatrix} = \begin{pmatrix} t_{11} & t_{12} \\ t_{21} & t_{22} \end{pmatrix} \begin{pmatrix} 0 \\ B_o \end{pmatrix} \qquad 3.17$$

where t_{nm} are the components of the waveguide transfer matrix T. To satisfy equation 3.17 the transfer matrix element t_{22} must be 0. t_{22} is a function of β only and it is possible to compute allowed guided mode solutions for a waveguide of an arbitrary number of layers n+1 by computing the transfer matrix T and looking for solutions of the form $t_{22}(\beta) = 0$.

The 2x2 matrix method may be extended to estimate the propagation constant of any optical waveguide of arbitrary cross section. The basis for this technique was first demonstrated for rectangular waveguides by Marcatili [9]. To estimate the properties of rectangular waveguides, the field matching conditions in the shaded regions of figure 3.3 may be ignored as the field in these regions is only a small portion of the total field. The modes are hybrid but approximate the TE and TM modes of a planar waveguide. To solve the system two separate planar guides are analysed. First the propagation constant and effective index for the planar guide consisting of 3 layers of refractive indices n_4, n_1 and n_5 are found. The effective index (n_{eff}) computed for this planar waveguide (using the 2x2 matrix method) replaces the index n1 for the second planar guide consisting of the layers of refractive index n_3, n_{eff} and n_2. The result of the second calculation, taking care to use the same field orientation, generates the approximate propagation constant of the rectangular guide. This method is detailed in texts on integrated optics by Tamir [16] and Lee [17].

To obtain the propagation constant for an arbitrary 2-D waveguide, for example an optical fibre, it is possible to model it as a number of thin rectangular guides as shown in figure

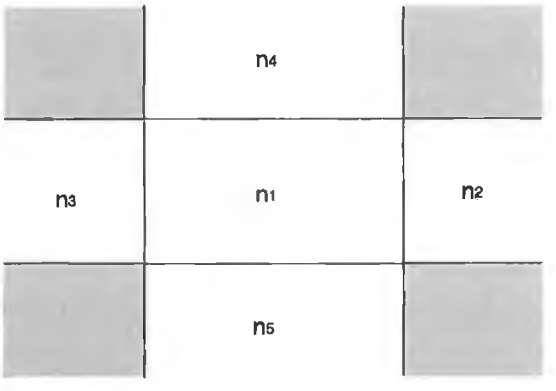

figure 3.3 Waveguide segmented using Marcatili's method for analysing rectangular waveguides described in the text.

3.4. For each rectangular section an effective index is computed. The propagation characteristics for the waveguide are then computed by solving for the multilayer waveguide with refractive indices equal to the calculated effective indices of the planar waveguide sections.

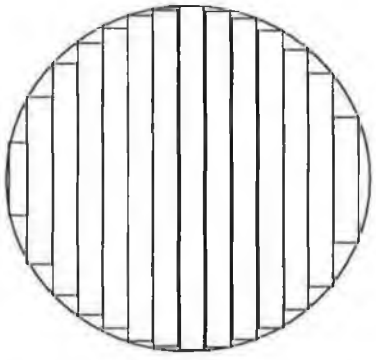

figure 3.4 infinitely clad optical fibre subdivided into rectangular waveguide segments for analysis

Formulation of the software to perform the required calculations is given in Appendix A. As previously mentioned the evanescent absorption of a mode may be calculated using the complex refractive index representation of a lossy dielectric. In this case the matrix elements including t_{22} are complex. Solutions must be found for both the real and imaginary parts of t_{22} for a bound guided wave. To obtain such a solution the modal propagation constant β must also be complex. The imaginary part of β represents power lost by the guided mode to the lossy material by absorption.

3.3 Finitely-clad optical fibre model.

3.3.1 Introduction.

As explained in the introduction to this chapter, the finitely clad model is used to predict the 'cutoff' condition for the HE_{11} (and in the weakly guiding case, the LP_{01}) mode. This information is then used to predict the degree of tapering required to produce a tapered evanescent wave sensor. The models are also used for comparison with the normal and generalised planar waveguide analysis for such predictions.

3.3.2 Rigorous finitely-clad fibre theory.

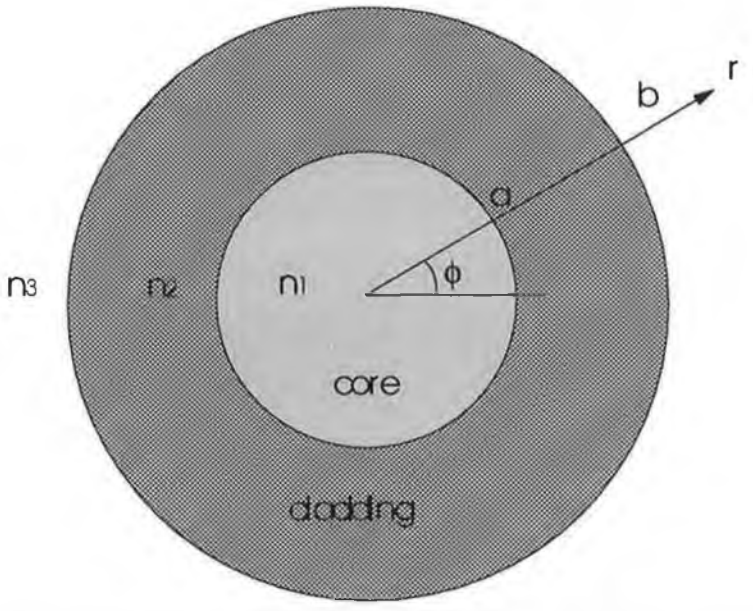

figure 3.5 cross section of a finitely clad optical fibre showing the transverse geometry

Solutions for the guided modes of an optical fibre require Maxwell's equations to be solved for a cylindrical geometry. The symmetry of the optical fibre shown in figure 3.5 is best described using the cylindrical polar coordinate system r,ϕ,z. r and ϕ are shown in figure 3.5 and z is the cartesian coordinate which coincides with the waveguide axis which is perpendicular to the plane of the page. As in section 3.2, the waveguide is assumed to be made from homogenous, linear, isotropic and non-magnetic media. Maxwell's equations reduce to the simple form of equation 3.6, the general wave equation, for Cartesian coordinates only. The operator ∇^2 for the cylindrical components of the transverse fields is

$$\nabla_t^2 = \frac{\partial^2}{\partial r^2} + \frac{1}{r}\frac{\partial}{\partial r} + \frac{1}{r^2}\frac{\partial^2}{\partial \phi^2} + \frac{\partial^2}{\partial z^2} \qquad 3.18$$

where the wave equation as a function of E_z is given by

$$\nabla^2 E_z + \mu_o \varepsilon \omega^2 E_z = 0 \qquad 3.19$$

It is simpler to solve for the cartesian field components E_z and H_z and use these to generate the remaining fields $E_{r,\phi}$ and $H_{r,\phi}$. The time and z dependence for a fibre mode are the same as are used for the planar waveguide model in equation 3.7. E_z can be written as $E(r,\phi)\ e^{(\omega t \pm \beta z)}$. The magnetic field H_z is an identical function of z and t. Assuming that E_z is a separable function of r,ϕ and z it becomes

$$E_z = \psi_{(r)}\Phi_{(\phi)}e^{\iota(\omega t \pm \beta z)} \qquad 3.20$$

The solution for $\Phi_{(\phi)}$ takes the form

$$\Phi_{(\phi)} = A\cos(m\phi) + B\sin(m\phi) \qquad 3.21$$

where m is an integer to satisfy the recurrence relation $\Phi_{(\phi)} = \Phi_{(\phi+2\pi)}$. Using equations 3.21 and 3.18, equation 3.19 becomes

$$\left(r^2\frac{\partial^2}{\partial r^2} + r\frac{\partial}{\partial r}\right)E_z + \left(\left(k_0^2 n^2 - \beta^2\right)r^2 - m^2\right)E_z = 0 \qquad 3.22$$

The equation is now in the form of Bessels differential equation and solutions for $\psi_{(r)}$ are Bessel functions of integer order m. The factor $(k^2n^2 - \beta^2)^{1/2}$ is the radial component of the propagation vector β. The Bessel function solutions for the radial field $\psi_{(r)}$ is

$$\Psi_{(r)} = AJ_m\left(\frac{ur}{a}\right) \qquad r < a \qquad 3.23$$

$$\Psi_{(r)} = CI_m\left(\frac{wr}{a}\right) + DK_m\left(\frac{wr}{a}\right) \qquad r > a \qquad 3.24$$

$$\Psi_{(r)} = FK_m\left(\frac{qr}{a}\right) \qquad r > b \qquad 3.25$$

where J is a Bessel function of the first kind and I and K are mofified Bessel functions of the first and second kind, respectively.

$$u = a\left(k^2 n_1^2 - \beta^2\right)^{1/2}, \quad w = a\left(\beta^2 - k^2 n_2^2\right)^{1/2}, \quad q = a\left(\beta^2 - k^2 n_3^2\right)^{1/2} \qquad 3.26$$

Therefore for a guided or bound mode in a fibre $k_o^2 n_1^2 > \beta^2 > k_o^2 n_2^2$. The general solution for r < a does not include Y_m terms as $Y_m(r) \rightarrow \infty$ as $r \rightarrow 0$ which is physically impossible. Similarly for infinitely clad fibre, the I_m terms are omitted because $I_m(r) \rightarrow \infty$ as $r \rightarrow \infty$. In the case of a finitely clad fibre, however, the I_m terms represent reflections of the evanescent wave at the cladding boundary r = b shown in figure 3.5. Keeping only the r and ϕ dependence, the full solution for E_z and H_z in the three regions of figure 3.5 are then

$$E_z = A_e J_m\left(\frac{ur}{a}\right) e^{\pm \imath m\phi} \qquad r < a \qquad 3.27$$

$$E_z = \left[C_e I_m\left(\frac{\omega r}{a}\right) + D_e K_m\left(\frac{\omega r}{a}\right)\right] e^{\pm \imath m\phi} \qquad a < r < b \qquad 3.28$$

$$E_z = F_e K_m\left(\frac{qr}{a}\right) e^{\pm \imath m\phi} \qquad r > b \qquad 3.29$$

where the subscript *e* is used to signify the E field coefficients. Similarly a subscript *h* may be used to denote H field coefficients. The remaining field components $E_{r,\phi}$ and $H_{r,\phi}$ can be generated from E_z and H_z directly using Maxwell's equations. The unknown coefficients $A_{e,h}$ to $F_{e,h}$ may be obtained by solving for the continuity of the z and ϕ fields at the boundaries r = a and r = b. This yields 8 linear equations for the 8 coefficients $A_{e,h} \rightarrow F_{e,h}$. This may be written as an 8x8 homogenous matrix the determinant of which must be 0 for a non-trivial solution to exist. The determinant, from which the characteristic equation of the fibre is obtained, is a function of β only, all other variables being determined by the fibre parameters. This analysis is shown explicitly for the much simpler weakly guiding model in the next section.

The form of the characteristic equation, as given by Unger [11], is reproduced in Appendix B. This equation is used to predict the taper diameter at which the fundamental mode in single mode fluoride fibre is no longer guided by the fibre core.

3.3.3 Weakly guiding approximation.

The weakly guiding approximation is valid where $n_{cl} \cong n_{\infty}$ [18] and is much simpler to solve for the finitely clad structure outlined in the previous section. Solutions to the guided wave propagation constant may be obtained by solving the scalar wave equation for the finitely clad structure. This simplification is valid because the fields in the direction of propagation, E_z and H_z, which depend on the refractive index step n_{∞}-n_{cl}, are negligible. The radial dependence of the field is given as before by the Bessel function solutions in equations 3.23 to 3.25. To obtain the charateristic equation in the weakly guiding approximation, only the continuity of these transverse components at the boundaries r=a and r=b needs to be considered.

Applying the continuity conditions for ψ and ψ' gives the following equations [12]:

$$AJ_m(u) = CI_m(w) + DK_m(w) \qquad \Psi \text{ at } r = a \qquad 3.30$$

$$FK_m(qc) = CI_m(wc) + DK_m(wc) \qquad \Psi \text{ at } r = b \qquad 3.31$$

$$uJ_m(u) = vCI_m(w) + vDK_m(wc) \qquad \Psi' \text{ at } r = a \qquad 3.32$$

$$qFK_m(qc) = vCI_m(wc) + vDK_m(wc) \qquad \Psi' \text{ at } r = b \qquad 3.33$$

A 4x4 matrix may be generated from equations 3.30 to 3.33. The determinant of this matrix yields the characteristic equation for the weakly guided finitely clad fibre. Solutions for guided modes are found by setting the determinant equal to 0 and solving for β. The characteristic equation becomes:

$$Y_m \quad [-wU_m W_1 + W_2] + U_m K_m(w) I_m(wc) W_3 = 0 \qquad 3.34$$

where the following abreviations have been used:

$$Y_m = \frac{J_m(u)}{uJ'_m(u)} \quad , \quad U_m = \frac{K_m(qc)}{qK'_m(qc)} \qquad 3.35$$

and

$$W_1 = I'_m(wc)K'_m(w) + I'_m(w)K'_m(wc) \qquad 3.36$$

$$W_2 = I_m(wc)K'_m(w) - K_m(wc)I'_m(w) \qquad 3.37$$

$$W_3 = I_m(wc)K_m(w) - I_m(w)K_m(wc) \qquad 3.38$$

Using equation 3.34, the propagation constant may be plotted as a function of the degree of tapering applied to the optical fibre as shown in figure 3.7 in the next section.

3.3.4 Planar waveguide approximation

The planar waveguide and extended planar waveguide analysis are used to estimate the 'cutoff' characteristics of a taper using the structures shown in figure 3.6.

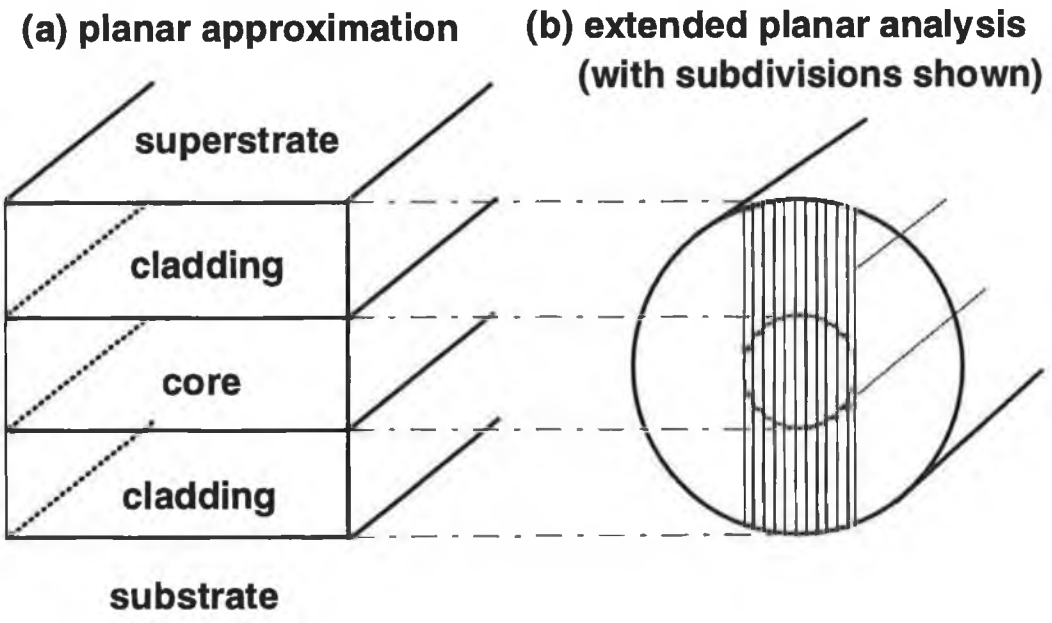

figure 3.6 simple planar waveguide approximation to finitely-clad fibre structure (a) and subdivisions used to fit finitely-clad fibre to extended planar waveguide model.

The results of a comparison of the 4 models using the parameters of the single mode fluoride fibre supplied by Le Verre Fluore (cf. Appendix C) are shown in figure 3.7. The plot shows the difference between the effective index of the local mode and the cladding index as a function of the degree of tapering that the fibre has undergone. $N_{eff} = N_{cl}$ is taken to be the cutoff point. At this value the guided wave is no longer evanescent in the cladding. The degree of tapering is represented by the taper factor defined as (Di-Dw)/Di, where Dw is the taper waist diameter and Di is the untapered fibre diameter.

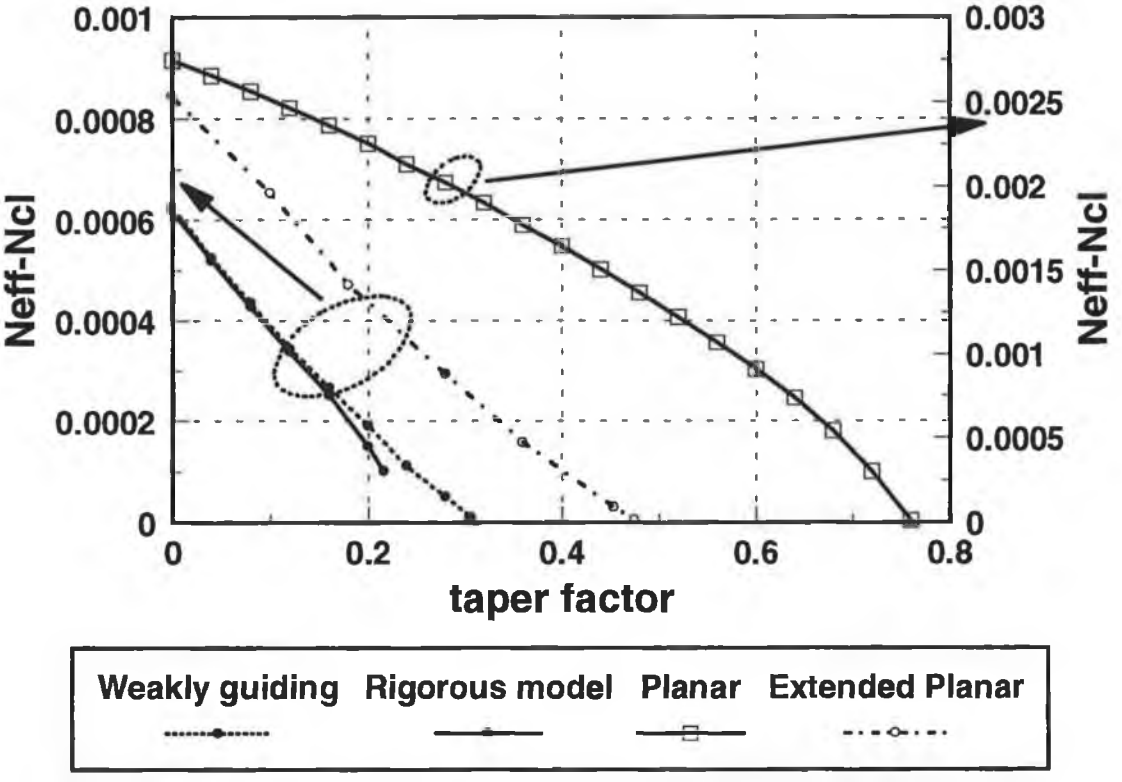

figure 3.7 comparison of fundamental mode 'cutoff' taper diameter reduction predicted by the models in section 3.3. Cutoff occurs when $N_{eff} - N_d = 0$. Planar theory prediction is on right hand axis

The rigorous finitely clad and weakly guided solutions match very closely and diverge only slightly as cutoff approaches. The HE_{11} mode is no longer guided, and therefore cutoff, before the effective index is equal to the cladding index. The predicted cutoff point for the extended planar waveguide model differs significantly from the models derived for polar coordinates. It is, however, significantly more accurate than the simple planar waveguide model which, as expected, exhibits the greatest deviation from the rigorous solution. The extended planar waveguide model represents a significant improvement on the simple planar model for the estimation of the guided mode parameters of optical fibres.

3.4 Polished fibre model

3.4.1 Introduction

A number of modal models have been examined to determine which is the most suitable for modelling the sensitivity of the asymmetric polished block structure. Vassalo [13] models the structure explicitly. In this paper, as in more recent papers by Love *et al.* [14] and Marcuse *et al.* [15], the asymmetric modal field is represented by a Fourier-Bessel series.

3.4.2 D-fibre model

The modal field of the D-shaped fibre is generated using a method similar to that used by Unger [11] and Monerie [12] when analysing finitely clad optical fibres. The field at the the cladding discontinuity is considered to be the sum of an incident and reflected evanescent field on one side and a transmitted evanescent field on the other. These fields are shown in figure 3.8. This analysis completely describes the fields in finitely clad fibres because of the symmetry of such structures. It follows from the asymmetry of D-shaped fibres that the field distribution will be asymmetric. An asymmetric field distribution can be generated by considering the field as a summation of integer order Bessel functions represented as a Fourier-Bessel series,

$$\Psi = \sum_{m=0}^{\infty} A_m J_m\left(\frac{ur}{a}\right)\cos(m\theta) \qquad r < R \qquad 3.39$$

$$\Psi = \sum_{m=0}^{\infty} \left[C_m K_m(\frac{wr}{a}) + D_m I_m(\frac{wr}{a})\right]\cos(m\theta) \qquad r > R \qquad 3.40$$

where $u^2 = ak^2(n^2_{core} - n^2_{eff})$ and $w^2 = ak^2(n^2_{neff} - n^2_{clad})$.

The amplitude coefficients are related by reflection at the cladding discontinuity at x=d and the fields in the core and cladding are connected by the continuity of Ψ and $d\Psi/dr$ at x = R.

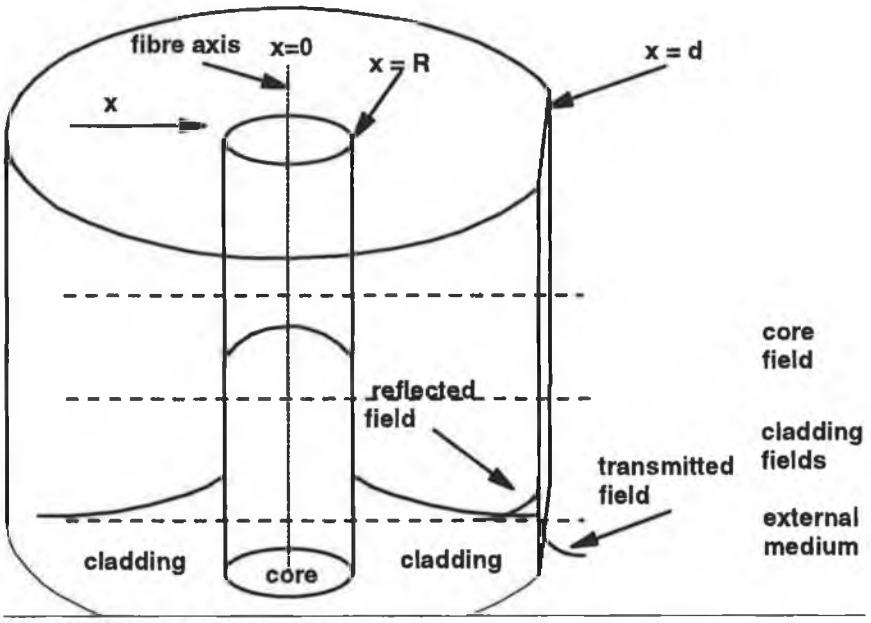

figure 3.8 D-shaped fibre structure

To solve the system for the guided wave propagation constant, the fields in the cladding and external medium about the plane x=d are rewritten using Cartesian coordinates and a plane wave expansion. It is assumed that the field is evanescent in both regions. The field in the region x > R bounded by the plane x < d is the sum of two counter-propagating evanescent plane waves. The wave with the exponentially increasing amplitude in the positive x direction is generated by reflection of the outward evanescent wave from the discontinuity at the plane x = d. The total field may be written,

$$\Psi = \int_{-\infty}^{\infty} e^{ivy}\left[S_v e^{-\sigma(x-d)} + T_v e^{\sigma(x-d)}\right]dv \qquad 3.41$$

where S_ν is the incident amplitude, T_ν the reflected amplitude and $\sigma^2 = \omega^2 + \nu^2$. $S_\nu = R_\nu T_\nu$ where R_ν is the reflection coefficient for a complex plane wave. The field in the external medium x > d is also written as a plane wave expansion about x=d

$$\Psi = \int_{-\infty}^{\infty} e^{ivy} G_\nu e^{-\tau(x-d)} dv \qquad 3.42$$

The continuity conditions at the boundary x = R relate equations 3.39 and 3.40 and the identical conditions at x = d are used to equate equations 3.41 and 3.42. The plane wave expansion in the cladding describes the field which is identical to the Fourier-Bessel series and the two sets of equations are equivalent. The plane wave expansions and the Fourier-Bessel function solutions may be related as follows,

$$\sum_{m=0}^{\infty} C_m K_m(\frac{wr}{a})\cos(m\theta) = \int_{-\infty}^{\infty} e^{ivy} S_\nu e^{-\sigma(x-d)} dv \qquad 3.43$$

$$\sum_{m=0}^{\infty} D_m I_m(\frac{wr}{a})\cos(m\theta) = \int_{-\infty}^{\infty} e^{ivy} T_\nu e^{\sigma(x-d)} dv \qquad 3.44$$

Using the analytical relationships suggested by Vassalo [19], and detailed by Marcuse [20], S_ν and D_m can be written,

$$S_\nu = \frac{e^{-\sigma d}}{2\sigma} \sum_{m=0}^{\infty} C_m \cosh(mg) \qquad \text{where } g = \cosh^{-1}(\frac{\sigma}{w}) \qquad 3.45$$

$$D_m = \frac{2}{\eta_m} \int_{-\infty}^{\infty} T_\nu e^{-\sigma d} \cosh(mg) dv \qquad \text{where } \eta_m = \begin{cases} 2 \text{ if } m = 0 \\ 1 \text{ if } m > 0 \end{cases} \qquad 3.46$$

Imposing the condition that the field and its first derivative are continuous across the core-cladding and cladding-external medium interfaces, gives for equations 3.29 and 3.30 at x = R

$$A_m J_m(u) = C_m K_m(w) + D_m I_m(w) \qquad 3.47$$

$$uA_m J'_m(u) = wC_m K'_m(w) + wD_m I'_m(w) \qquad 3.48$$

Using equations 3.33 and 3.34, A_m can be eliminated and C_m can be directly related to D_m

$$D_m = C_m \frac{uJ'_m(u)K_m(w) - wJ_m(u)K'_m(w)}{wJ_m(u)I'_m(w) - uJ'_m(u)I_m(w)} \qquad 3.49$$

Similarly at x=d, for y polarisation the E field is continuous across the boundary. Applying this continuity,

$$\int_{-\infty}^{\infty} [S_v + T_v] e^{ivy} dv = \int_{-\infty}^{\infty} G_v e^{ivy} dv \qquad 3.50$$

$$\Rightarrow S_v + T_v = G_v \qquad 3.51$$

and applying continuity of the field derivatives with respect to x.

$$\sigma[S_v - T_v] = -\tau G_v \qquad 3.52$$

Eliminating G_v gives the following relationship for S_v and T_v.

$$T_v = \frac{[\sigma - \tau]}{[\sigma + \tau]} S_v \qquad 3.53$$

This is the reflection coefficient R_v introduced earlier (for y polarisation only). Using the relationship for D_m given in equation 3.46, and substituting for T_v using $R_v S_v$ (where S_v is given by equation 3.45) gives

$$D_m = \frac{2}{\eta_m} \sum_{n=0}^{\infty} C_n \int_0^{\infty} R_v \frac{e^{-2\sigma d}}{\sigma} \cosh(mg)\cosh(ng)dv \qquad 3.54$$

Using equation 3.49, D_m may be eliminated to give

$$\frac{uJ'_m(u)K_m(w) - wJ_n(u)K'_m(w)}{wJ_m(u)I'_m(w) - uJ'_m(u)I_n(w)} C_m = \frac{1}{\eta_m} \sum_{n=0}^{\infty} C_n \int_{-\infty}^{\infty} R_v \cosh(mg)\cosh(ng) \frac{e^{-2\sigma d}}{\sigma} dv \qquad 3.55$$

Multiplying by the denominator of the left hand side and dividing by J_nK_n equation 3.55 may be rearranged to give

$$\left(\frac{uJ'_n}{J_n} - \frac{wK'_n}{K_n}\right) C_m = \left(\frac{wI'_m}{I_m} - \frac{uJ'_n}{J_n}\right) \frac{I_m}{K_m} \text{rhs}(3.55). \qquad 3.56$$

Equation 3.56 may be expressed in matrix form as AC = QC where A and C are infinite column vectors and Q is an infinite square matrix. This may be rewritten (Q-A)C = 0 where the determinant of the matrix Q-A is the characteristic equation of the D-fibre. To make the solution manageable, the system is truncated to order M and the integral is changed to be over g. The characteristic equation then becomes

$$\sum_{m=0}^{M-1} \left[\left(\frac{wK'_m}{K_m} - \frac{uJ'_m}{J_m}\right) C_m + \left(\frac{wI'_m}{I_m} - \frac{uJ'_m}{J_m}\right) \times \frac{I_m}{K_m \eta_m} \sum_{n=0}^{M-1} P_{mn} C_n \right] = 0 \qquad 3.57$$

with

$$P_{mn} = 2 \int_0^{\infty} R_v \cosh(mg)\cosh(ng) e^{-2\sigma d} dg \qquad 3.58$$

where equation 3.57 and 3.58 are Vassalo's equations 7 and 8 from [13] with $\sigma = \omega \cosh(g)$. The order M for the matrix determines the accuracy of the numerical calculations and also the time required to reach a solution. Vassalo states that taking M = 3 is sufficient to obtain a good evaluation of the propagation constant β. Values of 3 and 4 for M were used in numerical calculations of the D-fibre propagation constant in this thesis. Higher orders of M quickly lead to much longer calculation times without a corresponding increase in the accuracy of β.

3.4.3 Planar waveguide approximation

The planar waveguide and extended planar waveguide analysis are used to estimate the effect of the proximity of the plane on the D-fibre propagation constant and also on the penetration of the evanescent field into the external half space defined by the polished plane. The field distributions and propagation characteristics are compared to those predicted by Vassalo's rigorous theory. The structures used for the planar and extended planar D-fibre approximations are shown in figure 3.9 below.

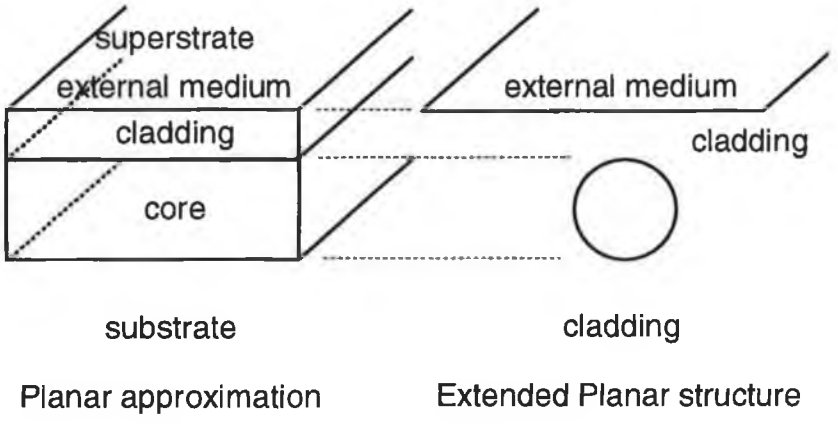

figure 3.9 Planar and extended planar waveguide structures used to model D-shaped fibre

The results of a comparison of the 3 models using the parameters of the single mode fluoride fibre supplied by Le Verre Fluore are shown in figure 3.10. The plot shows the

difference between the effective index of the D-fibre mode and the cladding index as a function of the distance of the half-space from the core-cladding boundary. The effective index is plotted for an external medium of refractive index 1.38 corresponding to an IPA analyte. The predicted effective index is also plotted using Vassalo's model for an external index of 1 corresponding a gas. From the data generated using Vassalo's model it is apparent that the modal field in D-shaped fibre can be so distorted by the half space that the core-cladding structure no longer guides. The guided mode propagation constant values calculated using Vassalo's model may be validated by calculating the propagation constant using the weakly guiding model in the absence of any perturbation. The value of the effective index for the fibre studied is 1.49062, calculated using the weakly guiding approximation. The propagation constant calculated using the rigorous model approaches this value as $d \rightarrow \infty$ as shown in figure 3.11. In figure 3.12 the other limit of interest, N_{ext} -> N_{cl}, is tested for convergence to the weakly guiding result. The extended planar waveguide model is a reasonable approximation.

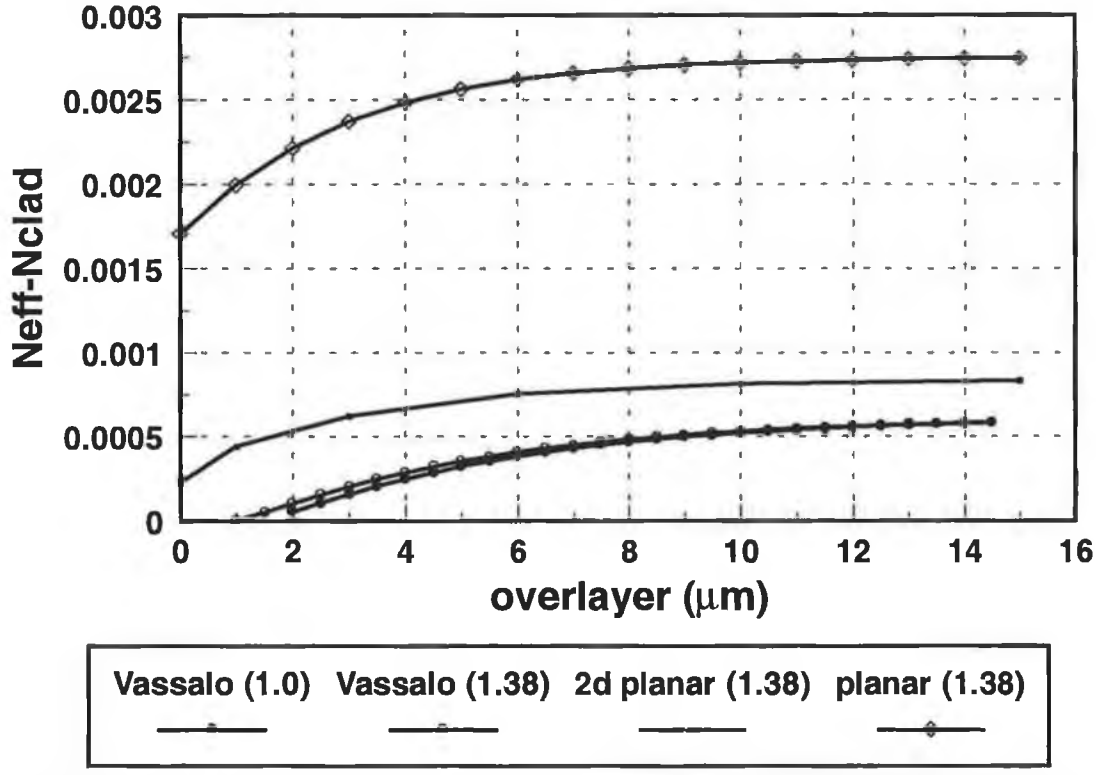

figure 3.10 Graph of Neff-Ncl for various overlayer thicknesses using the planar, extended planar and Vassalo's models.

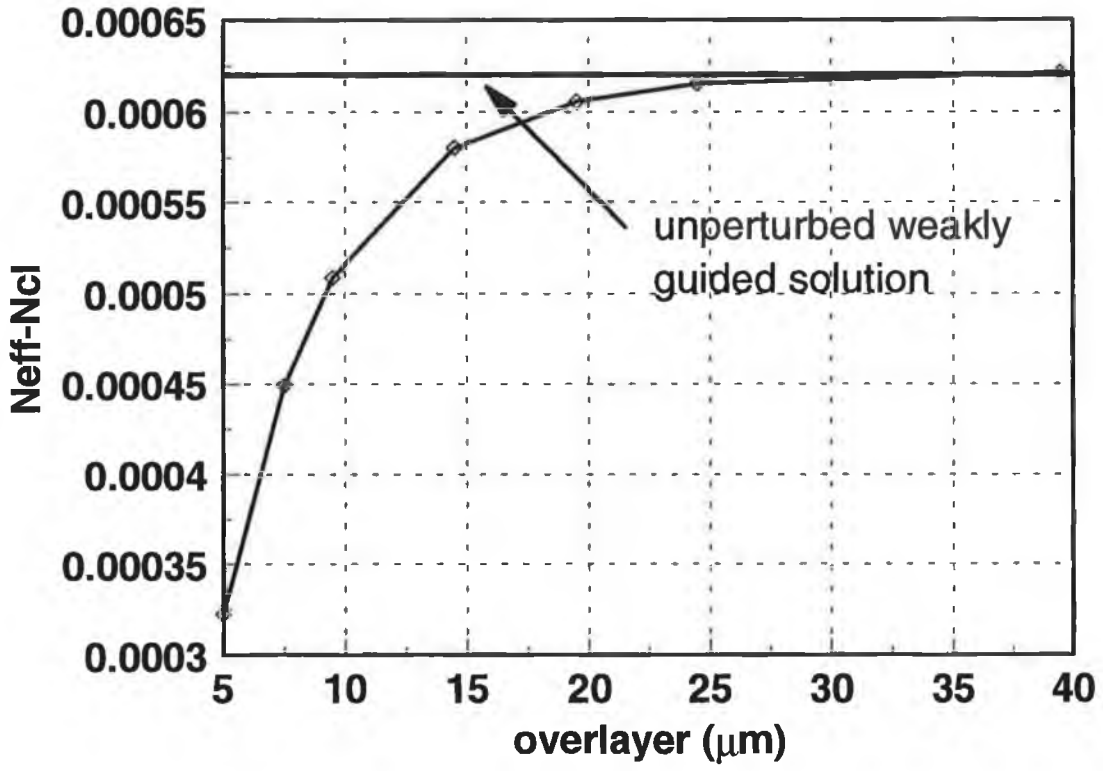

figure 3.11 graph showing convergence of Vassalo model to unperturbed weakly guided fibre effective index as d increases for a fixed Next

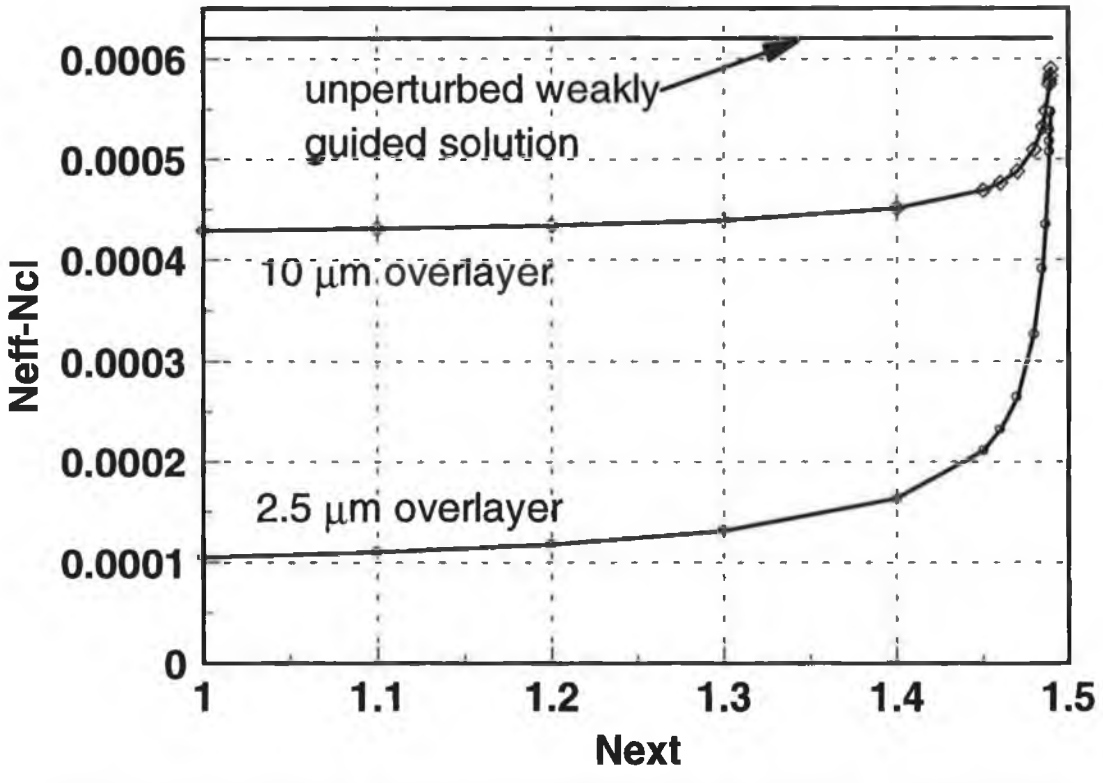

figure 3.12 graph showing convergence of Vassalo model to unperturbed weakly guided fibre effective index as Next approaches Nclad for 2 different overlayer thicknesses

The parameters used to generate the data for figures 3.11 and 3.12 were as follows:

n_{core}	= 1.495
$n_{cladding}$	= 1.49
R (core radius)	= 5.5μm
d (overlayer distance)	= variable
λ (wavelength)	= 3.4μm[2]
M (order of calc)	= 3
$n_{external}$	= 1.00 (gas) / 1.38 (IPA) / variable in figure 3.12.

These parameters are for Le Verre Fluore monomode fluoride fibre. The information used to obtain the parameters below is given in Appendix C.

3.5 Loss calculations

In section 3.2 it was stated that the complex representation of the refractive index of an arbitrary layer in a waveguide may be used to calculate the loss in a mode. This technique, while accurate, requires considerable calculation for the more complex analysis discussed in sections 3.3 and 3.4 as solutions must be found in the complex domain. In many cases it is simpler to calculate the exact modes of the equivalent lossless waveguide and then apply perturbation theory to calculate the losses due to an absorbing layer. From perturbation theory, it can be shown that absorption loss of a mode is proportional to the product of the absorption coefficient of the absorbing layer and the fraction of the total power within that layer as calculated for the lossless waveguide [18]. Therefore, if the ratio of power in the analyte to the total guided power is r and the absorption coefficient is α then the modal absorption coefficient is rα. Beer's law for the mode may be written as

$$I = I_o e^{-r\alpha cL} \qquad 3.59$$

[2] A number of the calculations used 3.392μm which is the wavelength of the HeNe laser used for the experimental work.

where L is the interaction length (or path length) of the absorbing region. The value of r is very important for evanescent wave sensing because it determines the sensitivity of the mode to external absorbing media. It must be noted, however, that equation 3.59 is applicable only when $n_i << n_r$. For flammable gases this is normally true with ratios of n_r to n_i of greater than 1000:1.

3.6 Conclusion

In this chapter models have been presented that may be applied to all of the monomode optical fibre structures studied in the course of this investigation. The extended planar waveguide model has been used to approximate tapered and D-shaped fibre structures to good accuracy. This demonstrates the flexibility of the extended planar waveguide model and indicates that it may be used as a reasonable approximation where rigorous theories for arbitrary structures have not been developed. The software used to generate the graphs above is described in Appendix A. In chapter 6 the predicted evanescent wave sensitivity of the models will be compared to experimental data. Modifications to the theory will be introduced in the text where appropriate.

1. Snyder A.W., and Love J.D.: '**Optical Waveguide Theory**', Chapman and Hall 1991, Chapter 10

2. Harrick N.J.: '**Internal Reflection spectroscopy: Review and supplement**', 1985 Harrick Scientific Corporation, pp 50-54.

3. Ruddy V.: '**An effective attenuation coefficient for evanescent wave spectroscopy using multimode fiber**', Fiber and integrated optics , 1990, Vol. 9, pp. 142-150

4. Walpita L.M.: '**Solutions for planar optical waveguide equations by selecting zero elements in a characteristic matrix**', Journal Optical Society of America A 1985 , Vol. 2, No. 4, pp. 595-602

5. Walpita L.M.: '**Calculation of the approximate propagation characteristics for any given two-dimensional optical waveguide**', Electronics Letters, 1985, Vol. 21, No.23, pp. 1074-1076.

6. Smith D.O.: '**Magneto-optical scattering from multi-layer magnetic and dielectric films**', Optica Acta, 1965, Vol. 12, pp. 13-45

7. Vassel M.O.: '**Structure of optical guided modes in planar multilayers of optically anisotropic materials**', Journal Optical Society of America 1974, Vol. 64, No. 2, pp. 166-173

8. Jones R.C.: '', Journal Optical Society of America, 1941, Vol. 31, p. 488

9. Marcatali E. A.J.: '**Dielectric rectangular waveguide and directional coupler for integrated optics**', Bell Systems Technical Journal, 1979, Vol. 48, pp. 2071-2102

10. Kuhn M. H..: '**The influence of the refractive index step due to the finite cladding of homogenous fibres on the hybrid properties of modes**', Archiv Elektron & Ubertragunstech, 1974, Vol. 28, No. 10, pp. 393-401

11. Unger H.G.: '**Planar optical waveguides and fibres**', Oxford University Press 1980, pp. 290-317.

12. Monerie M.: '**Propagation in doubly clad single-mode fibres**', IEEE Trans Microwave Theory & Techniques, 1982, Vol. MTT-30 No. 4, pp. 381-388

13. Vassalo C.: '**Rigorous theory for modes of optical fibres with cladding limited by a plane**', Electronics Letters, 1986, Vol. 22, No. 18, pp. 944-5

14. Love J.D., Ladouceur F., Marcuse D.: '**Vector modes of D-shaped fibres**', Proceedings 16th Austrailian Conference on Optical Fibre Technology (ACOFT-16), 1991, pp. 270-3

15. Marcuse D., Ladouceur F. and Love J.D.: '**Vector modes of D-shaped fibres**', IEE Proceedings-J, Vol. 139, No. 2, 1992, pp. 117-126

16. Tamir T.: '**Guided-Wave Optoelectronics** (Springer Series in electronics and photonics 26)', 2nd ed. Springer Verlag, 1990.

17. Lee D.L.: '**Electromagnetic principles of integrated optics**', Wiley, 1986.

18. Snyder A.W., and Love J.D.: '**Optical Waveguide Theory**', Chapman and Hall 1991

19. Reference 13, Equations 4 and 5

20. reference 18, Appendix section 11.2.1, Equations 33(a) to 39(c)

21. reference 17, Chapter 18.

Chapter 4 Fibre Sensor Fabrication

4.1 Introduction

The fabrication of fibre sensor devices forms an important section of the work undertaken for this thesis. The aim of this investigation into fabrication techniques is to develop methods for efficient access to the evanescent field in zirconium optical fibre. These methods could then be used to produce a range of sensor types for evaluation purposes. Factors which would determine the practical viability of a given method include, ease and cost of fabrication, and stability of sensor structure. These sensors should be capable of detecting concentrations of flammable gases, in air, well below the relevant gas lower explosion limit (LEL). None of the devices studied is currently available as part of an 'off the shelf' sensor. The sensor preparation methods to be discussed in this chapter are fibre polishing and tapering. Each of these processes was performed using all glass fluoride fibres. Polishing comes under the heading of cladding removal processes as outlined in chapter 2 section 2.4.1. Tapering is a waveguide modification process as defined in chapter 2 section 2.4.2. Polishing and tapering techniques have been reported extensively in literature as fabrication methods for silica fibre devices [1,2]. The techniques reported in this thesis are similar, in principal, to those used with silica fibre but differ substantially in detail from silica fibre techniques because of the physical parameters of zirconium fluoride optical fibre. An exception to the requirement for fibre preparation prior to sensing was Teflon clad multimode fluoride fibre [3] which was used as supplied and is therefore not discussed in this chapter.

4.2 Polishing

4.2.1 Polishing method

A Logitech PM2A polisher was used to fabricate monomode optical fibre semi-coupler blocks for evanescent wave sensing using a lapping and polishing process. This method is a well known one which has been used to fabricate fibre couplers and other devices and is currently used to fabricate tuneable fibre couplers from silica optical fibre [4,5,6]. Polished fibre couplers suffer from temperature instability and have been replaced by tapered couplers in fixed coupling ratio applications. Tapered sensors are discussed later in this chapter. When fabricating semi-couplers the optical fibre should be mounted in a

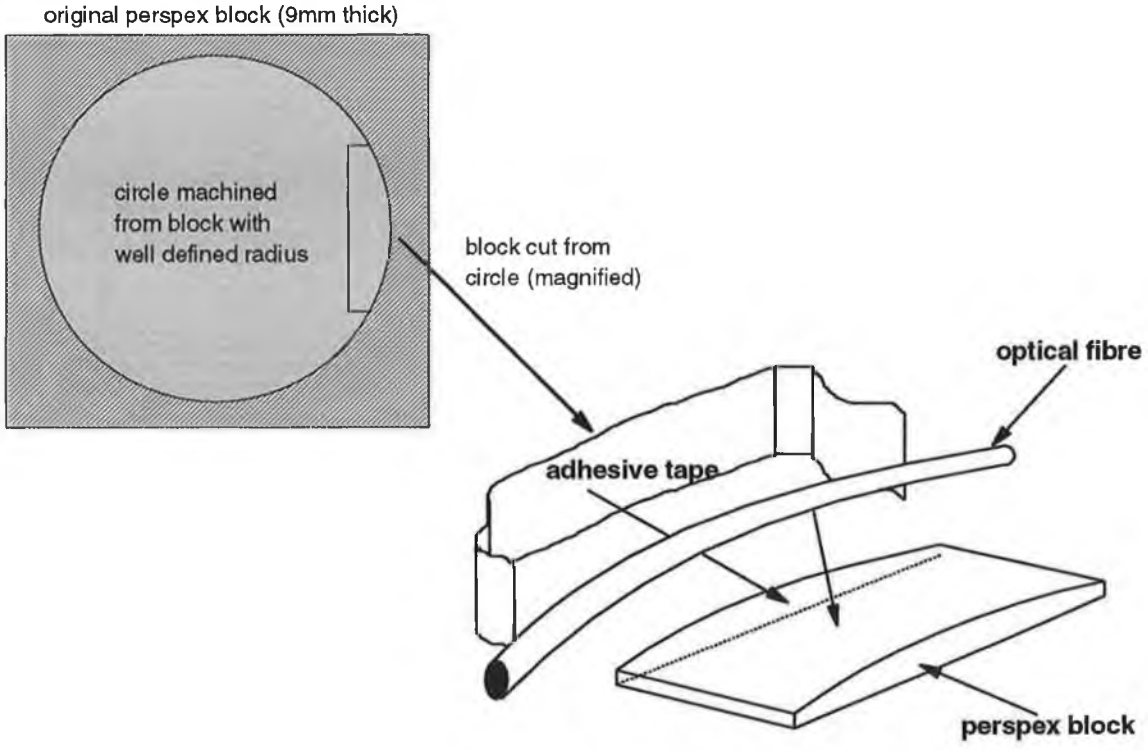

figure 4.1 fabrication of perspex block for polishing and optical fibre fixing method in preparation for half coupler polishing

stable substrate, with polishing properties similar to those of the fibre, to minimise stresses which may cause fracture of the polished fibre. In the case of silica fibre the fibre is first stripped of its protective coating and placed in a curved groove cut in a silica glass block. The groove, slightly larger than the fibre cladding diameter, is cut in the block using a diamond saw with a predetermined radius of curvature. The fibre is fixed

in place with a UV cured epoxy. The silica block provides an ideal substrate for the fibre as it is made from the same material. This method is not directly applicable to fluoride fibre because fluoride fibre is extremely brittle. To remove the protective coating from fluoride fibre is a delicate process. Initial attempts to duplicate the method used for silica fibres resulted in many fluoride fibres being damaged.

Consequently, a new method was developed for mounting fluoride fibre for polishing. The method was successful in eliminating the occurrence of fractures in the polished region. The fluoride fibre polishing technique uses perspex blocks with one face machined to a specified radius of curvature. The blocks are cut from a disc of perspex (figure 4.1) which was machined using a milling machine equipped with a specially designed fly cutter. The fibre is fixed in position using an epoxy resin which polishes at a similar rate to the fibre. The sensor preparation method illustrated in figure 4.1 is as follows:-

1. Adhesive tape is fixed to the outside of the perspex block to provide a mould for the epoxy resin.
2. The optical fibre is passed through two small holes punched in the adhesive tape and the holes are sealed with a small amount of glue. The ends of the fibre are taped to the setting block to ensure that the fibre follows the blocks radius of curvature.
3. Epoxy resin is poured into the mould and allowed to set.
4. When the epoxy has set, the tape is removed and the block is set into the polishing jig using denture fixing wax.

The epoxy resin (Epofix by Streurs, USA) setting process can take from 18 to 24 hours depending on the precise ratio of resin to hardener used (the recommended ratio is 15 to 2). Care must be taken at this stage to ensure that the fibre is secure so that it can not move during the setting process. As the time taken to polish the fibre depends on the thickness of the epoxy layer it is helpful to keep this layer as thin as possible. Reducing the epoxy layer thickness, however, increased the failure rate of the polished blocks dramatically. The increased failure rate was due to bubbles trapped under the surface of the epoxy. The bubbles rise to the top but do not break through the surface because of the high viscosity of the liquid. This is only a problem if the air bubbles are in the same

horizontal plane as the fibre because it is possible that the fibre is not completely encased in epoxy. The epoxy must therefore be deep enough to allow all the bubbles to rise out of the plane of the fibre. This increases the total polishing time but improves the quality of the mould and reduces the failure rate.

A significant problem associated with polishing is the determination of the proximity of the fibre to the polished surface. A lot of time and repetitive measurement was saved by employing a visual method to estimate the remaining epoxy layer. This was made possible by increasing the contrast between the epoxy and the perspex block. To improve the contrast a red dye is mixed with the epoxy before the hardener is added. The dye is mixed in powder form because even small quantities of dye dissolved in other liquids reduced the hardness and increased the setting time of the epoxy. The dye increased visual contrast between the epoxy and the fibre this made it easier to identify the optical fibre cladding ellipse for polish depth measurements as explained below.

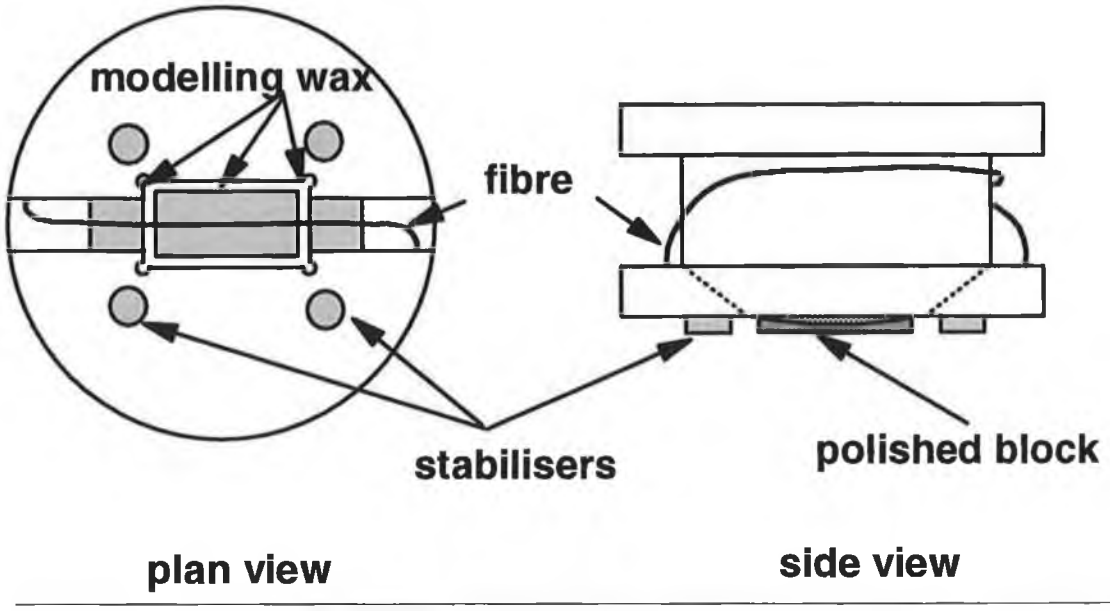

figure 4.2 jig for optical fibre half block (or semi-coupler) polishing as described in figure 4.1

When the epoxy is set the tape is removed and the block is fixed into a polishing jig using modelling wax as shown in figure 4.2. The trailing ends of the optical fibre are wound around the central recessed section of the jig and taped or held in place using Blu-Tak to protect it during polishing. It is important that the fibre should be easy to unravel from the jig to facilitate coupling into an experimental system before the polishing process has been completed.

The Logitech polishing machine shown in figure 4.3 consists of a horizontal rotating wheel, an arm to hold the polishing jig and a polishing slurry feed system. There are two polishing wheels available for different applications. A cast iron polishing wheel is used to remove large quantities of material and a polyurethane wheel is used to 'fine-polish' the surface of the finished block. The polishing jig is kept in place by a semi-circular arm and the motion of the polishing wheel. The arm can move from side to side ensuring that all of the wheel is used during polishing. Continuous polishing using only one area of the wheel causes the wheel to loose its flatness. The final section of the machine is the rotating drum mechanism which is used to deposit polishing slurries onto the rotating wheel.

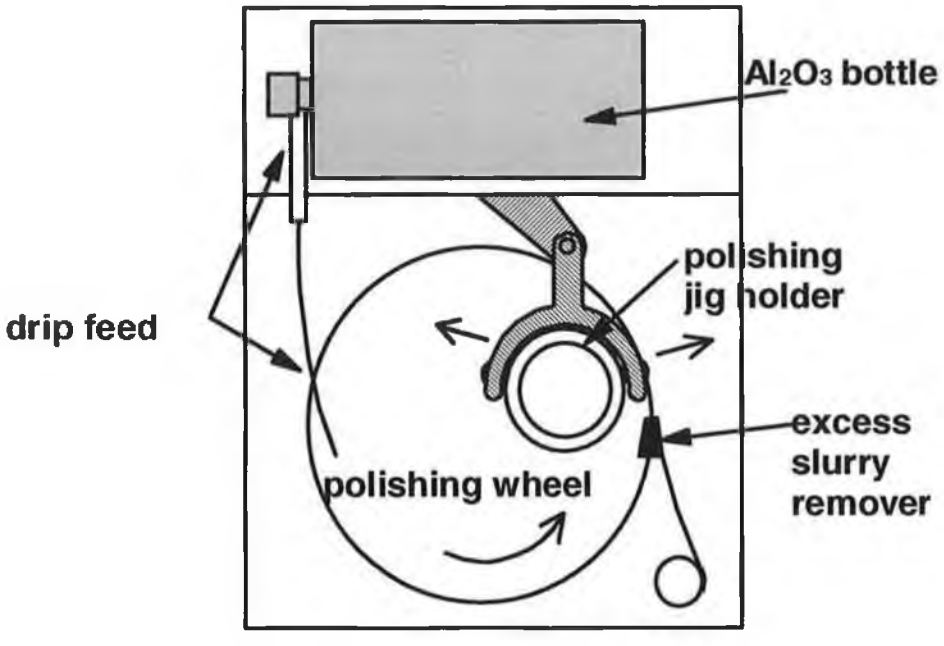

figure 4.3 Logitech PM2A polishing and lapping machine plan view.

The epoxy removal rate is a function of the size of the slurry particulates, the rate of rotation of the wheel and the amount of force exerted on the block. It also depends on the hardness of the epoxy which is related to the amount of hardener used. Polishing was performed in 4 phases. Firstly, the layer containing bubbles was polished rapidly using a very coarse 60μm Al_2O_3 powder suspended in water. This was deposited manually using a plastic pipette because there was no rotating drum feeder available for it. This slurry had to be stirred constantly because it sedimented very quickly. When the epoxy layer had been reduced to approximately 2 mm at its thinnest point, a 9 μm Al_2O_3 slurry was used. The 9 μm slurry was used until the cladding was reached and then replaced with a 3 μm Al_2O_3 slurry. Optical measurements were performed at this stage to determine the degree of access to the evanescent field. These consisted of measuring the transmission of the side-polished fibre when coated with a layer of absorbing liquid. The 3 μm slurry was used until a measurable evanescent absorption signal was recorded when the block was coated with a thin layer of isopropanol (IPA). IPA (i-C_3H_7OH) absorbs strongly at 3.4 μm. At this point the steel wheel was replaced with the polyurethane wheel and a 0.125 μm polishing suspension was used. The feed rate for the 0.125 μm suspension was controlled by constricting the flow tube of a gravity feed system. The 0.125 μm suspension crystallises in air and care had to be taken to ensure that it did not crystallise on the polishing wheel and cause damage to the fibre. Repeated experimental measurements of the sensors sensitivity as an ATR device were taken while polishing with the suspension. This is the most critical stage of the sensor fabrication process as each measurement requires extensive handling of the fragile fibre. To take a

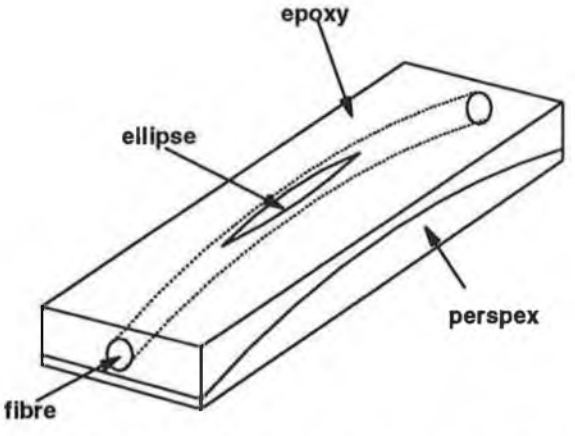

figure 4.4 polished fibre in polishing block showing cladding ellipse

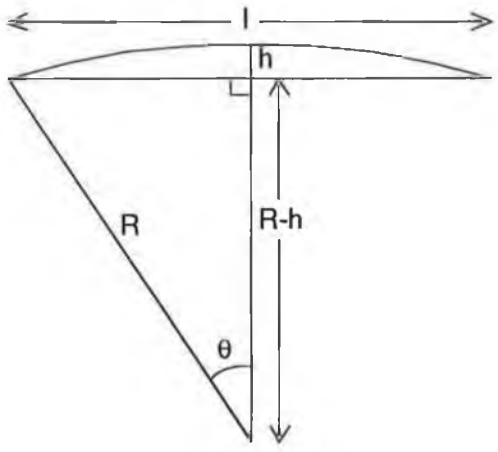

figure 4.5 geometry for polishing depth measurements

complete set of results the fibre may have to be unwound and rewound up to 30 times. The polishing procedure is continued until a desired cladding thickness remains.

4.2.2 Polishing depth calculation

Calculation of the thickness of the remaining cladding layer is based on measurement of the exposed optical fibre cladding ellipse as shown in figure 4.4. To reduce the possibility of polishing completely through the cladding while using coarse slurries two early warning indicators are used. As previously mentioned, the dyed epoxy can be visually distinguished from the perspex substrate. Visual measurement of the remaining epoxy layer indicates the proximity of the fibre to the polished surface. Secondly, as the fluoride fibre protective coating has not been removed and can be distinguished from the epoxy by virtue of the dye, observation of this polished ellipse provides another more accurate early warning of the proximity of the cladding.

The depth of polish into the cladding is calculated from the simple geometry shown in figure 4.5. The ellipse length l (measured) and the radius R of the perspex block determine the polish depth h by the equation.

$$h = R - \sqrt{R^2 - \frac{l^2}{4}} \qquad 4.1$$

This method of determining the remaining distance to the core assumes that the optical fibre core and cladding are concentric. The manufacturers of the 11/125 μm monomode fluoride fibre (Le Verre Fluore, France) used in the polishing process quote a maximum concentricity error of 5 μm. While the values for the polish depth obtained by the ellipse

method are not absolute measurements of overlayer thickness, they represent the relative decrease in overlayer thicknesses with absolute (systematic) errors of the order of microns.

4.2.3 Conclusion

Using the polishing technique described above for fluoride fibre, a very high success rate was achieved. Very little of the damage that occurred to fibres during the polishing process was as a direct result of the polishing or lapping procedure. However, due to the fragility of the zirconium fluoride glass a high incidence of breakage occured during the fabrication proceedure. Breakage was normally a result of the repeated handling received by the fibre during absorption measurements. Automated production of these devices could be achieved by using infrared laser diodes or LEDs and detectors to monitor the throughput of the block during the polishing process [7]. Such sources are not currently available on a commercial basis in the wavelength region of monomode operation of fluoride fibres. Monitoring in the near-infrared where the fibre is multimode may provide a short term answer but would not provide the repeatability of monomode operation because of possible fluctuations in the modal power distribution.

4.3 Tapering.

4.3.1 Introduction.

Tapering optical fibres involves the simultaneous heating of the fibre to the glass molten point and the application of a tensile stress along the fibre axis. The procedure is similar to the fibre preform drawing process where a preform of centimetres in diameter is heated and pulled to reduce it to an optical fibre waveguide of a few hundred microns in diameter. If the heated region is at the molten glass temperature and the fibre is pulled at the appropriate rate, the fibre will taper as shown in figure 4.6. Figure 4.6(a) shows an idealised taper geometry and a typical evolution of the modal field in a tapered single mode fibre. Figure 4.6(b) shows a more realistic taper geometry which is similar to those obtained experimentally.

As the diameter of a fibre reduces, the modal field distorts to satisfy the new boundary conditions. The supported modal field is found by obtaining the local mode solution for the fibre at each point along the taper. These fields are represented in figure 4.6(a). In section 3.3 it was shown that as the core diameter of the fibre is reduced the fundamental mode becomes 'cut-off' i.e. it is no longer guided by the core. This mode has become a cladding mode i.e. it is guided by the cladding / air interface provided a guided local mode solution exists for this boundary. In effect the field is no longer evanescent in the fibre cladding. In order to achieve a lossless taper, the rate of field distortion and the transition of a core mode to a cladding mode in a taper must meet the following general criterion called the adiabatic condition, '*the fibre nonuniformity must change over a distance large compared with* z_b', where z_b is the beat length, $2\pi/|\beta_1-\beta_2|$, between a pair of modes [8]. As the fibre diameter increases on the far side of the taper waist, the cladding modes are recaptured and become core modes. If the fibre taper is not adiabatic some of the power in the fibre modes will be coupled into higher order modes that are not recaptured by the fibre on the far side of the taper waist.

Tapered silica fibre devices are commonly used and have superseded polished fibre couplers. Tapered couplers are made by tapering the required number of fibres in the one flame until the fibres fuse and the desired coupling ratio is achieved. Cohesion is ensured by twisting the fibres in the tapering flame. Tapered couplers are less prone to temperature drift than their polished counterparts and they can be fabricated as multiport devices with accurately controlled coupling ratios and a flat wavelength response. Tapered couplers have reduced the market for polished couplers to applications where variable coupling ratios are desired.

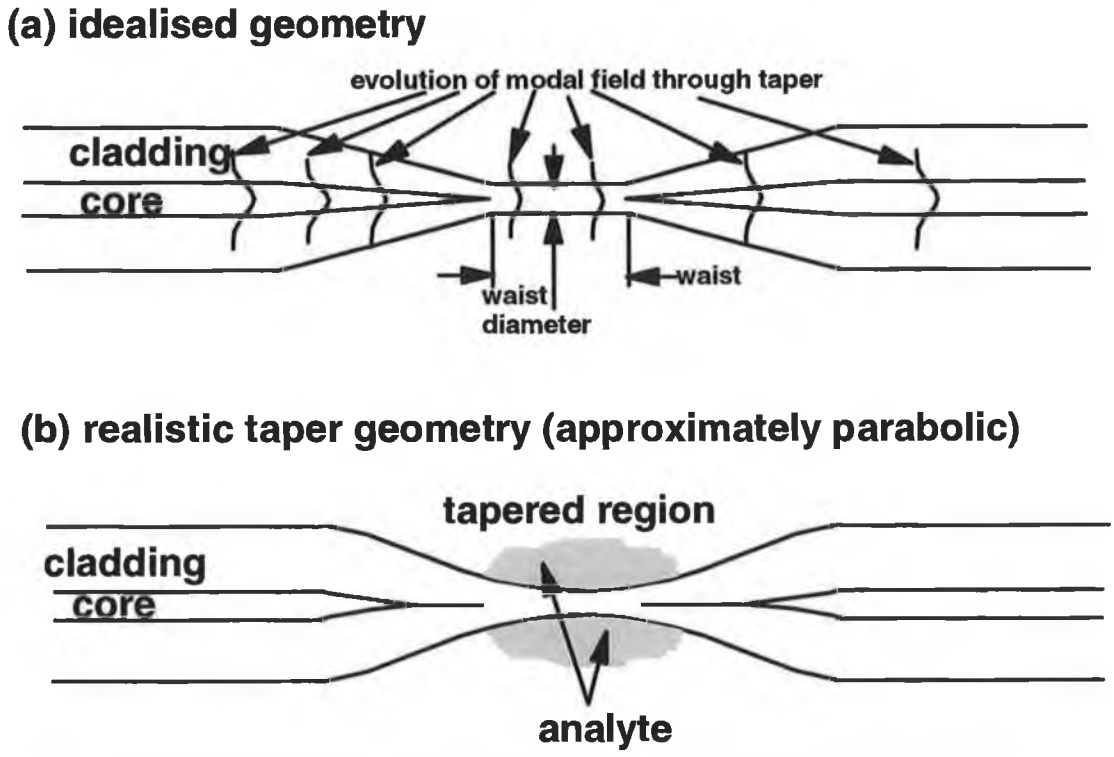

figure 4.6 longitudinal geometry of optical fibre tapers: (a) an idealised representation showing a representation of the evolution of the modal field for a single mode taper, and (b) realistic taper geometry.

In a manner similar to the semi-coupler described earlier, a tapered fibre may be used for evanescent wave sensing. The tapered region acts as the sensor as the evanescent field may extend into the analyte as shown in figure 4.6(b). The sensitivity of a tapered evanescent wave sensor is determined by (i) the taper diameter at the waist, (ii) the length of the waist and (iii) the wavelength of operation. Factors (i) and (iii) may be evaluated together if the V-number of the tapered section of fibre is used as a parameter for determining sensitivity. Sensitivity increases with decreasing waist diameter, increasing waist length and increasing wavelength.

The waist of a taper is the region over which the taper diameter is uniform as shown in figure 4.6(a). The taper waist length is determined by the width of the heat source and in the simplest model they are assumed to be identical. Burns *et al.* [9], using a parabolic model for the taper shape and assuming a constant fibre volume during tapering, showed that the effective heater size is smaller than its physical dimensions. Using the same

model they also showed that the maximum pull length for the fibre before breaking was 5 times the effective furnace length. This was supported by experimental data in the same paper.

A tapered optical fibre methane sensor using silica fibre was reported by H. Tai *et al.* [1] in 1987. The sensor used multimode silica fibre, tapered to a minimum diameter of 1.8 μm, and a 3.392 μm HeNe gas laser source. Using this sensor these workers achieved a minimum detectable concentration of 1% methane which is well below the lower explosion limit (LEL) of 5%. The silica fibre used had a loss of $91dBm^{-1}$ at the HeNe laser wavelength and as a result could not be the basis of a practical remote or distributed fibre sensor. A practical tapered sensor for flammable gases would require the use of low loss fluoride fibre.

4.3.2 Tapering methods

Fluoride fibre tapering techniques are not as developed as those for silica fibre and there is little detail in reported literature. The first reported tapering of multimode fluoride fibre for the fabrication of fluoride fibre couplers was reported by Rowe *et al.* in 1990 [10]. An exact duplication of the silica fibre tapering process is not possible with fluoride fibres as fluoride glass has a much lower glass transition temperature (~280°C) than silica-based glass (~1000°C). Consequently heat sources, such as a butane flame which can be used to melt silica fibres for tapering, may not be applied directly to fluoride fibre. A different type of heat source is required for fluoride fibre tapering. The first requirement in the development of the fluoride fibre tapering rig was the identification of such a suitable heat source. Two sources were initially considered: a resistive heating source consisting of a coiled length of tungsten wire and butane gas burners used indirectly. The butane burners had been used successfully to taper multimode silica fibre in a vertical tapering configuration similar to that shown in figure 4.7 [11].

4.3.2(a) Vertical tapering

Experiments to compare these heat sources were performed on a vertical taper rig. One end of the fibre was fixed and a small mass (approximately 5g) was attached to the other. The weight was found to provide enough tension to taper the heated fibre. The butane flame was used to heat a metal shield placed around the fibre. To provide as uniform a source as possible to taper the fibre two portable gas burners (Portasol, Oglesby & Butler, Ireland) were used as shown in figure 4.7. A small number of tapers were pulled using this source, but it became rapidly apparent that accurate temperature control was impossible. The temperature of the tapering region using the butane burners in this configuration depends on too many variables. These include the tube diameter, the flame to tube distance and the flame temperature. Using the flame source tapers were made by allowing the temperature in the

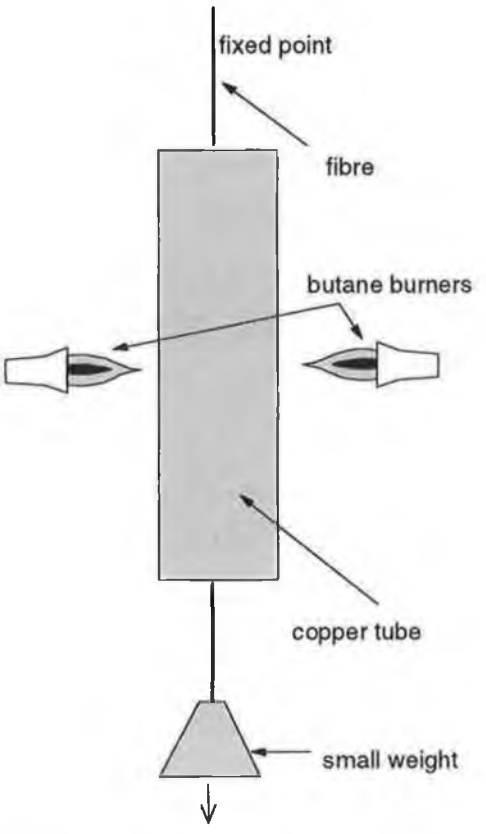

figure 4.7 horizontal tapering of fluoride fibre using a copper shield and a butane flame source.

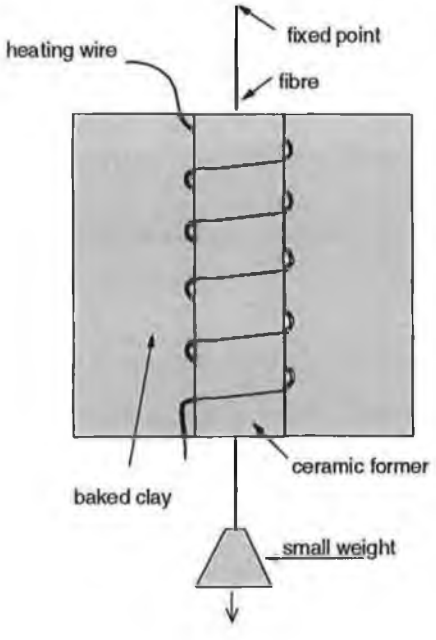

figure 4.8 initial resistive tapering rig for source and fibre evaluation

tapering region to ramp through the tapering temperature slowly and by decreasing the heat once tapering had begun.

The second source, a tungsten wire resistive heater, was also studied in a vertical tapering rig, depicted in figure 4.8. The temperature in the tapering region was controlled by means of a high current variable voltage source. The heating element is wound around a hollow ceramic former, 5mm in diameter. The fibre to be tapered passes through the centre of the former. The position of the fibre is critical in ensuring that the temperature is uniform across a section of fibre. In figure 4.10 the maximum temperature within the ceramic former is plotted as a function of the voltage applied across the resistive heater. Voltage is plotted instead of current because the power supply does not accommodate direct current control. The resistance of the element was measured to be 12Ω at room temperature.

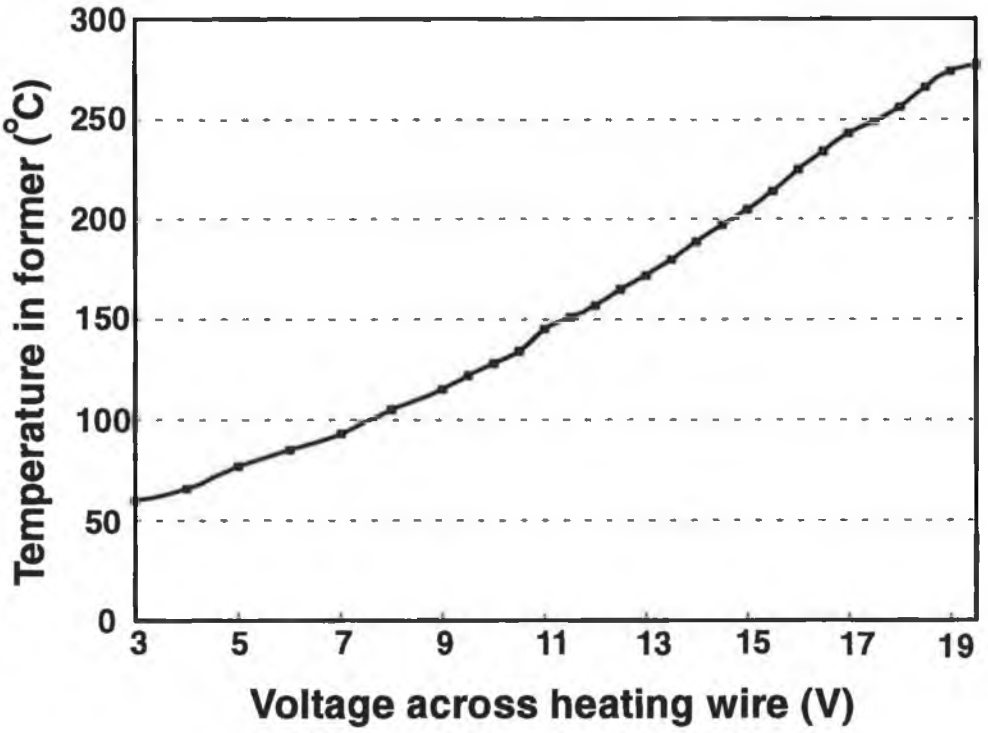

figure 4.9 voltage vs temperature for resistively heated vertical tapering rig

The tapering temperature was estimated by placing a fibre in the tapering rig and increasing the applied voltage from 15 volts in 0.1 volt steps until tapering occurred. Tapering was observed to occur between 17 and 18 volts for a range of fibres. The tapering temperature of the fluoride fibre may then be measured from figure 4.9. The tapering voltage range corresponds to a temperature range of approximately 240-260°C which is very close to the glass transition temperature (≅260°C) quoted for fluoride fibre by Rowe *et al.* [10]. The tapering temperature is lower than the quoted melting point of the fluoride glass, 310°C (Le Verre Fluore). Feedback control of the temperature within the former was not implemented at this stage. Ambient temperature fluctuations did not significantly affect the temperature within the former. Accurate positioning of the fibre within the ceramic former is critical to ensure that the conditions are identical for all tapers pulled. Above 18 volts the fluoride fibre tapers rapidly and breaks. This is possibly due to the low viscosity of fluoride glasses which drops rapidly with increasing temperature.

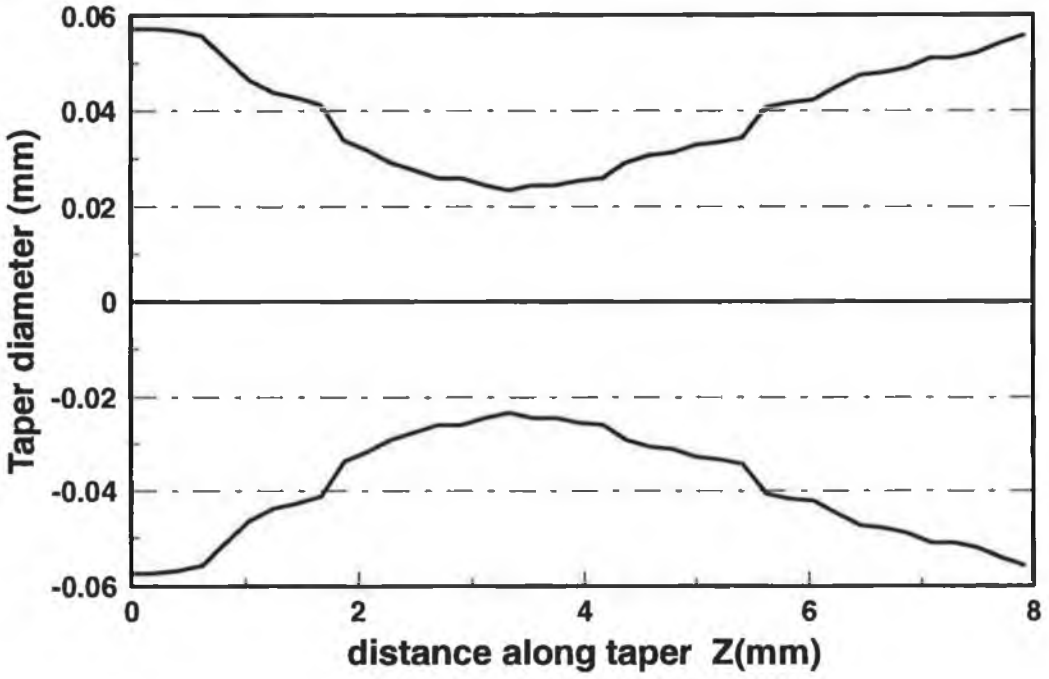

figure 4.10 profile of taper made with the resistive wire tapering rig

Figure 4.10 shows the spatial profile of a typical taper pulled with the vertical tapering rig. The profile was measured by photographing sections of the taper at x40

magnification with a microscope (Nikon type 104). A number of features common to these tapers can be seen in the graph. Firstly, the taper is asymmetric about its narrowest point or waist. This feature may be explained using a simple constant volume model as shown in figure 4.11. A length of fibre, dz, is heated to the glass softening temperature and pulled a distance dl. The diameter of the pulled region is reduced to maintain a constant volume. A schematic of the model shown in figure 4.11 for symmetric and asymmetric stretching, shows, respectively, the resultant symmetric and asymmetric taper shapes. The asymmetric stretching model leaves one end fixed with respect too the heating zone, as is the case for the fixed point vertical tapering system. As the incremental tapering length, dl, is decreased, the taper shape predicted by the model is smoothed. The model is unable to accurately predict the profile of the asymmetry. This is due to the heating effect of the source which is assumed not to heat the fibre outside the section dz. The model uses a step function to model the temperature profile within the tapering region and, as a consequence, predicts a constant diameter for the taper in the waist region of length dz equal to the heater length. A profile of the temperature distribution in the former generated by the heater is shown in figure 4.12. It is clear from this figure that although the source is 5cm in length the effective length of the source is much less than this. It is also evident that the model of the source as a step function is not valid. Consequently, one would not expect to see a flat taper waist in this system.

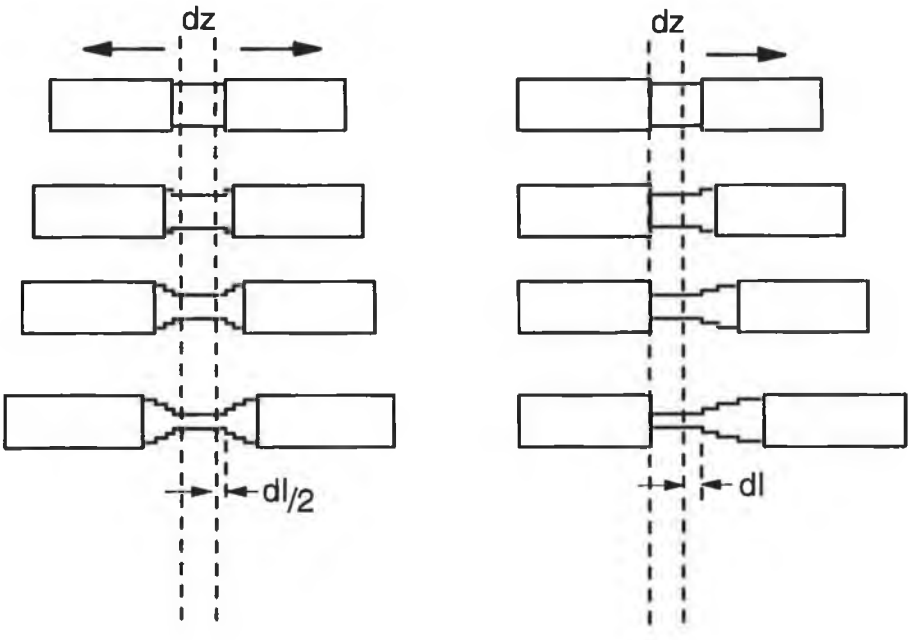

figure 4.11 simple constant volume taper model for symmetric and asymmetric tapering.

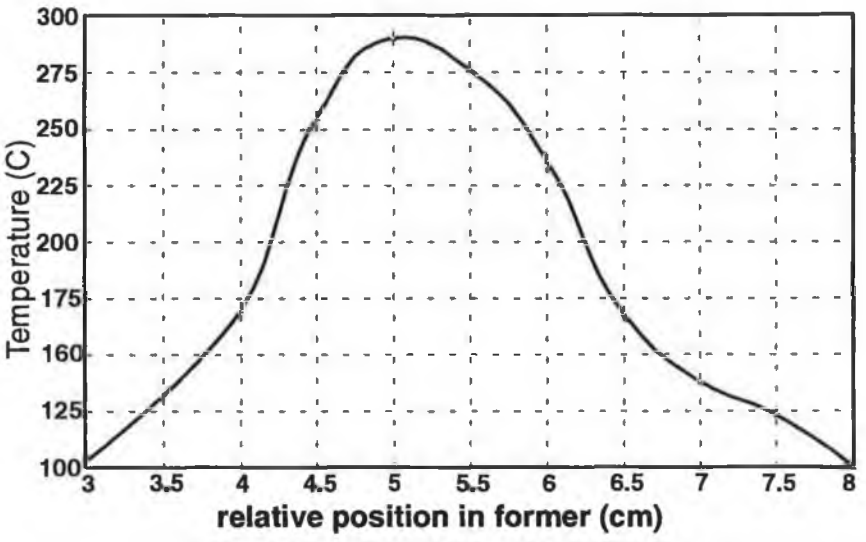

figure 4.12 spatial distribution of temperature within vertical tapering rig

A second model, the constant volume parabolic model, has been used to estimate the effective size of the source (dz). A maximum taper length of L = 5dz is predicted by this model [9]. For example, using the taper diameter reduction ratio from figure 4.10, Df/Di = 0.407 (where Df is the minimum taper waist diameter and Di is the untapered fibre diameter), and a taper length L of 9.16 mm (twice the longest side of the taper), the parabolic model gives a value for dz of 3.36 mm. Figure 4.13 shows the theoretical taper profile generated by this model. The figure also shows the profile generated by the simple constant volume model of figure 4.11 and the taper data from figure 4.10. Use of the value for dz predicted by the parabolic model in the simple model, while keeping L constant, yields a diameter reduction ratio of 0.65. To obtain the correct reduction ratio (0.407) and to generate the profile shown in figure 4.13 the waist length dz was allowed to vary. A value for dz of 2 mm gave the correct reduction and was used to generate the profile shown using the total taper length of 9.16 mm.

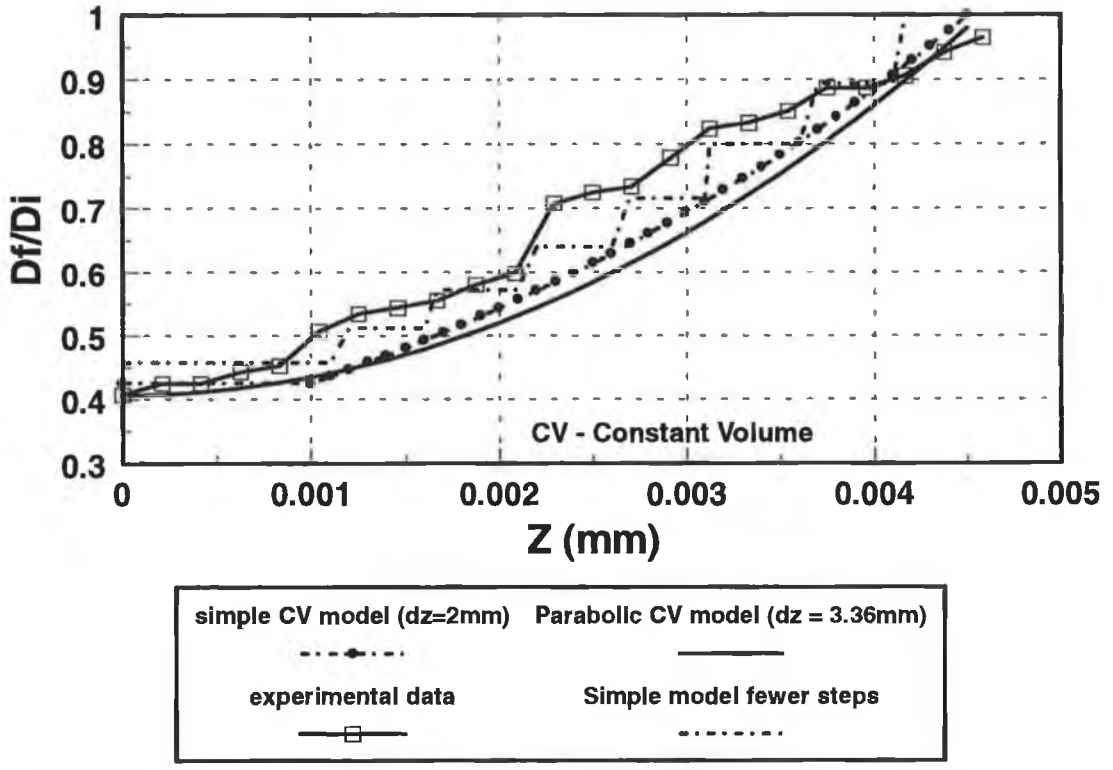

figure 4.13 comparison of simple constant volume model and parabolic constant volume model

An additional feature of the taper shown in figure 4.10 is its irregular profile. The structure is almost periodic and suggests that the fibre did not taper at a constant rate. The regular structure observed is very similar to the structure predicted in the simple theoretical model outlined above where dl is not small. For example, the simple model data in figure 4.13 are plotted where for dl = 0.5 mm and it produces a better fit to the data than the other fits. The value dl = 0.5 mm was chosen because the periodicity in the taper was of that order. The reason why the tapering should result in such a profile is not known. Although it may be directly related to the vertical tapering configuration. The proposed explanation is as follows. The fibre is heated and becomes soft enough to be stretched by the constant applied tension. In the vertical system, the hottest section of the fibre is constantly being pulled out of the hottest section of the former. This may reduce the fibre temperature sufficiently to stop the fibre tapering at this point. This explanation is equivalent to the source of heat moving slowly in one direction in a symmetrical tapering rig.

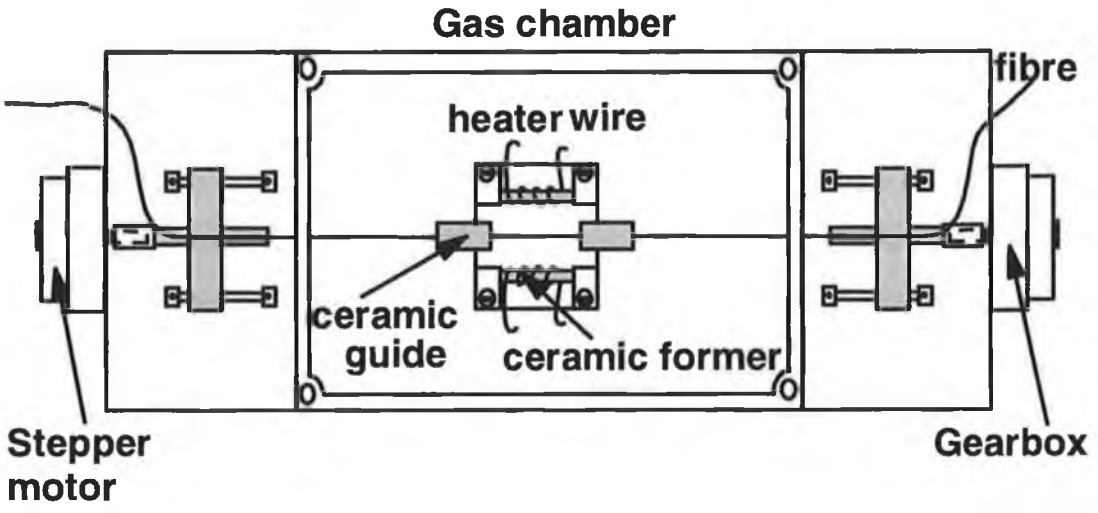

figure 4.14 horizontal computer controlled tapering rig with resistive heating elements

4.3.2(b) Horizontal tapering.

In an attempt to achieve symmetric fibre tapers, a horizontal tapering rig was designed and built. The rig is depicted in figure 4.14. The fibre pulling mechanism consists of 2 stepper motors attached to 1:25 ratio gear boxes. The heat source consists of 2 resistive heaters placed on opposing sides of the fibre. The fibre is guided through small ceramic tubes at either end of the tapering area. The tapering area, or furnace length, is between 3 and 4 cm. The fibre is not enclosed so that it can be observed by microscope during the tapering process. The fibre platforms are coupled to the motors through a threaded bar with 0.8 mm pitch. The 1:25 ratio gearboxes give an effective step angle of 0.3° which corresponds to a lateral movement of 1.3μm per stepper motor step (770 steps/mm). The stepsize is sufficiently small to ensure a smooth pull without requiring too high a stepper motor speed. At higher step rates the stepper motor torque decreases rapidly [12] and can result in missed steps or jamming of the tapering rig. The resistive heater furnace is contained in a sealed box with a removable lid so that the evanescent

absorption sensitivity of a taper to gases can be investigated without the problem of moving the very fragile tapers.

The system is controlled by the voltage on the high current power supply. The tapering process is no longer passive and the following tests were required to determine the optimum operational parameters such as heater voltage and tapering speed. The voltage corresponding to a temperature of 250°C was measured using a temperature probe and this was used as the starting point in ascertaining the tapering parameters for this system. This voltage was measured to be 3 volts across the two coils which have a resistance of 1Ω each and are wired in parallel. No tapering was observed at this voltage even at the slowest of tapering speeds of 0.1 mm/min. Tapering was observed at a minimum probe temperature of 300°C (4.5 volts). This temperature is much greater than that measured in the vertical tapering system. A possible reason for the discrepancy is the transparency of fluoride fibre to radiant heat energy which the probe absorbs readily.

The fibre inlet and outlet holes were sealed which made it extremely difficult to remove the fibres intact for measurement and inspection with a high quality microscope. None of the tapers made in this rig were examined under such a microscope. Using the maximum taper pull lengths recorded and the parabolic constant volume model certain taper parameters may be estimated. The taper parameter of interest, from which all others may be inferred, is the effective furnace length. The effect on this parameter of the proximity of the heat source to the fibre is shown in table 4.1. Moving the heaters nearer to the fibre, by a factor of two, increases the taper lengths and effective furnace length by more than a factor of two. The calculated maximum effective furnace length is approximately one quarter the actual heater length. This is a better ratio than is obtained for the vertical tapering system where the total furnace length is between 4 and 5 cm while the effective furnace length is approximately 3.4 mm.

Configuration	pull length (mm)	average (mm)	effective furnace length (mm) [9]
2 x resistive heaters equidistant from fibre (2 cm)	20	19.5	4
	21.3		
	17.3		
2 x resistive heaters equidistant from fibre (1 cm)	52	46	9
	56		
	31.2		

Table 4.1 Total taper pull lengths before breaking.

4.3.3 Conclusion

Using the horizontal and vertical tapering methods a maximum taper reduction ratio of approximately 0.4 was achieved. This ratio is similar to that published for multimode fluoride devices [10]. This work has been continued in a flowing argon gas atmosphere using feedback in the temperature control circuits [13]. The gas is used to aid heat transport to the largely IR transparent fluoride optical fibre. Although further work is required to produce single mode fibre capable of sensing gases, the technology reported here is capable of tapering multimode tapers for enhanced evanescent wave sensitivity.

4.4 Comparison of fabrication techniques

The structures produced by polishing and tapering have very different properties. Polished fibre sensors require are very time consuming to fabricate. Before the procedure was optimised a single sensor could take up to 2 weeks to polish. Fabrication time was reduced to 2 days during the course of the work. The polished fibre sensing structure is very robust because it is firmly fixed in an epoxy resin. In contrast, the tapered sensor can be fabricated in less than half an hour but the final structure is very fragile. The failure rate for tapers is higher than for polished blocks despite the repeated handling that the polished sensors undergo during the sensitivity measurement and

repolish process. In the next chapter the apparatus used to measure the evanescent wave sensitivity of the sensors fabricated, as described in this chapter, is discussed. In addition, apparatus used to characterise multimode fibre sensors is described.

1. Tai H., Tanaka H., and Yoshino T.: '**Fibre-optic evanescent-wave methane-gas sensor using optical absorption for the 3.392-μm line of a He-Ne laser**', Optics Letters, 1987, Vol. 12, No. 6, pp. 437-439

2. Lew A., Depeursinge C., Cochet F., Berthou H., Parriaux O.: '**Single-mode fibre evanescent wave spectroscopy**', 2nd International Conference on Fibre Optic Sensors, Stuttgart, 1984, pp. 71-4

3. Ruddy V., McCabe S., and MacCraith B. D.: '**Detection of propane by IR-ATR in a Teflon-clad fluoride glass optical fibre**', Applied Spectroscopy, 1990, Vol. 44, No. 9, pp. 1461-3

4. Digonnet M.J.F., Feth J.R., Stokes L.F., Shaw H.J.: '**Measurement of the core proximity in polished fiber substrates and couplers**', Optics Letters, 1985, Vol. 10, No. 9, pp. 463-5

5. Zafirova B.S., Panajotov K.P., Andreev A.Tz.:'**Temperature-stable polished fibre-optic coupler**', Optics & laser technology, 1992, Vol. 24, No. 6, pp. 345-7

6. Sorin W.V., Kim B.Y., Shaw H.J.: '**Phase-velocity measurements using prism output coupling for single and few-mode optical fibres**', Optics Letters, 1986, Vol. 11, No. 2, pp. 106-8

7. Nicholls S.T.:'**Automatic manufacture of polished single-mode-fibre directional coupler**', Electronics Letters, 1985, Vol. 21, No. 19, pp. 825-6

8. Snyder A.W., Love J.D.:'**Optical waveguide theory**', Chapman & Hall, 1991

9. Burns. W. K., Abebe. M., Villarruel C. A.: '**Parabolic model for shape of fibre taper**', Applied Optics, 1985, Vol. 24, No. 7, pp. 2753-5

10. Rowe C. J., Moore M. W., Wilkonson I. J., Achurch N. E.: '**Fused taper couplers in multimode Fluorozirconate fibre**', Electronics Letters, 1990, Vol 26, No 5, pp. 316-8

11. Cryan C.: '**Optical Fibre Refractometer**', Dublin City University, Undergratuate thesis, 1989.

12. RS stepper motor data sheet, 1987 No.8199

13. O'Dwyer K.: '**Development of infrared evanesvent wave fibre sensors using an FTIR spectrometer**', Dublin City University, Thesis presented for degree of Master of Science 1993.

Chapter 5 Experimental Systems

5.1 Introduction

In this chapter the requirements of experimental systems to measure the sensitivity of optical fibre evanescent wave (EW) sensors operating in the IR region from 3-5 μm are discussed. The components used in these systems are introduced under various headings including source, detector and monochromator. The software and electronics written to control the equipment and collect the data are detailed in Appendix D. The combination of components used with each of the sensors fabricated in this work are detailed at the end of the chapter. The experimental systems are described in this manner to demonstrate flexibility and the particular strengths and weaknesses of each individual component in relation to individual fibres.

The experimental systems are required to measure the sensitivity of the fibre EW sensors, fabricated by the processes outlined in chapter 4. To measure sensitivity, the spectral transmission of the sensor is measured in the absence of an absorbing species, $I_o(\lambda)$, and then in the presence of one, $I(\lambda)$. From these data a transmission or absorption spectrum of the analyte can be calculated where

$$\text{Transmittance}(\lambda) = \frac{I(\lambda)}{I_o(\lambda)}$$

and

$$\text{Absorbance}(\lambda) = \log_{10}\frac{I_o(\lambda)}{I(\lambda)}$$

By comparing absorption the EW device with the absorption of the same analyte in a direct transmission cell from which bulk absorption coefficients are measured the efficiency of the EW device may be calculated. The efficiency is represented as the ratio of the absorbtion coefficient for the EW device ratioed to the absorption coefficient in a open cell of a equal interaction length.

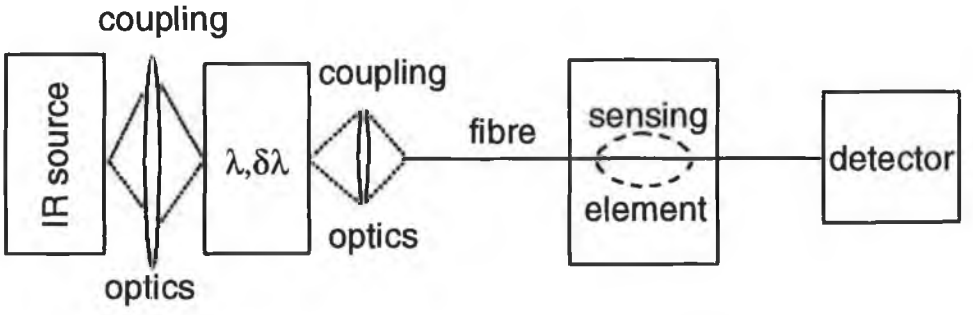

figure 5.1 generic experimental system

The experimental system of figure 5.1 contains all the elements required to measure the sensitivity of a fibre sensor. The system consists of an infra-red source coupled via a monochromator to a length of optical fibre a region of which operates as the sensor. The end of the fibre is in turn mated to an infra-red detector. The experimental system not only provides sensitivity information for the EW sensors but can also be used to test the suitability and performance of various infra red devices such as detectors and sources.

5.2 Infra-red sources.

For this work the radiation source must satisfy a number of requirements. The spectral output must overlap with the C-H vibrational and rotational absorption lines in the 3-4μm region of the electromagnetic spectrum. As the source output must be coupled into an optical fibre the source emission area should ideally be comparable to the fibre core area. The source output should be stable spatially and temporally. Low power consumption and long life are essential for possible commercial uses but not necessary for experimental purposes.

Solid state sources are ideal for use with fibres and are used extensively in the visible and near infra-red. Mid-IR solid state sources are not as advanced as the visible/NIR devices. Commercially available laser diodes that cover the 2-4μm region of the optical spectrum are fabricated from lead salt combinations e.g. PbCdS. Such devices need to be operated at liquid nitrogen temperatures and below, may be wavelength tuned with difficulty, and, consequently, are not very practical sources for use in sensor systems. Light emitting diodes (LEDs) covering this region have been developed recently by various research groups [1,2,3,4]. Medium power room temperature operation LEDs suitable for flammable gas sensing are now available at reasonable cost. These sources were not available during the initial period of this work but will be discussed in section 6.5. Similarly, a fibre coupled Fourier Transform Infra Red (FTIR) spectrometer which became available at a late stage will be discussed separately (cf. section 5.6).

Apart from solid state diode sources, other available sources for this work fall into 2 distinct groups: gas lasers and broadband thermal sources. A Helium Neon gas laser which has an emission line at 3.392 μm is commercially available [5]. This matches exactly a line in the P branch of the rotational fine structure of the v_3 vibrational level of the C-H bond in methane. This laser line also lies within the broader absorption bands found in other hydrocarbon analytes relevant to this work e.g. propane, butane and IPA. The advantages of a laser source for fibre optic applications are many. Its small spot size and high power density simplify launching power into the fibre and detector requirements are minimised. The main disadvantage of the laser source is that absorption measurements are limited to a single wavelength. This does not allow a stable reference which is essential for any intensity based spectral absorption sensor [6]. In a controlled environment power fluctuations may occur due to drift in alignment and source instability. Normally it is necessary to compensate for such fluctuations by measuring the throughput at a nonabsorbing wavelength.

The broadband sources available for use in the mid infra-red are blackbody sources, glowbar and high power incandescent lamps (such as tungsten halogen). Blackbody

sources are primarily used as calibration devices and have low output powers unsuitable for the requirements of a fibre based sensor. The majority of glowbar sources have large emission areas with high total output powers that can not be coupled efficiently into optical fibres. A range of miniature glowbars are available that are more suited to coupling into optical fibres but do not have the output power density required for use with the smaller diameter fibres[3]. The most practical of the broadband sources tested was a high power tungsten halogen lamp. This source provides enough power for use with the multimode fluoride fibres of core diameters of 200μm or more.

In the following sections the sources used and the mode in which they were employed are detailed.

5.2.1 Helium Neon gas laser.

A 5 mW HeNe laser (PMS Electro Optics, Colorado USA) with two emission lines at 3.392 μm and 1.152 μm was used as the laser source. The 1.152 μm line is too far separated from the 3.392 μm line to be used as a valid reference signal. In addition it is outside the range of single mode operation of the fibre used. A long wavelength pass filter with a cut-on at 1.8 μm was used to filter out the 1.152 μm line. The 5mW total power is divided between the 2 laser lines with the 3.392 μm line having a power of 3 mW. A lens of focal length 6 mm was used to couple the laser radiation into the fibres as shown in figure 5.2. It is not easy to obtain a lens of such a short focal length fabricated from infra-red transmitting materials. Quartz, primarily for use in the ultra violet, has a narrow 90% transmission window in the infra-red that overlaps with the laser output wavelength. This feature greatly increased the range of lenses from which appropriate lenses could be chosen for work with the laser. The source was modulated for lock-in detection using a mechanical optical chopper (Bentham model 218) in conjunction with a computer controlled lock-in amplifier (Stanford Research SR510). Lock-in detection was required because of the high sensitivity of the detector to random changes in the

[3]All of the above comments must be qualified by noting that the detector used was a 3 stage TE cooled PbSe detector with a medium D^* of approximately 10^9

background infrared levels caused, for example, by people moving in the laboratory.

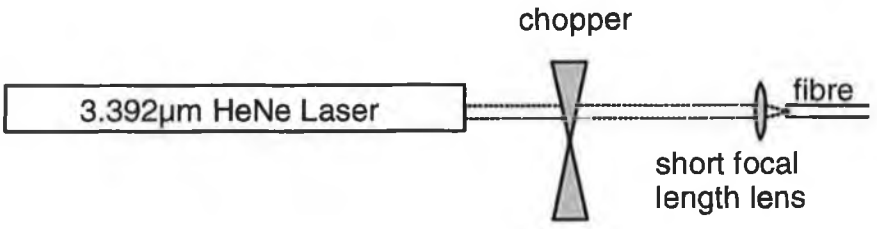

figure 5.2 infra-red laser launch setup

To determine the stability of the laser source, the output power of the 3.392 μm line was monitored from start-up using a PbSe detector. Initially, the output power exhibits periodic oscillations of up to 25% of peak power with a period of approximately 10 seconds. After allowing the laser to settle for 3 hours the oscillations reduce to less than 5% with a period of the order of 5 minutes. This behaviour is also observed when the laser is launched into multimode optical fibre. When the laser was used in conjunction with monomode optical fibre, however, more problematic behaviour was observed. Aperiodic oscillations of up to 80% of peak transmitted power were measured and these did not reduce with time. Initially it was assumed that the source was ageing and a beam splitter was employed to tap some of the output power in order to reference the oscillations. This approach showed that the total power of the laser line was stable to within 5% as previously observed. This suggested that the oscillations were due to spatial fluctuations of the laser output (beam wander). By placing a pinhole in front of the reference detector this was confirmed. With the pinhole in place the reference signal also exhibited large aperiodic oscillations. Unfortunately, it was virtually impossible to match the reference oscillations to those measured at the distal end of the optical fibre and so it was not possible to use the second detector as a reference during measurements.

The usefulness of the laser is limited by the aperiodic power fluctuations to the measurement of large absorptions that occur over timescales short in comparison with the laser oscillations. The HeNe laser is not suited to characterising monomode fibre

EW gas sensors where beam wander is more pronounced in its effects than for multimode fibres.

5.2.2 Tungsten Halogen lamp.

The tungsten halogen source used in this work had a total output power of 50W. The greater portion of this optical power is in the visible and near infra-red spectral region. As a result it is not ideal as an infra-red source. Furthermore the source area is large compared with the core areas of the optical fibres used and this factor reduces the power that can be launched. Using the chopper and lock in amplifier, detailed in section 5.2.1, in conjunction with a PbSe detector this signal is well separated from the noise. The source can not be used with single mode fluoride fibre, however, as the power that can be launched is too small to be detected by the PbSe detector lock in amplifier combination due to the smaller core diameter (11μm).

The lamp was housed in a custom made metal box and mounted in a ceramic holder as shown in figure 5.3. A 20 mm focal length infrared lens (Spindler & Hoyer IRGN6) was also mounted inside the box so that the light leaving the housing is approximately collimated. The optic axis is 45mm from the optical table onto which the housing was mounted to coincide with the optic axis of the monochromator (SMC1-06 Optometrics UK). The lamp is mounted in a ceramic base which is able to withstand the heat generated by the lamp. The lamp output power is stable over long periods. This stability was essential because, at low signal levels, the lock in amplifier prefilter time constant was set to 3 seconds or more and the total time

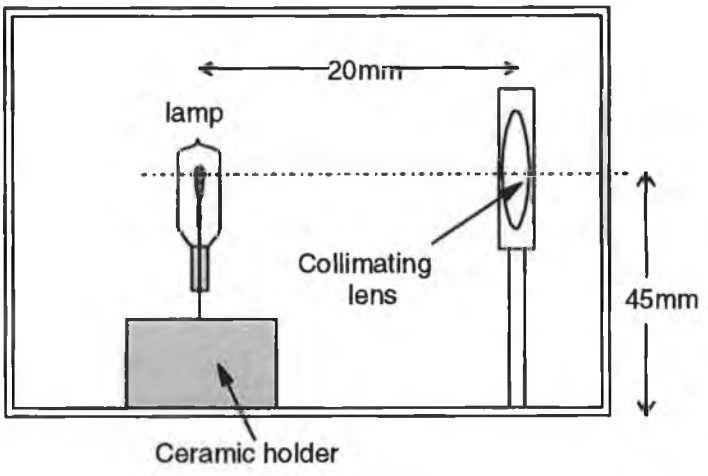

figure 5.3 50 Watt Tungsten Halogen lamp housing

required to take reference and absorption spectra was 30 minutes (sample scan 3μm to 4μm, 10nm steps, 5 seconds per point). New lamps were 'burned in' for a period of 2 hours before they were used to take measurements.

5.3 Infra-red Detectors.

The range of detectors available for the infrared is considerable as can be seen from the graph of D* vs wavelength in figure 5.4. The D* of a detector at the particular wavelength of interest is a good guide for choosing a detector. The D* of a detector is defined as $D^* = \frac{\sqrt{AB}}{NEP}$ where A is the active area of the detector, B the bandwith, and NEP the noise equivalent power of the detector. Other factors that need to be considered include response time, stability of response, cost, spectral response and cooling requirements. On the basis of cost, the thermoelectrically cooled lead selenide (PbSe) detectors give the best value and adequately cover the 3-4μm range. The response time of these devices is of the order of 20μs. Liquid Nitrogen cooled Indium Antimonide (InSb) detectors cover a similar spectral range with better detectivity and faster response times but are considerably more expensive.

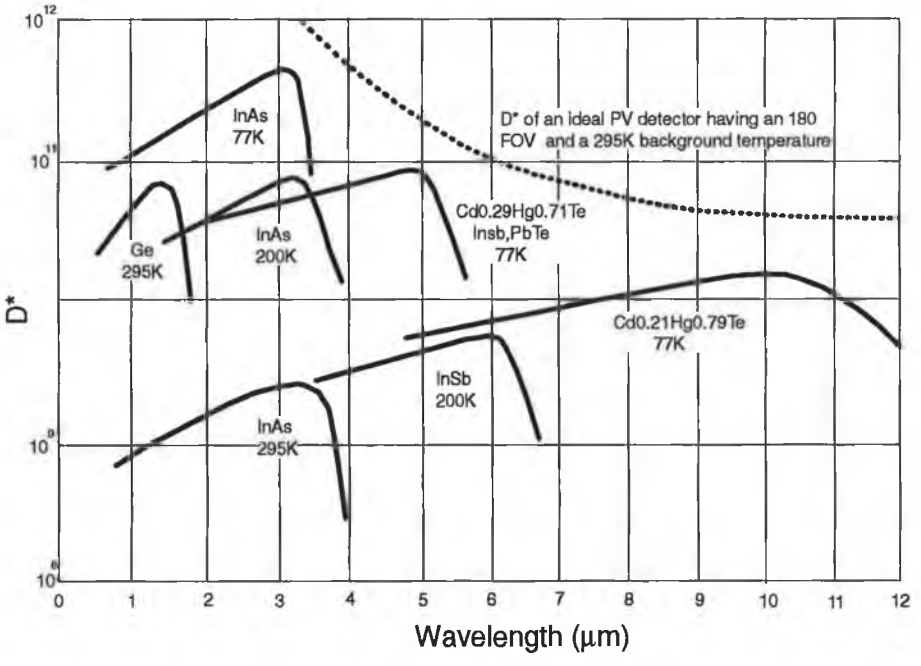

figure 5.4 graph showing the relative detectivities D* of various IR detector types.

Two detectors were used at different stages during the course of the experimentation. A thermoelectrically cooled PbSe (Infrared Industries, USA) detector was used initially. This detector was sufficiently sensitive for use with the tungsten halogen lamp source output coupled into multimode fibre with a lock-in amplifier used for signal averaging. A liquid nitrogen cooled InSb (Graseby Infrared, UK) detector was later obtained for use with a mid-IR LED. The InSb detector was used with the LED, which was operated in pulsed mode, because it offers a combination of high sensitivity and fast response time.

5.3.1 PbSe detector.

The PbSe (Infrared Industries, USA) detector that was used is a photoconductive device mounted on a three stage thermoelectric cooler. Figure 5.5 shows the basic electronic circuit for this detector. R_f, in figure 5.5, should equal the cooled resistance of the detector for maximum detector signal to noise ratio. The cooler is capable of cooling the detector to 80 degrees below ambient for an indefinite period providing the detector is mounted on a good heatsink. The heatsink is required to conduct the heat generated by the thermoelectric cooler away from the detector casing. The cooler has a maximum operating current of 1.4 Amps. During the long periods of operation required for the acquisition of multiple spectra, the detector responsivity was observed to decrease. This was due to the slow rise in the heatsink temperature when the cooler was operating near its maximum cooling current. The detector sensitivity is not linearly related to the temperature and this makes it difficult to compensate for this effect. It is much simpler to minimise the temperature drift of the detector. A fan was used to blow room air over the heatsink to stop it rising above room temperature and this provided sufficient stability. Figure 5.6 shows the effect of temperature drift of the detector on the signal at a single wavelength and figure

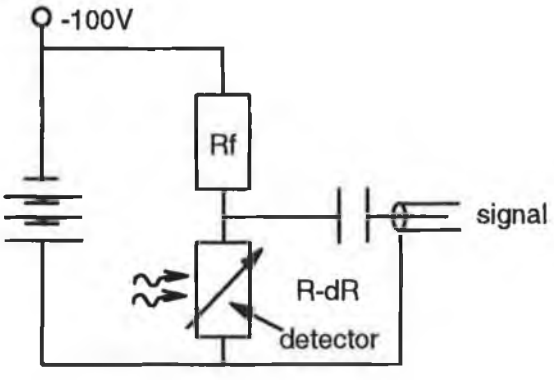

figure 5.5 PbSe photoconductive detector circuit

5.7 shows the stabilising effect that the fan has on the devices temperature. The temperature is measured using the thermistor that is mounted between the detector and cooler.

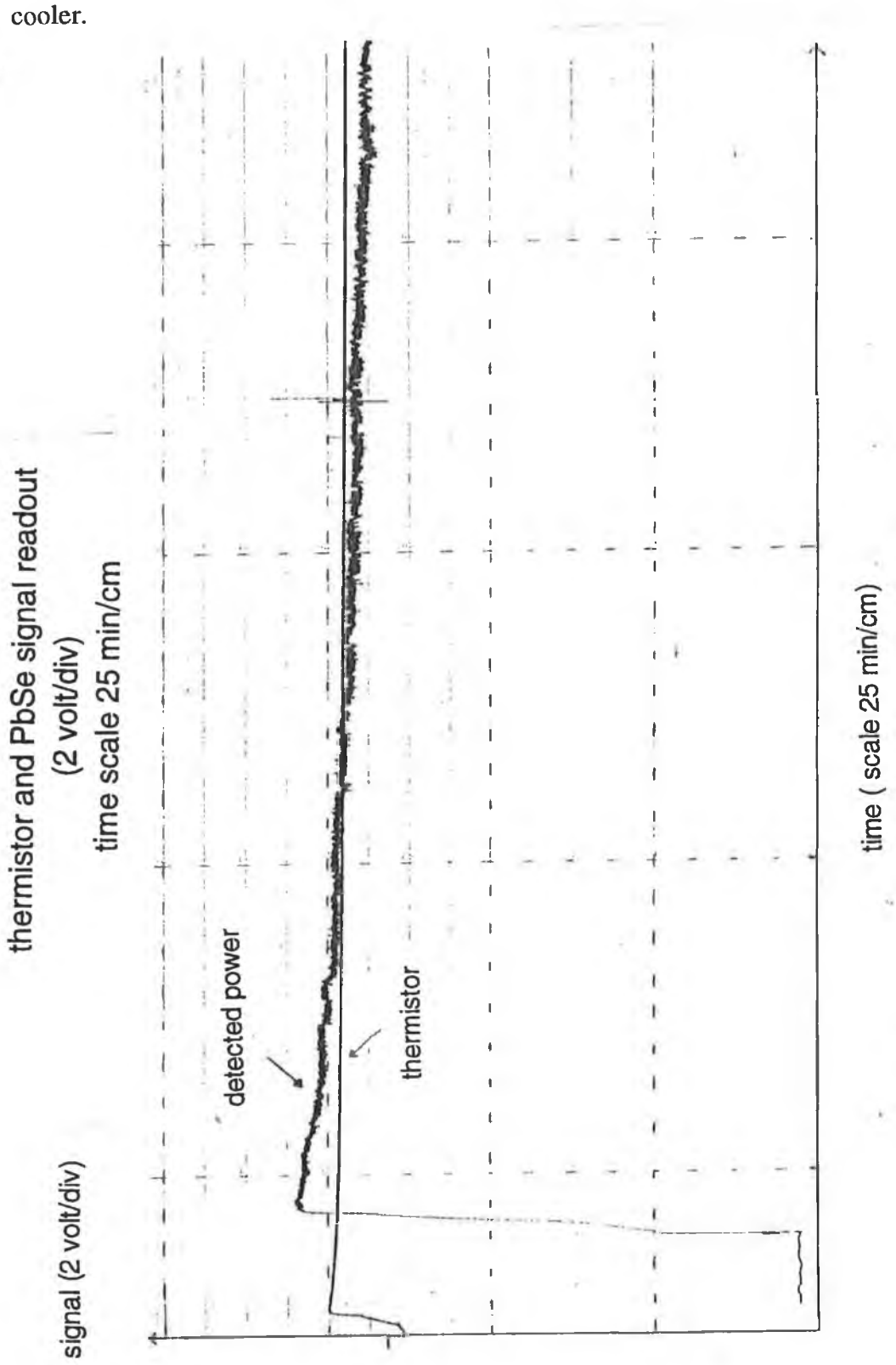

figure 5.6 PbSe detector drift due to insufficient heat dissapation of heatsink

figure 5.7 stabilising effect of fan on temperature of PbSe detector element

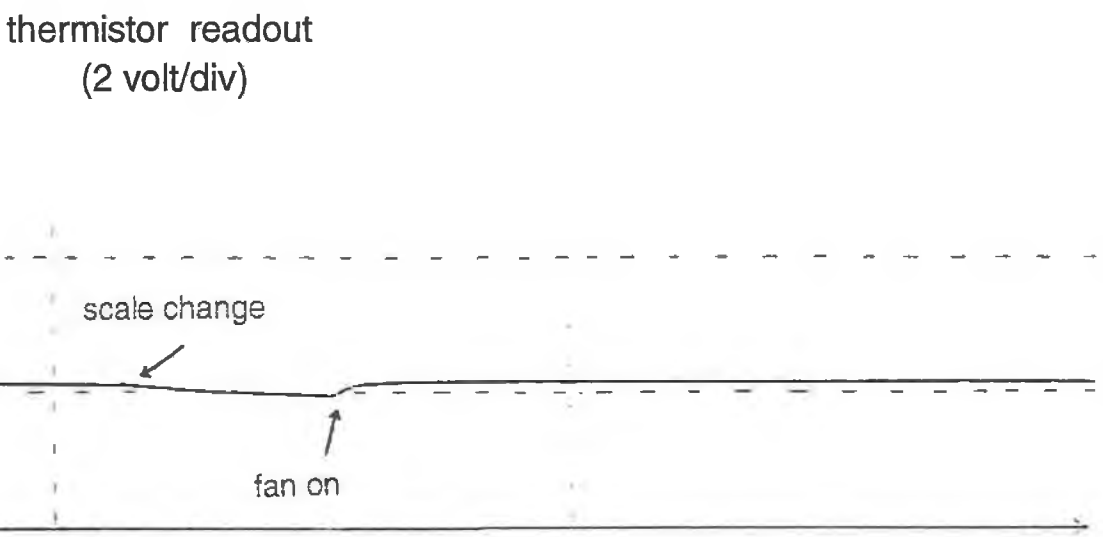
thermistor readout
(2 volt/div)
scale change
fan on

The basic circuit used to obtain an electrical signal from the detector is shown in figure 5.5. A second ac amplifier stage was added later to increase the signal and to minimise the noise by amplifying the signal close to the signal source. In order to minimise noise the 100 volt bias was provided by a series of 9V batteries rather than a variable high voltage source. The resistor R_f in figure 5.5 was chosen to match the resistance of the detector when cooled (3MΩ) as this gives the best conversion of photoconductive resistance change to ouput voltage.

5.3.2 InSb detector.

The Indium Antimonide detector supplied by Graseby Infrared is liquid nitrogen cooled with an active area of $4x10^{-4}cm^2$. This detector was purchased because it has a faster response time than the PbSe detector and a greater sensitivity. The detectors D* value is quoted as 3.65 x 10^{11} (cm $Hz^{1/2}$ $Watt^{-1}$). The dewar has a hold time of approximately 8 hours during which time the detector sensitivity is stable. The field of view of the detector is limited to 30° to reduce the background noise level. The detector responsivity peaks at 2.61 A/W at a wavelength of 3.9 μm. The response time of the detector unit is limited by the gain bandwidth product of the amplifier used. An impedance matched amplifier, supplied with the detector, has a gain of 10^6 and a gain bandwidth product of $60x10^9$ Hz. At low signal levels this amplifier was replaced with an ITHACO 1642 current sensitive preamp with selectable gain from 10^4 to 10^9.

5.4 Sensor testing chamber.

To measure the sensitivity of the various sensors designed and developed in the laboratory a sealed gas-tight chamber was required. The chamber had to be well sealed because of the dangers inherent in the use of flammable gases. The problem in the design of such a chamber is the optical fibre feedthrough method to be used. This should allow the fibre to be removed without damage for further modification of the sensor or storage. In figure 5.8(a) the most flexible solution is shown. Here the fibre is connectorised and may be very simply placed into or removed from the gas chamber and may be properly

sealed. This type of configuration did not prove practical for the following reasons. A range of fibres were to be tested, some of which had no protective coatings, were extremely delicate and therefore difficult to connectorise. The connectors had to be gas tight to stop leakage between the connector and the chamber wall and this was difficult to ensure. For monomode fibre, control of launch is critical and connectors would not provide the accuracy required. These problems are minimised if the unconnectorised fibre passes in and out of the chamber through small holes that can be sealed from inside and outside the chamber as shown in figure 5.8(b). The fibres can be taken directly to the launch and detector optics with this system thereby increasing the signal throughput as compared to the system in figure 5.8(a). The main problem with this method is the removal of the fibres from the chamber without damage. To attempt to overcome this problem an acetone soluble glue (Fiberhold, Ealing Electro Optics) was purchased. To correctly apply the glue the area of application had to be heated to the Fiberhold flow point (54°C) or above. The gas seal provided by the glue was not sufficient for our purposes but this may have been due to the difficulty involved in properly heating the application area without damaging the fibre. Although many sealing compounds were tried in order to seal the holes none were found to be satisfactory.

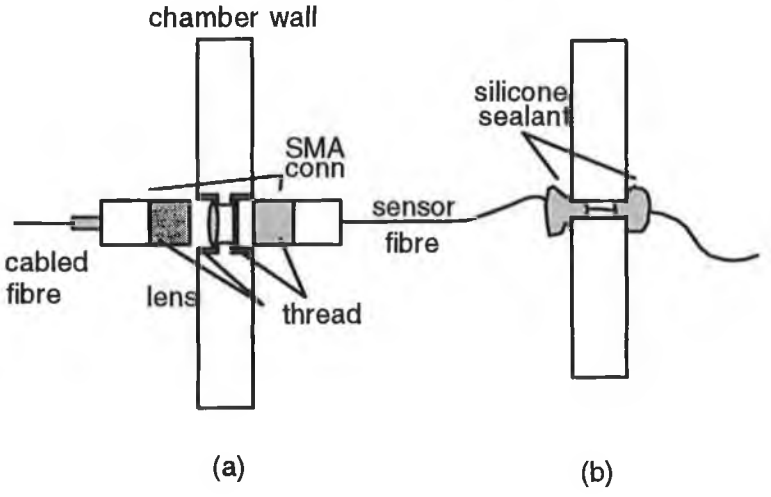

figure 5.8 gas tight fibre connections to gas chamber

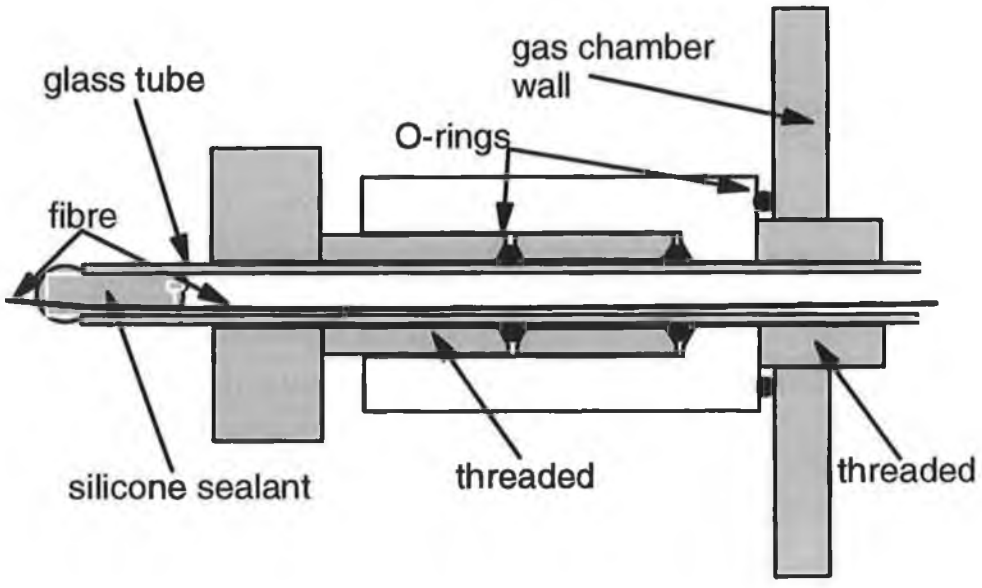

figure 5.9 cross section of Wilson seal with fibre in removable glass rod sealed with silicone rubber

The solution to the problem was provided by using a type of seal known as a Wilson seal, as shown in figure 5.9. Such seals are used in vacuum systems to allow probes to be inserted into vacuum chambers. Wilson seals allow glass tubes to pass through the chamber walls and be sealed in place. Therefore a fibre permanently sealed inside a short glass tube can be inserted and removed from the chamber any number of times with ease. The chamber designed using these seals is shown in figure 5.10. It has dimensions 360x150x120mm^3 and incorporates an extra Wilson seal larger than the fibre seals to allow the feedthrough of electrical signals so that measurements may be made inside the chamber while it remains sealed.

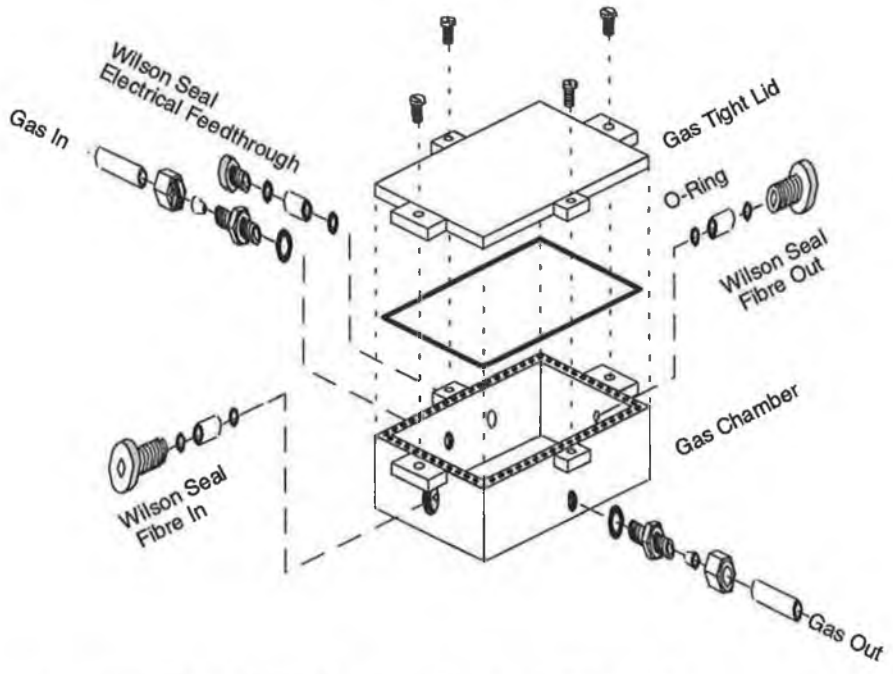

figure 5.10 exploded view of gas chamber employing Wilson seals.

5.5 Monochromator

The monochromator used (Optometrics Minichrom SCM-06) was a Fastie-Ebert in-line monochromator with a 300 lines/mm infrared grating blazed for peak efficiency at a wavelength of 3.5 μm. The f-number of the monochromator is 3.9. The range of entrance and exit slits available yielded resolutions of between 5 nm and 20 nm. Choice of slit usually depended on the intensity of the detected signal.

A long pass filter (Spectrogon, Sweden) with a cut-on wavelength of 1.8μm was used as a second order blocking filter. This filter was also used with the HeNe gas laser to remove the 1.152μm line from the beam.

5.6 FTIR Spectrometer

The FTIR Spectrometer used is a Bomem MB120 which has a maximum resolution of 1 cm^{-1}. The FTIR is supplied with a deuterated triglycine sulfate (DTGS) detector as standard. This was replaced with an InSb detector which has a better response over the wavelength range of interest for flammable gases i.e. 2-5 μm. The FTIR uses a high intensity temperature stabilised ceramic source housed in a nitrogen purged sealed chamber. The fibre launch stage is a custom designed 0.2 NA IRGN6 lens configuration attached to the side port option of the MB120 [7].

The FTIR has two advantages over dispersive spectrometers. The most important, the Jacquinot advantage, is the signal to noise advantage due to high energy throughput. As the FTIR is nondispersive, all of the optical power is incident on the detector during a spectral scan. The second advantage, the Felgett advantage, is the similtaneous processing of all wavelengths using fast fourier transforms which allows a large number of spectra to be recorded and averaged in a fixed time period [8].

5.7 Miscellaneous components.

5.7.1 Lenses

The majority of the lenses used were made from the infrared transmitting material IRGN6 (Spindler & Hoyer). Fused silica lenses were used where a suitable IRGN6 lens was not available. Fused silica has a transmission window at 3.4 μm of greater than 80%. The lenses were supplied with Melles Griot holders which were mounted on in-house custom designed supports.

5.7.2 Fibre positioners

An xyz micropositioner stage (Microblock, Photon Control, UK) was used to align the excitation end of the optical fibres. The xyz stage is fitted with differential positioners

on each axis to give relative positional accuracy of 0.1μm. Monomode fibre was held in place using magnetic clamps and a plate with a small v groove supplied with the positioner. The xyz micropositioner stage was also used with multimode fibre. A holder with the same optic axis as the v groove was designed to clamp to this stage to accommodate fibre chucks capable of holding a range of fibre sizes.

5.8 Conclusion

The lack of a single optical source capable of satisfying the requirements of all the fibre sensors being tested was a severe limitation. Broadband sources that could be used with multimode fibre were not of sufficient intensity for use with singlemode fibre. Conversely, the laser used with singlemode fibre, while providing significant power, does not give any spectral information. Therefore, its usefulness is limited. Furthermore, the stability of the transmitted laser power is very poor when used with singlemode fibre because of spatial fluctuations of the laser output that could not be compensated for. The PbSe detector, while less sensitive than the InSb detector, is more practical for sensing applications as it does not require regular replenishment of cryogenic coolant. The gas chamber employing Wilson seals proved to be the most flexible design that was also gas tight. This chamber was used with all experimental systems and with the FTIR spectrometer. It was possible to use the FTIR spectrometer with both multimode and singlemode fibre because of its advantages over dispersive spectrometers as mentioned in section 5.6. The FTIR spectrometer was not extensively used as most of the data had already been obtained before it became available.

In chapter 6 the individual experimental configurations used to obtain the data presented are detailed. All of the components used in these configurations have been descibed in this chapter.

1. Yakovlev Y.P., Baranov A. N., Imenkov A. N., Mikhailova M. P.: '**Optoelectronic LED - photodiode pairs for moisture and gas sensors in the spectral range 1.8 - 4.8 μm**', Proceedings SPIE, 1991, Chemical and Medical Sensors, Vol. 1510, pp. 170-9

2. Zotova N.V., Karandashov S.A., Matveev B.A., Pentsov A.V., Slobodchikov S.V., Smirnova N.N., Stus N.M., Talalakin G.N., Markov I.I.: '**Optoelectronic sensors based on narrow band A3B5 alloys**', SPIE Proceedings Chemical, Biochemical and Environmental Fiber Sensors III ,1991,Vol. 1587, pp. 334-345

3. Johnston S.F.: '**Gas monitors employing infrared LEDs**', Measurement Science & Technology, 1992, Vol. 3, pp. 191-5

4. Dobbelaere W., De Boeck J., Bruynseraede C., Mertens R., Borghs G.: '**InAsSb light emitting diodes and their applications to infra-red gas sensors**', Electronics Letters, 1993, Vol. 29, No. 10, pp. 890-1

5. Tai H., Tanaka H., Yoshino T.: '**Fiber-optic evanescent-wave methane-gas sensor using optical absorption for the 3.392 μm line of a He-Ne laser'**, Optics Letters, 1987, Vol. 12, No. 6, pp. 437-9

6. Culshaw B.: '**Optical fibre sensing and signal processing**', Peter Peregrinus Ltd., 1984, Chapter 11

7. Bomem, '**Michelson series, FT-IR user's guide**', Bomem Inc., 1989

8. Griffiths P.R., de Haseth J.A.: '**Fourier Transform Infrared Spectrometry**', Wiley & Sons, 1986, Chapter 7 (IV)

Chapter 6 Experimental Results

6.1 Introduction

The experimental results obtained from the investigation of evanescent wave absorption using the fibre sensors described in chapter 4 are presented in this chapter. The primary use of the data is to identify fibre structures that may provide the basis for a viable evanescent wave gas sensor. A minimum requirement for a viable flammable gas sensor is the ability to detect a concentration of 50% of the lower explosion limit (LEL) of the gas for which it is designed. For example, the sensor must be at least able to detect 2.5% methane in air as 5% is the LEL for methane [1]. For some commercial applications better performance is required e.g. offshore installations require a detection limit of better than 1% of the LEL [2]. The data are also compared with the predictions of the theoretical models detailed in chapters 2 and 3. Comparison of experimental and theoretical absorption is used to evaluate the accuracy and applicability of various models. Using this information it is possible to design custom optical fibre structures which enhance the evanescent wave interaction. The insights obtained from the combined consideration of experimental and theoretical data are important in identifying the direction of future research into optical fibre sensors based on evanescent wave interactions.

Experimental results are presented for all of the sensors fabricated during the course of this work. In addition, data obtained using commercially available Teflon clad fluoride fibre are presented [3]. The identification of suitable IR sources played an important role in the experimental realisation of the results presented. Therefore a separate section is given to the characterisation of a novel mid-IR solid state LED first used in this work as a source for optical fibre evanescent wave gas sensing [4] .

A number of gases and liquids were used for measuring the absorption of various sensor configurations. Although methane gas was of particular interest, it was not extensively used because of the high spectral resolution required in order to match its very fine rotational structure. Instead, a commercially available mixture of the flammable gases propane and butane was often used. In contrast to methane, the absorption spectra of propane and butane in the 3-4 μm region form a continous band and can more easily be observed with a low spectral resolution detection system. High resolution spectra of the gases used are given in Appendix E as well as a high performance liquid chromatography (HPLC) trace (figure E.4), indicating the composition of the propane / butane gas mixture. In calculations involving the gas mixture, the absorption coefficient of propane is used because at low resolution the absorption spectra of the two gases are almost identical. An organic solvent, isopropanol (IPA), which absorbs light strongly in the region of interest was used to determine the sensitivity of sensor structures with small evanescent penetration. IPA was also used when it was impractical to place the sensor in a gas tight chamber for analysis. The refractive index values of IPA at the 3.392 μm line of the HeNe laser are $n_r = 1.38$ and $n_i = 0.01$, equivalent to an absorption coefficient (α) of $3.7 \times 10^4 m^{-1}$.

6.2 Polished sensors.

6.2.1 Introduction

Single mode fibre was investigated as an evanescent wave sensor primarily because it has the highest r value of all fibre types. The r value is the ratio of the optical power contained in the fibre cladding to the total optical power guided by the fibre.

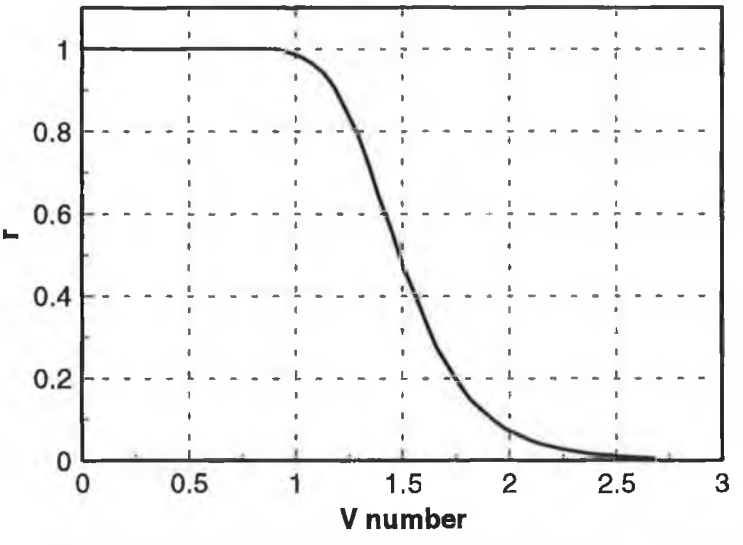

figure 6.1 cladding power ratio r for HE_{11} mode as a function of V number

The value of r increases with decreasing V number (the normalised frequency parameter) of a fibre. For highly multimoded fibre, r may be calculated from Gloge's approximation $r = \frac{4\sqrt{2}}{3V}$ and is typically of the order of 0.05 or less [5]. For single mode operation, the fibre V number must be less than 2.405 and for practical single mode fibre where $1 < V < 2.405$, the value of r can be large as shown in figure 6.1. The V number of the Le Verre Fluore zirconium fluoride fibre used in this work is between 1.2 and 1.5 at the 3.392 μm line of the HeNe laser (the range is due to numerical aperture variation between batches). From figure 6.1 the value of r is approximately 0.5 at V = 1.5 and therefore 50% of the guided power propagates in the cladding. On initial examination this suggests a high sensitivity for single mode fibre evanescent wave sensors fabricated by cladding removal.

Polishing was chosen as the initial method of evanescent field access for single mode fibre as the finished product is more robust than that produced by tapering. The similarity between the structure of a side-polished sensor and the structure of D-shaped fibre, not currently available in fluoride, means that the theory for the two is similar. One of the models used to predict the sensitivity of the polished fibres was in fact developed for D-shaped fibre. The sensitivity of D-shaped fibre is easier to predict than that for polished blocks because it is a constant structure. The merits of the models used are discussed in detail in the experimental discussion below.

Despite the apparent advantages associated with using single mode fibre the main problem in developing a single mode evanescent wave sensor lies in the identification of a suitable mid IR source. There are no broadband sources from which light can be launched efficiently into single mode fibre and solid state sources for the mid IR that are fibre compatible, such as laser diodes, are not yet routinely available. To measure the sensitivity of single mode fibre a HeNe laser was used as described in section 5.2.1. Absorption spectra were also taken with an FTIR spectrometer modified for use with single mode fibre. The FTIR spectrometer uses a large area broadband source and is not designed for use with monomode fibre. Spectra obtained must be averaged many times to improve the signal to noise ratio to an acceptable level for measurements.

6.2.2 Experimental apparatus.

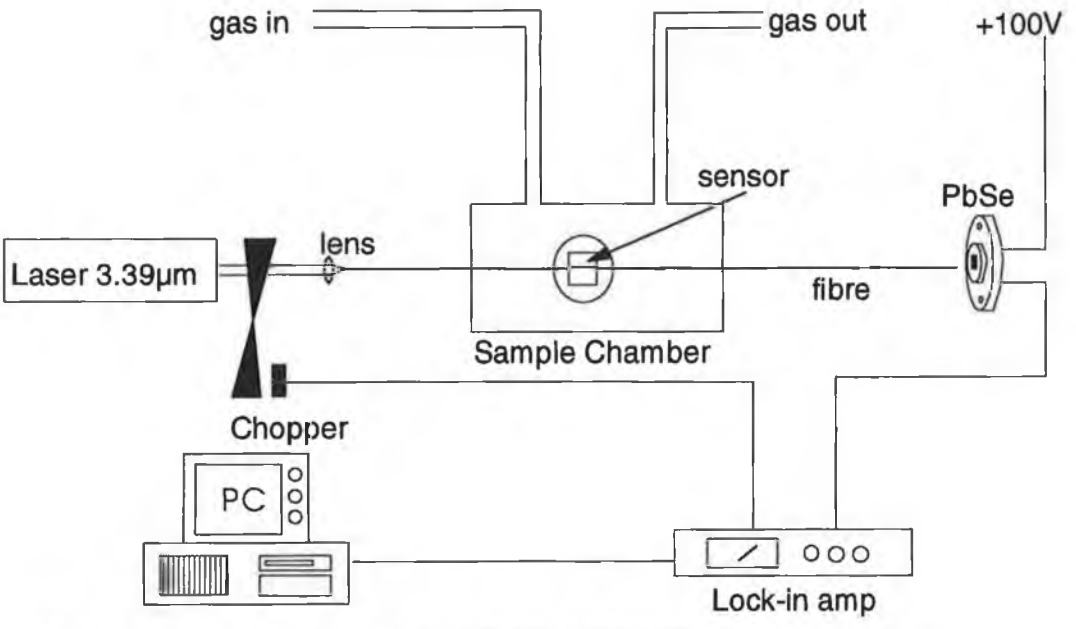

figure 6.2 Infrared laser based single mode fluoride fibre experimental apparatus

The experimental system used to measure the sensitivity of single mode side-polished blocks is shown in figure 6.2. The HeNe gas laser is modulated at 220Hz by a Bentham optical chopper for detection with a lock-in amplifier. The laser is launched into the fibre using a 6 mm focal length fused silica lens (cf. section 5.7.1). The detection system consists of a photoconductive PbSe detector and a Stanford Research SR510 lock in amplifier. A short wavelength blocking optical filter was used to prevent the launch of the 1.152 μm laser line into the fibre. For measurements involving gases, the sensing element was housed in a custom-designed gas chamber described in section 5.4. An FTIR spectrometer was used to obtain IPA absorption spectra. The FTIR spectrometer used is a Bomem model MB120 as described in section 5.6.

6.2.3 Experimental measurement.

The sensitivity of the side-polished fibre to an absorbing species was measured as a function of the remaining cladding layer thickness. The error in the calculated layer thickness, using the technique described in section 4.2, due to the potential variability in

fibre parameters including fibre concentricity is difficult to quantify. The fluoride fibre manufacturer quotes a concentricity error of 5 μm. Therefore, this is taken as the minimum absolute error in all calculated overlayer thickness values. However, overlayer thickness calculations are accurate for relative overlayer measurements. Evanescent wave absorption was quantified using IPA which strongly absorbs at the 3.392 μm line of the HeNe laser source. The measurements were performed for a range of polished blocks with differing radii of curvature (10, 15, & 25 cm). The evanescent wave absorption data are used to evaluate polishing as a technique for single mode fibre sensor fabrication. All the initial development work was performed using blocks with a 25 cm radius of curvature, which is the standard used in the fabrication of polished couplers [6,7,8]. Larger radii would provide longer interaction lengths but such blocks are difficult to fabricate using the technique outlined in section 4.2.

Figure 6.3 shows the results obtained from a single mode fibre mounted on a block with a radius of curvature of 25 cm. The measurements terminate at an estimated remaining cladding layer of less than 1 μm. These data exhibit a behaviour that mirrors the exponential nature of the field in the cladding of a planar or fibre waveguide and this is what is intuitively expected from such a device.

The planar waveguide model was initially used to estimate the sensitivity of the side-polished sensor to absorbing overlayers such as IPA or methane. The planar waveguide structure used to simulate the side-polished block is shown in figure 6.4. In this case a 4 layer waveguide was used as extending the model to 5 or more layers does not improve the accuracy of the calculated IPA absorption. The overlayer thickness is set equal to the minimum core to analyte distance d shown in figure 6.4. The layer representing the core is set equal to the core diameter. The cladding and analyte are assumed to be infinite in extent and assume the roles of substrate and superstrate respectively.

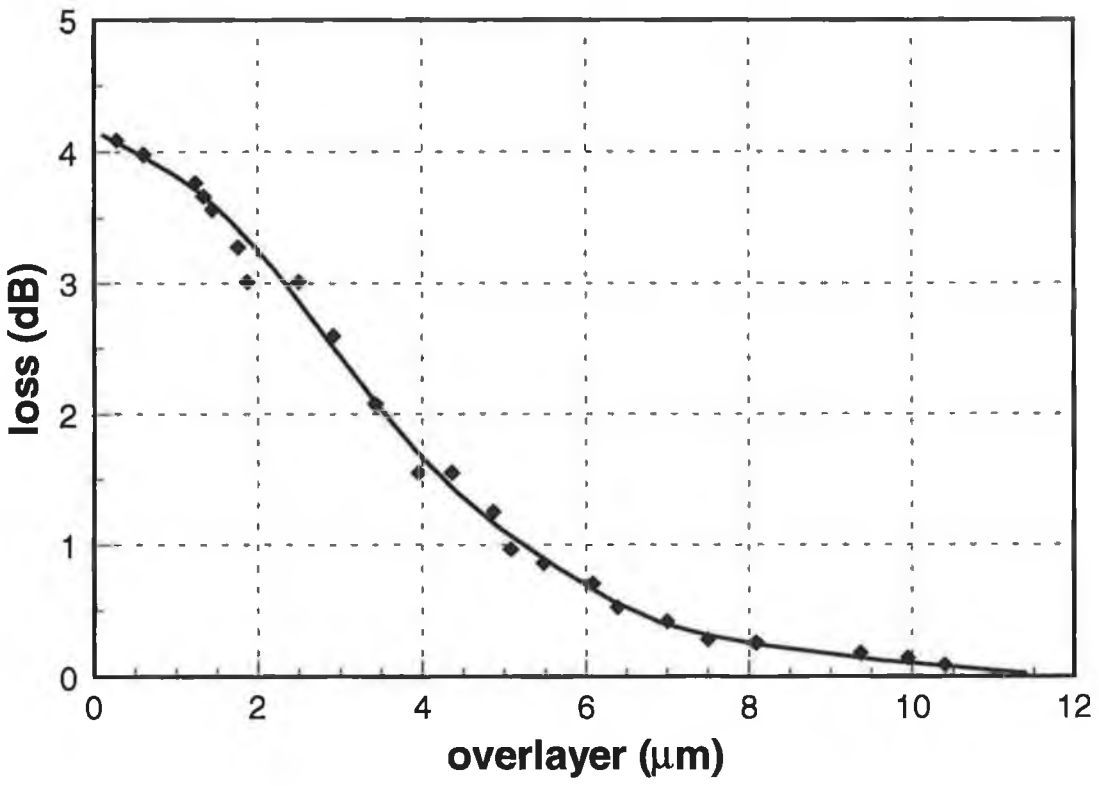

figure 6.3 IPA attenuation vs polish depth for 25cm radius of curvature polished block

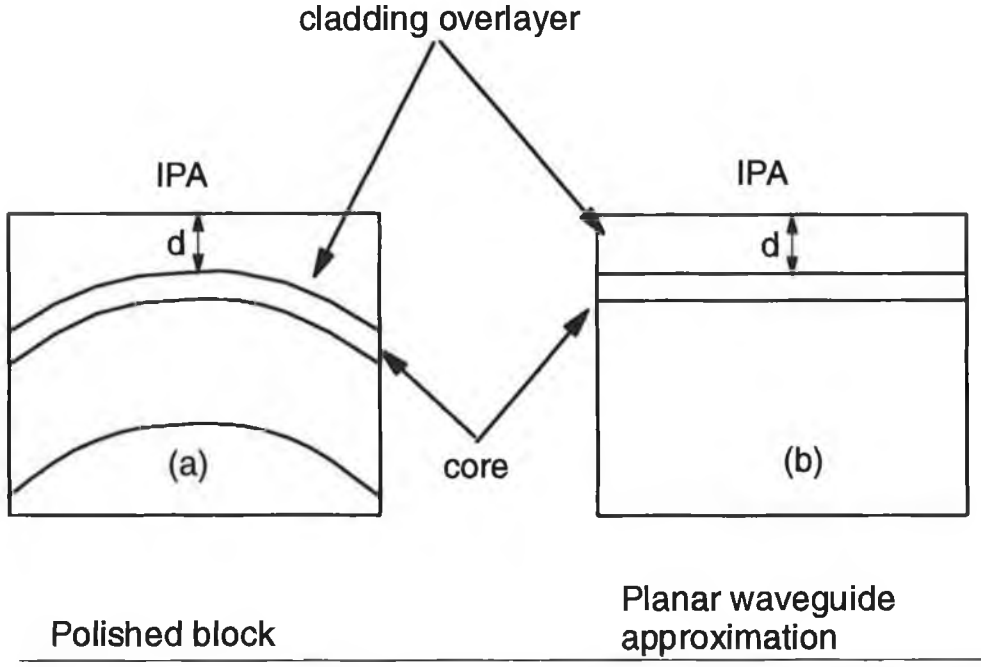

figure 6.4 (a) cross section through polished block, (b) planar approximation

Figure 6.5 shows the evanescent wave absorbance as a function of cladding overlayer thickness predicted by the model for IPA @ 3.392 μm compared with the experimental data for IPA. Data for the TE_o and TM_o modes of the waveguide are presented using the following fibre parameters (cf. Appendix C): core diameter = 11μm, n_{core} = 1.495, and n_{clad} = 1.49 which correspond to a fibre NA of 0.12. These parameters are used in all side-polished fibre models. The interaction length is set to be 1 cm. This length is used because an ellipse length of between 10 and 10.7 mm corresponds to an overlayer thickness of between 8 and 0 μm for a 25 cm radius block. In view of the number of approximations used the agreement between experiment and theory is reasonable.

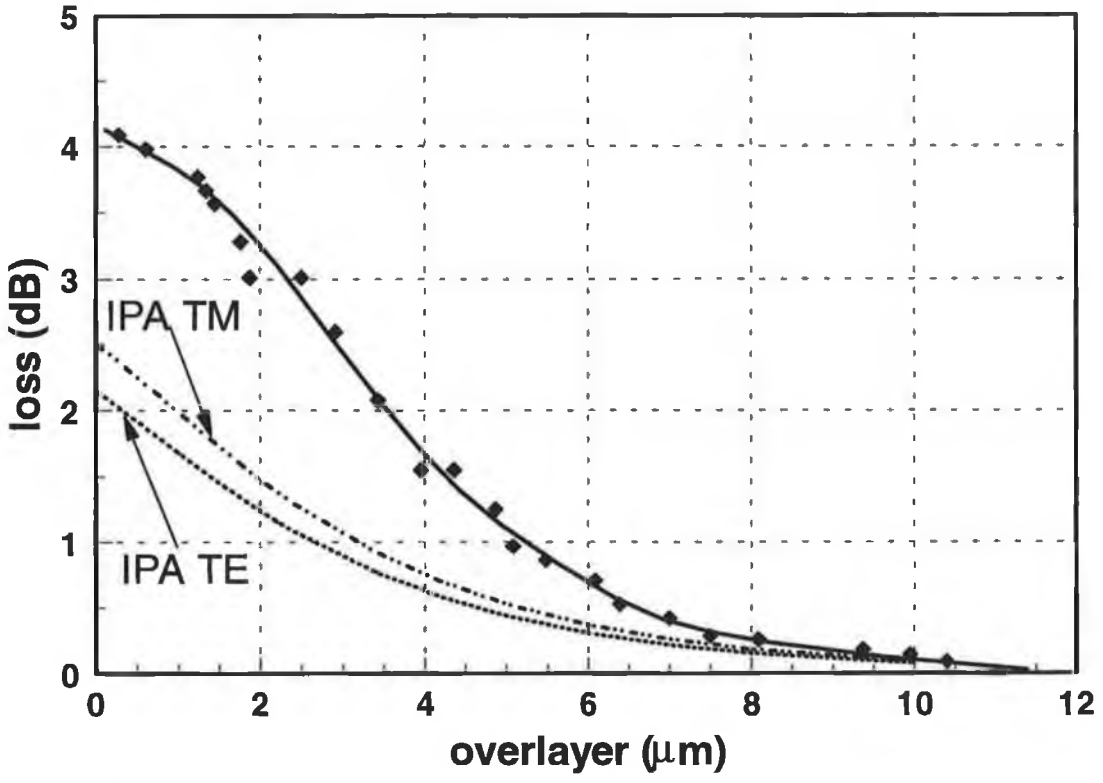

figure 6.5 comparison of IPA absorption experimental data with results of 4 layer planar waveguide model

When the measured IPA absorbance response for a particular side-polished sensor was 3dB or greater a parallel experiment was set up to measure the sensor response to methane. The sensor was sealed into a gas tight chamber and methane was pumped into the chamber. Invariably, the fibre throughput was not measurably attenuated by the gas. The absorption coefficient of methane at 3.392 μm is 8.3 atm^{-1} cm^{-1} ($n_i = 2.2 \times 10^{-4}$) [9].

This is approximately 2% of the absorption coefficient of IPA 370 cm^{-1} (n_i = 0.01) [10] at the same wavelength. Therefore a maximum loss of 0.01 dB would be expected from the ratio of absorption coefficients. However, predicting the methane sensitivity from the IPA data by ratioing their respective absorption coefficients is not valid because the evanescent field penetration is a function of the real part of the analyte refractive index [11,12]. Using the 4 layer planar waveguide model the calculated ratio of loss by IPA (2.5 dB/cm for TM mode) to loss by methane (0.0059 dB/cm for TM mode) for a 0 μm overlayer thickness is 423 [13]. This is nearly 10 times greater than that predicted by the ratio of their absorbtion coefficients and well below the noise level of the experimental system used. This discrepancy results from the effect of the real part of the refractive index on the guidance properties of the waveguide [14,15]. This effect is shown explicitly in figure 6.6 where a plot of the evanescent wave loss of the TE mode of a waveguide is plotted as a function of the real part of the refractive index of an absorbing overlayer. In this plot the overlayer and absorption coefficient are kept constant at 1 μm and 370 atm^{-1} cm^{-1} (n_i = 0.01), respectively. The trend in this graph is important as it shows that the larger the refractive index mismatch between sensor and analyte the less sensitive is the device. Physically what this means is that the evanescent wave penetration into the analyte is reduced and the modal power is confined within the waveguide. Using this result (for 1 cm interaction length) it is possible to predict the side-polished interaction length required to produce a 10% signal loss @ λ=3.392 μm when exposed to the LEL of methane. To obtain this figure the measured IPA loss is divided by the theoretical ratio of absorption loss to give a loss due to 100% methane of $6x10^{-3}$ dB cm^{-1}. The predicted required interaction length is then found to be approximately 15 m.

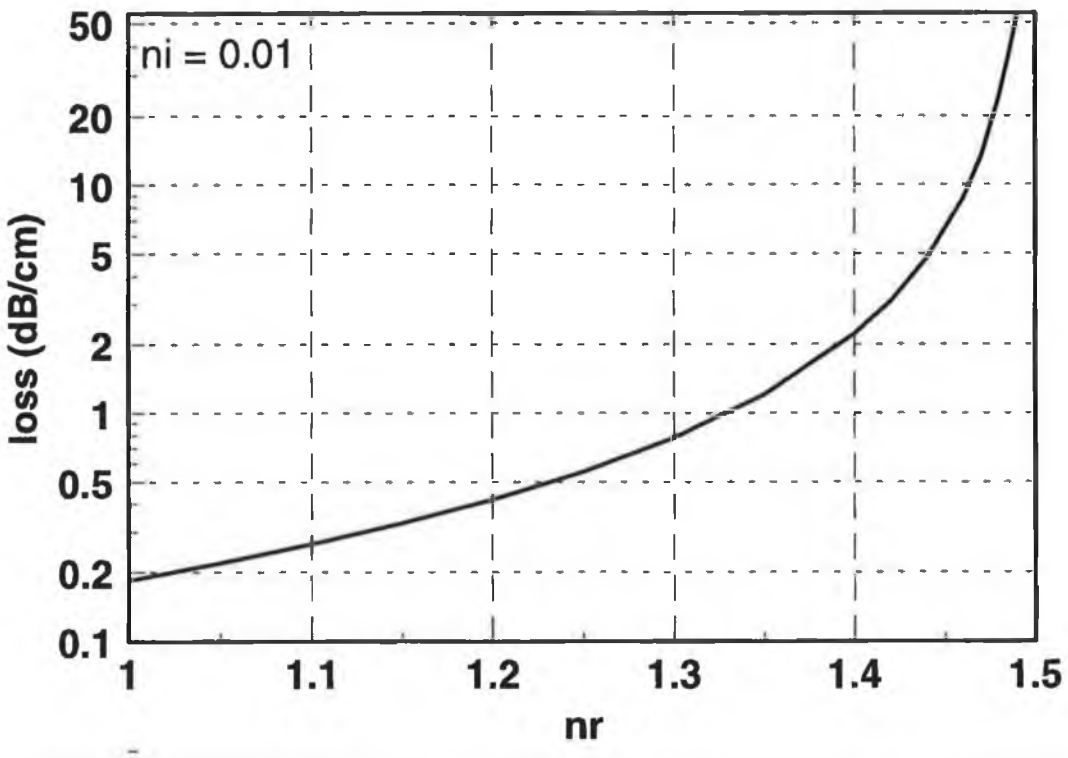

figure 6.6 planar waveguide loss as a function of the real part of the refractive index of an absorbing medium for a TE mode ($n_i = 0.01$).

The sensor exhibits a greater sensitivity to IPA than predicted by the planar waveguide model even though this model significantly overestimates the interaction length of the sensor. It is possible that the radius of curvature may contribute to this greater sensitivity. It is a well known phenomenon [16,17] that the power in a bent fibre is shifted to the outer edge of the curve. This effect is normally small at the radii of the polished sensors i.e. where R >> a (the core radius). To investigate this further mounting blocks were machined with radii of 10 and 15 cm and side-polished sensors were fabricated using these blocks.

Figure 6.7 shows the evanescent wave absorption data obtained from an IPA layer on a polished block with a radius of curvature of 15 cm. The peak absorption is quantitatively similar to that recorded for the 25 cm block. However, the behaviour of the absorption as a function of overlayer thickness is not as expected and exhibits significant oscillations. As mentioned earlier, the overlayer thickness on the x axis is not an

absolute measurement of the remaining cladding layer and it is possible that the oscillations are a result of polishing into the fibre core. A HeNe laser @ 632.8nm was used to check the integrity of the polished fibre and no significant leakage was observed from the polished region. Because polishing into the core would represent an abrupt perturbation it would be expected to lead to significant light leakage, and so none was observed it was deduced that no polishing had penetrated the core.

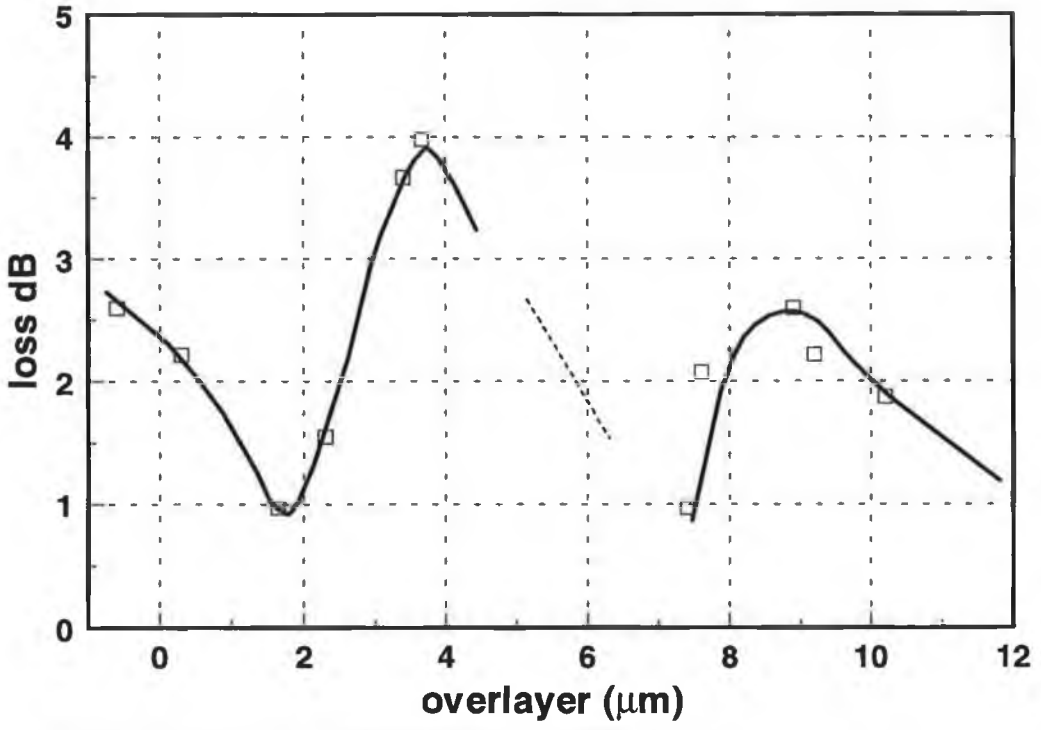

figure 6.7 attenuation vs polish depth for 15cm radius of curvature polished block

Figure 6.8 shows what is predicted by the planar waveguide model if we extend the analysis to describe polishing into the core. A 5 layer model (an air substrate is added to the structure) is used here as the mode is not guided by the 4 layer structure once the core is smaller than 6 μm. Both TE and TM modes are shown as well as their effective refractive indices This model does predict a decrease in absorption but does not predict oscillation or recovery of the absorption as seen in figure 6.7.

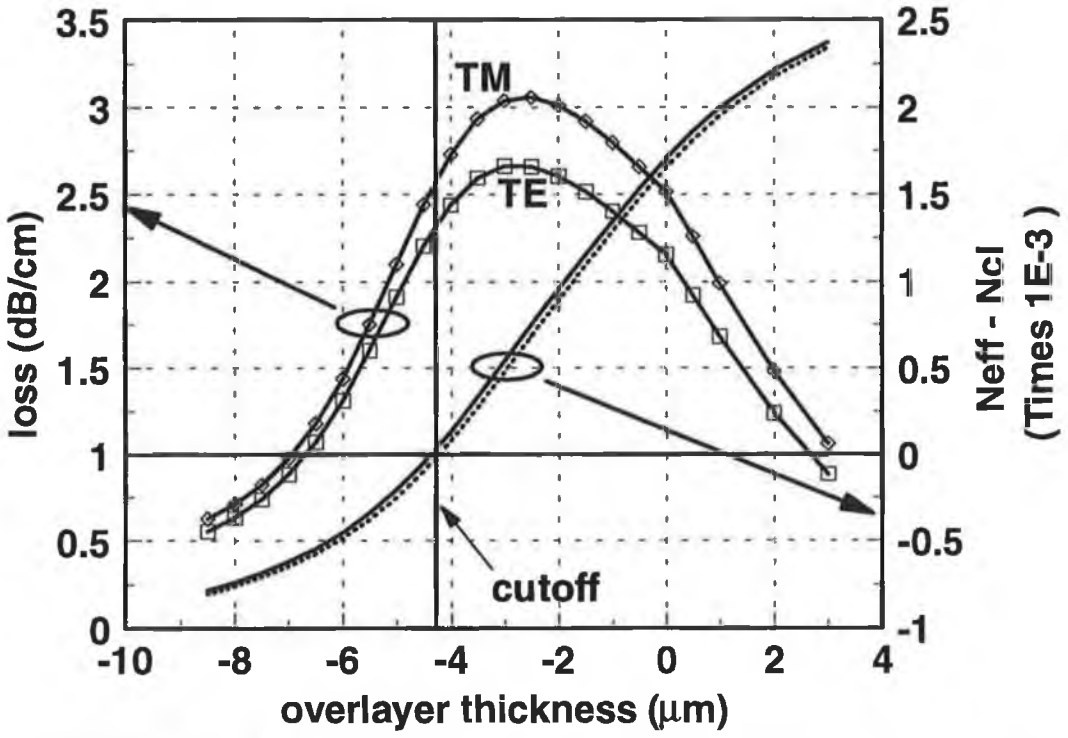

figure 6.8 IPA loss as a function of polish depth. (negative overlayer thickness represents polishing into the fibre core)

The experiment was repeated with a side-polished fibre block with a 10 cm radius of curvature. The evanescent wave absorption data in figure 6.9 exhibit the same overall shape as the previous set of data. However, the overlayer thickness at which the measured IPA loss starts to decrease is significantly different to that recorded with the 15 cm radius block. If the two sets of data are overlaid as shown in figure 6.10 with the oscillation peaks aligned they exhibit reasonable agreement in both period and magnitude. This tends to indicate that concentricity errors in the fibre are the cause of the different overlayer thicknesses calculated for the peak absorptions. In figure 6.9 it is not possible for the first oscillation to occur at the onset of polishing into the core, because after a further 10 μm of polishing the core was inferred to be intact from visible observation of the fibre throughput using a 632.8 nm HeNe laser. The small differences in period are probably due to the different radii of curvature.

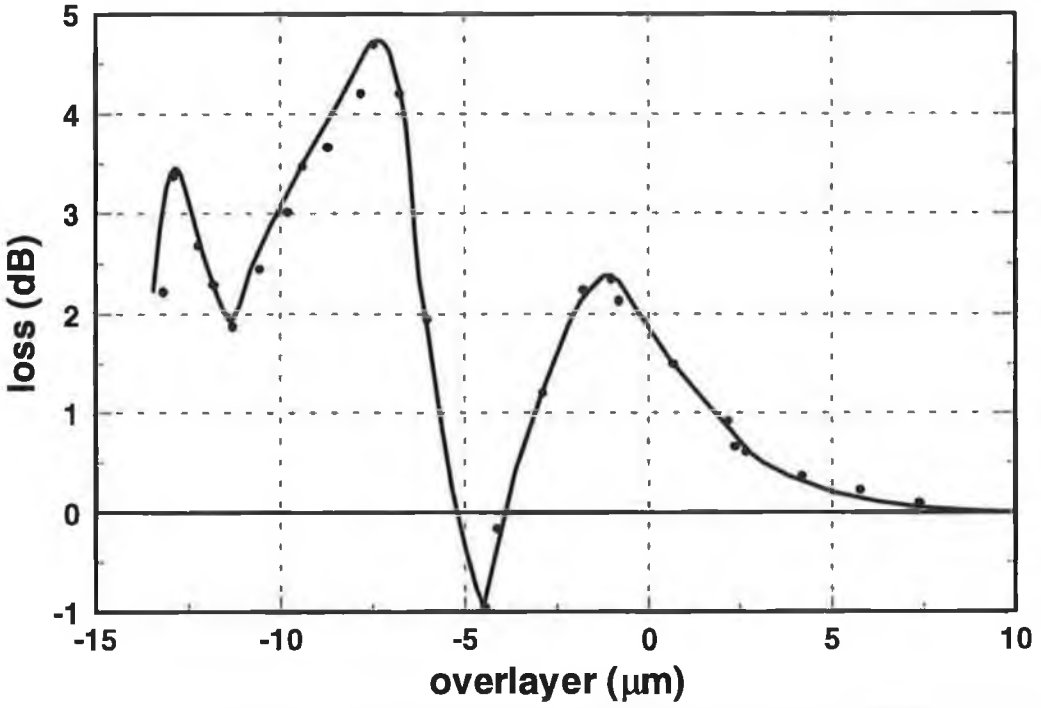

figure 6.9 IPA loss vs polish depth for 10cm radius of curvature polished block (note: core diameter is 11μm)

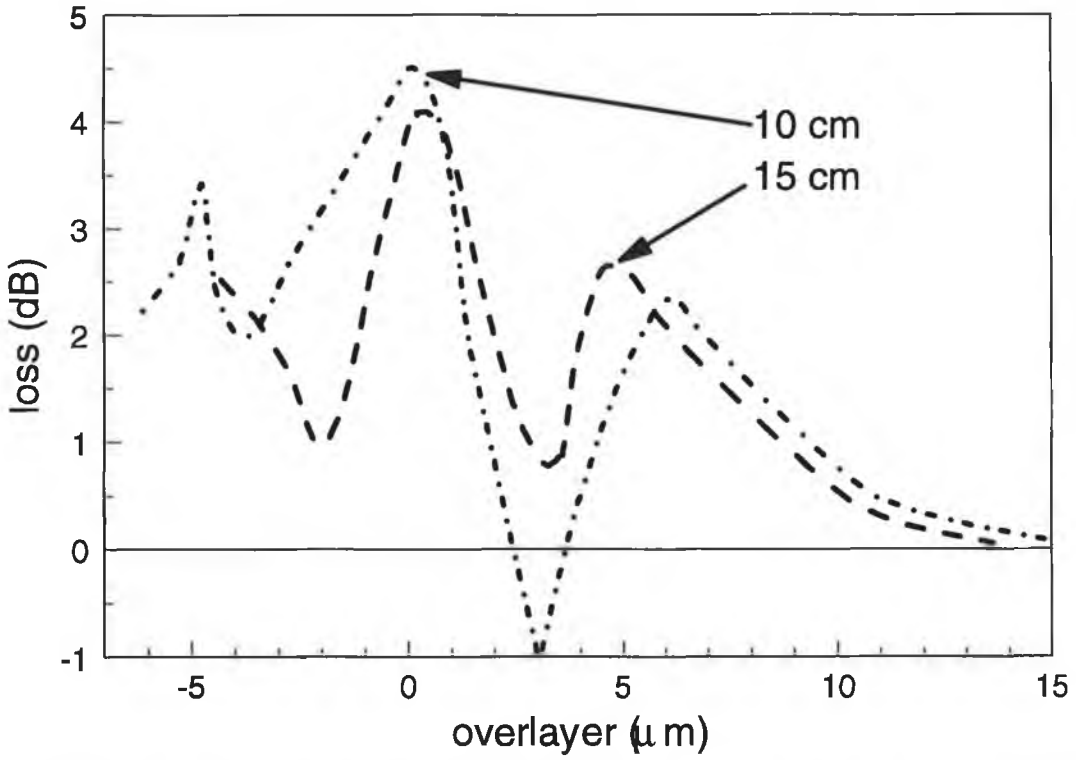

figure 6.10 IPA loss data for 10 and 15 cm radius side-polished fibres shifted on the x axis to align the oscillations in the loss data.

In figure 6.9 the change in throughput due to the addition of IPA becomes a gain of 1 dB when an estimated 4 μm depth of core has been polished. This signal gain agrees with the observations of Digonnet *et al.* [6]. In their work the gain is attributed to a liquid overlayer restoring the HE_{11} mode in the polished section of the fibre relative to the loss caused by the significant modal perturbation with an air overlayer. Records of throughput measurements for this fibre show that coincident with the relative gain due to IPA there is a significant decrease in the throughput of the side-polished fibre in air. The power throughput began to decrease coincident with the onset of the first oscillation in the measured IPA absorption. The throughput reached a minimum (down a factor ~ 30) at the trough in this oscillation. These measurements support Digonnet's observations. However, after further polishing the throughput increases and returns to the original value. The return of the signal to its original level suggests that the fibre core is not significantly polished into at this point as would be suggested by Digonnet's results. Regular checks were made of core integrity using a 632.8 nm HeNe and the core was observed to be intact during these measurements.

The planar structure is not a very accurate model of the polished fiber evanescent wave sensor structure. This is a result of the planar model being bound in only one direction. This may account for its inability to predict the oscillation observed. To obtain a better model of the structure the D-shaped theory of Vassalo [18] was investigated. Vassalo's theory has been presented in section 3.4. The core and cladding parameters used are identical to those used in the planar model. The curvature is ignored because it would make the model overly complicated. Figure 6.11 shows the predictions of Vassalo's model for both the effective index of the guided mode and the power in the analyte expressed as a fraction of the total power. The most significant feature of these data is that the mode is cutoff both for air and IPA external media before the core has been polished into. In contrast, the planar model predicts that it is necessary to polish into the core before the mode can no longer be supported. Digonnet *et al.* [5] observed an increased throughput when a liquid drop is placed on a polished fibre. Digonnet states '*The effect of a liquid ... is to reduce the perturbation*'. The perturbation causes attenuation which may be significant if the mode is perturbed to such an extent that it is

no longer guided. From figure 6.11 it can be seen that the loss as a function of overlayer thickness will be reduced before either the core is polished into or the mode is no longer guided. In addition there is a small range of overlayer thicknesses for which the presence of IPA would restore the mode to the guidance condition. These effects together may explain the drop in IPA loss and the gain observed at small overlayer thicknesses. However, this theory cannot explain why the power throughput recovers and also cannot explain why a second oscilation occurs. No other model has been found in the published literature that can explain the behaviour observed for loss as a function of polish depth. In addition no other reports of this effect have been found to date.

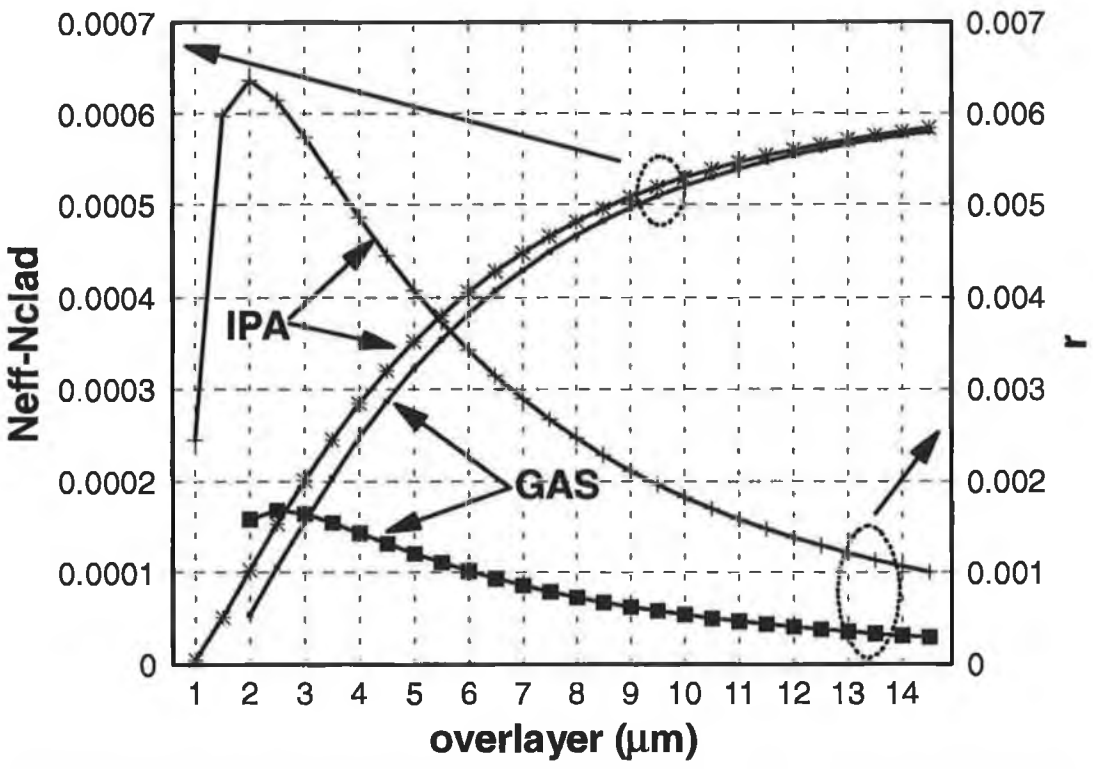

figure 6.11 effective index and r value as a function of overlayer thickness from D-shaped theory (losses may be calculated using the perturbation technique described in chapter 3)

All of the data presented so far for the side-polished fibres indicate that the structure is not sensitive enough for gas detection. Methods are therefore required to enhance the sensitivity of this structure. One such method is to use D-shaped fluoride fibre which provides increased interaction length and a consequent increase in overall sensitivity. D-shaped fluoride optical fibre is not currently available, however, but work is being performed to develop silica D-fibre for distributed flammable gas sensing [19]. The

sensitivity of D-shaped fibre remains small for gases because of the modal confinement caused by the large refractive index discontinuity, the effect of which was shown earlier in figure 6.6. Muhammad *et al.* [20] proposed the use of high index overlayers to improve sensitivity and theoretically predict enhancements of an order of magnitude using such techniques with D-shaped fibre. The high index overlayer offsets to some extent the effect of the refractive index of external medium on the guidance properties of the fibre. The overlayer does not overcome, however, the problem of surface fouling which may prevent the use of evanescent wave sensors outside of the laboratory [21]. The solution may lie in the use of porous overlayers of refractive index similar to the cladding refractive index. Such layers would allow the analyte gas to permeate the evanescent sensing region but would prevent fouling of the sensor by larger molecules. A gas permeable Teflon cladding has been used by us to successfully demonstrate gas sensing with a multimode evanescent wave sensor [22]. However, Teflon has a high attenuation in the mid IR and is therefore only of limited interest. More significant is the possible use of microporous fluoride sol-gel glass to enhance gas sensitivity and at the same time protect the D-fibre surface from contamination by larger molecules. A theoretical evaluation, using the planar waveguide model, of the sensitivity enhancement, relative to an uncoated fibre, possible for methane with TiO_2 porous sol-gel glass overlayers is shown in figure 6.12. The refractive index of the overlayer is calculated assuming that the refractive index of the microporous structure may be obtained from the gel pore volume refractive index (equal to the analyte index) and the densified glass index ratioed by volume. Therefore

$$n_{gel} = Xn_{gas} + (1 - X)n_{glass} \qquad 6.1$$

where X is the fractional porosity of the gel.

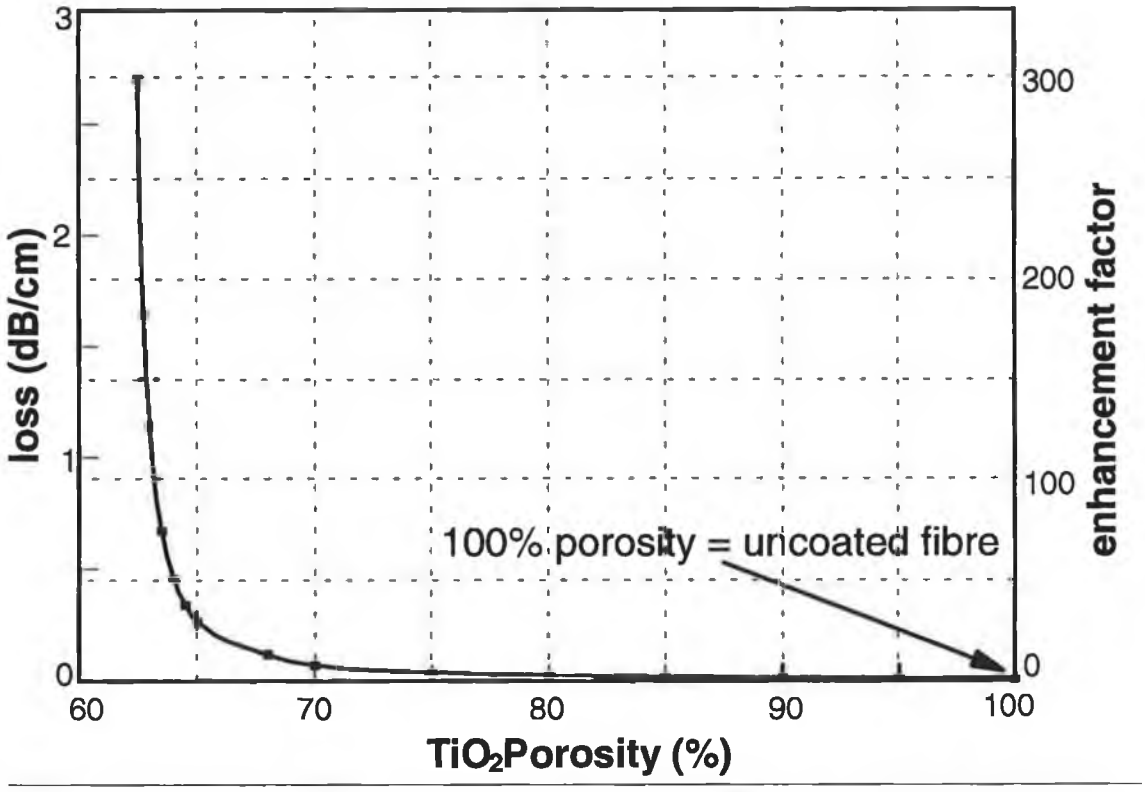

figure 6.12 Sensitivity enhancement for 100% methane @ 3.392 μm as a function of sol-gel porosity for a TiO_2 gel.

The refractive index of densified TiO_2 is 2.3. Therefore overlayer porosities below approximately 60%, where the compound layer index is greater than the guided mode effective index, result in a lossy structure. For porosities just above this value, however, the TiO_2 layer gives a very large enhancement because of its high porosity at a refractive index close to the cladding refractive index. Making a gel of exactly the required porosity is a difficult process. The refractive index may be more easily controlled by mixing silica and TiO_2 in controlled ratios where the resultant porosity of the gel is approximately known. Silica gels do not give the same degree of enhancement as TiO_2 because of the lower refractive index of the densified glass. Consequently the porosity required to achieve a refractive index close to the fluoride fibre cladding index is very small. This, in turn, results in a very low access volume for the sensor gas with a consequent low gas absorption enhancement value as may be seen from figure 6.13. TiO_2 and SiO_2 sol-gels have high attenuation in the infrared and although they may be coated on side-polished fibres without significantly degrading the throughput they would not be practical as coatings on fluoride D-fibre. The solution to the problem of

throughput would be the use of gels made from fluoride glasses. The enhancements predicted by the planar waveguide model for methane sensing at $\lambda = 3.392$ μm, using fluoride and silica gels is shown in figure 6.13. The difference in absorption predicted for silica and fluoride at low sol-gel porosities shows the influence of refractive index on evanescent wave sensitivity.

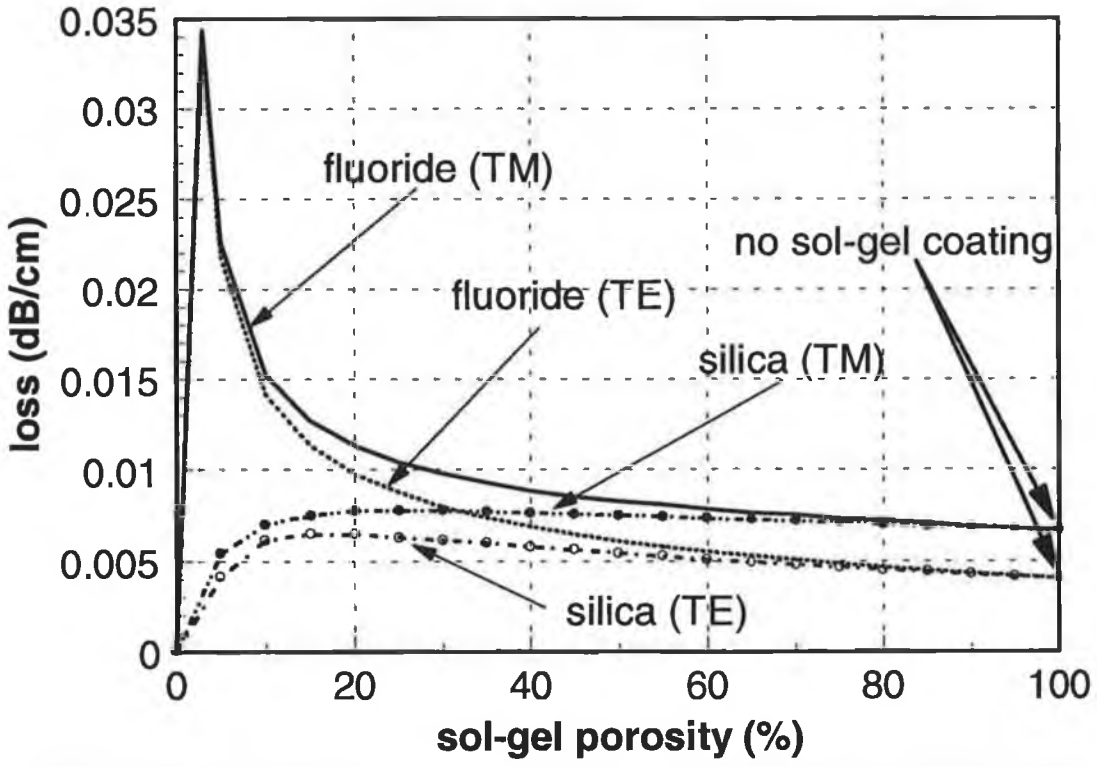

figure 6.13 silica and fluoride sol-gel methane gas absorption enhancement for a cladding layer of 1μm

6.2.4 Conclusion

From the absorption data recorded for IPA and the predictions of the planar and D-shaped fibre models it has been shown that side-polished and D-shaped fibre does not have sufficient sensitivity for viable gas sensing. Therefore, a method of achieving an enhancement of the evanescent wave sensitivity of these structures is required. The use of higher index overlayers [19] or porous overlayers as discussed here offers some improvements. Sol-gels, and in particular, TiO_2 sol-gels promise significant sensitivity enhancements but at the cost of high waveguide losses. Higher losses would not be a problem if fluoride glass microporous gels were used. Although fluoride gels are not yet readily available their synthesis is being vigorously investigated [23].

The mounted side-polished fibre is a robust structure when fully connectorised and is sufficiently sensitive to liquid absorptions for it to be used in this context. It would provide a powerful tool for performing real time analysis of liquid or solid materials e.g. monitoring the curing of epoxies or the water content of a material as it is baked or dried. Figure 6.14 shows a spectrum of IPA recorded with an FTIR spectrometer using a polished block of 25 cm radius and demonstrates the spectroscopic potential of the polished fluoride structure for absorbing liquids.

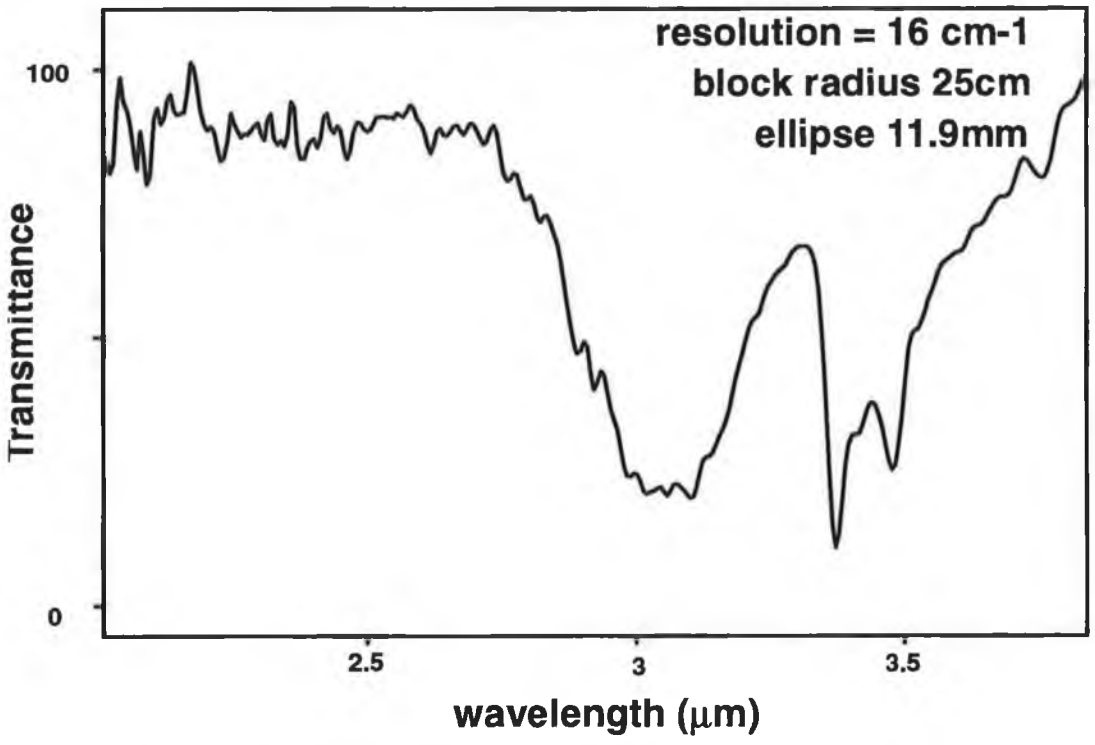

figure 6.14 IPA spectrum recorded on a 25 cm polished block using BOMEM FTIR

6.3 Single mode fibre tapering.

6.3.1 Introduction.

Section 4.4 details the methods developed in this work for tapering zirconium fluoride optical fibre. In this section the sensitivity of such tapers are analysed. The local modes of the fibre as a function of diameter reduction is analysed to determine the adiabaticity criterion for the 11/125 μm single mode fibre used (cf. section 4.3). To satisfy this criterion (also known as the slowly varying condition) '*the fiber nonuniformity must change over a distance large compared with* z_b' [24] where z_b is the beatlength between

the HE_{11} guided mode of the fibre and the cladding mode to which it most effectively couples. The fiber nonuniformity is quantified later in this chapter and taper measurements are analysed for compliance with the criterion. The simple constant volume taper model described in section 4.3 is used to predict the tapering parameters required to satisfy the adiabatic criterion. The final section of the theoretical discussion is a prediction of the parameters required to produce a 10% drop in throughput at 3.392 μm when a taper is exposed to 5% methane in air . This discussion is limited to single mode fibres and single mode tapers. Multimode zirconium fluoride fibres have been reported elsewhere for use as couplers [25] and as evanescent wave sensors [26].

A set of results for gas sensing using a monomode fluoride fibre taper is presented. The taper was fabricated for this work by the fluoride fibre manufacturer Le Verre Fluore (Rennes, France) using their 11/125 μm single mode fibre, which is the same fibre as used in our tapering system. This result and the results of Tai et al. [27] are used to test the validity of the fibre theory and the planar waveguide approximations (cf. section 6.3.4).

6.3.2 Experimental apparatus.

The apparatus used in this section is described earlier in section 6.2.2 and illustrated in figure 6.2. The sensitivity of the single mode taper pulled by Le Verre Fluore was measured using a Bomem MB120 FTIR spectrometer .

6.3.3 Experimental results

The maximum reduction ratio ($D_{final}/D_{initial}$) achieved with tapers fabricated as described in section 4.3 was approximately 0.2 (a taper waist diameter of 25-30 μm). These tapers were fabricated using the horizontal tapering rig. However, the measured throughput of these tapers was small and the signal to noise ratio using the laser based experimental system was of the order of 10. The smallest taper fabricated with a significant power

throughput had a taper waist diameter of 46 μm. The longitudinal profile of this taper is shown in figure 4.10. This taper will be referred to in the remainder of this section as T46.

None of the tapers pulled for this investigation showed any measurable sensitivity to the flammable gases methane, propane and butane. Using the no-core approximation [28], i.e. assuming that the tapered region is a cladding / air waveguide, the sensitivity of taper T46 may be calculated. Using $n_{core} = 1.493$ (cf. Appendix C) and $n_{clad} = 1$, the V number at the HeNe laser wavelength 3.392 μm is 47. Assumes all allowed modes of the taper are excited equally one may estimate a ratio of power in the cladding (r) to total power of 0.04 [5]. For a more correct analysis only the the fundamental, or HE_{11}, mode of the fibre may be used to predict the r value as only this mode is transmitted through the taper to the detector in the case of adiabatic tapers. The r value for this mode in a taper with a V number of 47 is less than 10^{-6}. In such circumstances absorption by a gas, such as methane, with an absorption coefficient of the order of 10^3 atm^{-1} m^{-1} would be negligible. The loss value for a mode may be calculated using its r value in the modified Beer-Lambert expression $I = I_o e^{-r\alpha cl}$ (cf. section 3.5). This result obtained from perturbation theory is only valid where $n_i << n_r$ which is true for most gases. This method will be used throughout this section for calculating the sensitivity of tapers and also to compare with the predictions of the extended planar waveguide model.

To determine the compliance of taper T46 with the adiabaticity criterion the simple constant volume model is used to calculate the magnitude of the fibre nonuniformity. The measure of nonuniformity used is derived from the rate of change of taper diameter and is called the local taper length scale z_t [29]. The geometrical representation of z_t is depicted in figure 6.15is defined as '*the height of a right circular cone with base coincident with the local core cross section and apex angle equal to the local taper angle*' [29]. To satisfy the adiabatic criterion, the nonuniformity must occur over a distance large compared to the beatlength z_b. This condition may be written as $z_t >> z_b$, everywhere.

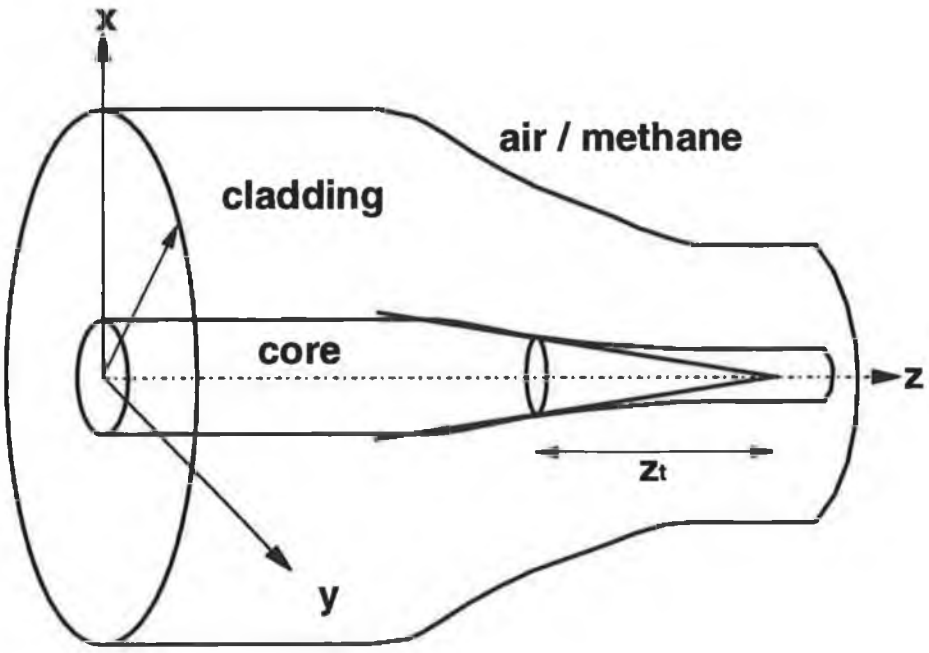

figure 6.15 graphical representation of the local taper length scale z_t at an arbitrary position in a fibre taper

From the simple constant volume taper model it emerges that z_t is equal in magnitude to the taper waist length. Table 6.1 shows values z_t for discrete values of the taper waist length in mm. The table also shows that the value of z_t approaches the value of the taper waist length asymptotically as the incremental stepsize dl (cf. figure 4.11) is reduced. The taper waist is directly related to the effective furnace length [30] using the parabolic taper shape model introduced in section 4.3.2. Therefore the degree of compliance of a taper with the adiabatic criterion is a function of the furnace length used.

taper waist length (mm)	local taper length-scale (mm)	model stepsize, dl (mm)
1	1.2071	1
1	1.0244	0.1
1	1.000249	10^{-3}
5	5.2386	1
5	5.0248	0.1
5	5.00025	10^{-3}

Table 6.1 local taper length-scale as a function of taper waist length and simple constant volume model stepsize

From the simple constant volume model the local taper length scale z_t for taper T46 is 2 mm. To satisfy the adiabaticity criterion the beat length ($z_b = 2\pi/(\beta_1-\beta_2)$) between the HE_{11} mode and the mode to which it most strongly couples must satisfy the condition $z_b << z_t$. In a perfectly axisymmetric taper coupling will occur between modes of the same azimuthal symmetry [29]. Therefore, in calculations of z_b, $\beta(HE_{11})$and $\beta(HE_{12})$ (the LP01 and LP02 modes of a weakly guided fibre) are normally used. This condition shall be applied here. In figure 6.16 the magnitude of z_b is plotted as a function of the taper reduction ratio. Using the finite and infinite clad fibre theory of Unger [16], detailed in chapter 3 and Appendix B, the respective values of β for the HE_{11} and HE_{12} local taper modes are calculated. The finite clad fibre theory is used to calculate the values of β before the fundamental mode is cutoff. The infinite clad fibre theory is used in conjunction with the no-core approximation to calculate all other values of the fundamental mode and all values of HE_{12}. The effect of this approximation is to slightly underestimate z_b where the core radius is not negligible. The discontinuity in the graph of z_b is due to the change from the finite clad model to the infinite clad model at the cutoff of the HE_{11} mode. The infinite clad model neglects the influence of the core and underestimates the effective index of the fundamental mode.

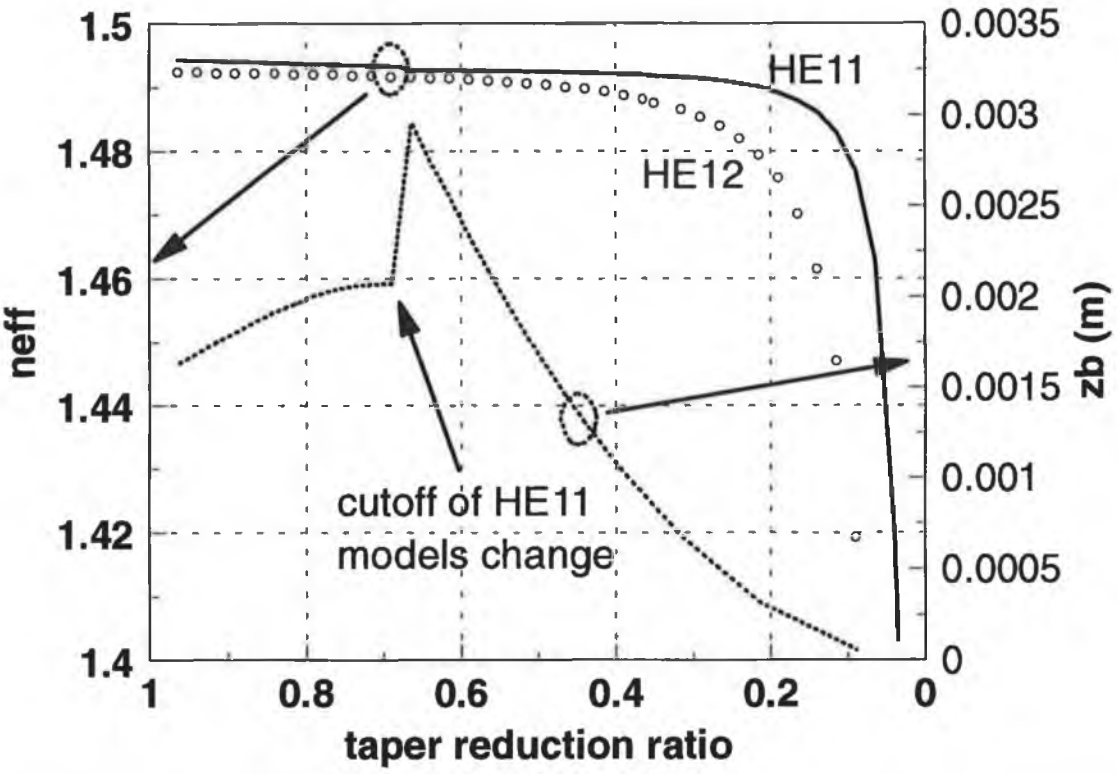

figure 6.16 HE_{11} and HE_{12} mode effective indices and beat length (z_b) as a function of taper reduction ratio

From figure 6.16 the maximum value of z_b is almost 3 mm. Therefore taper T46 does not satisfy the adiabatic criterion as $z_t < z_b$ for this taper. Using the calculated value for z_b the minimum value of the taper waist length to produce an adiabatic taper can be estimated. To satisfy the condition $z_t >> z_b$, z_t must be at least an order of magnitude greater then z_b. For example, using z_b = 2.95 mm, a taper waist or effective furnace length of 30 mm is required to fabricate an adiabatic taper from the 11/125 μm single mode fluoride fiber.

Using the taper waist length calculated above for an adiabatic taper and assuming that the waist of the taper is the sensing region, the required taper reduction ratio, to achieve a taper loss of 10% for 5% methane in air @ λ = 3.392 μm, can be calculated. Using the equation $I = I_o e^{-r\alpha cl}$ with $I = 0.9I_o$, l = 0.03 m, c = 0.05 relative partial pressure and α = 900 atm^{-1} m^{-1} the required cladding to total power ratio (r) is calculated to be 0.078 (7.8%). Using the infinite cladding theory in the no-core approximation [31] for 11/125

μm fibre the cladding power ratio, exceeds 8% for a taper reduction ratio of 0.023 (equivalent to a taper waist diameter of 2.9 μm). Using the taper waist length required to satisfy the adiabatic criterion (30 mm) the simple constant volume taper shape model predicts a taper pull length of 450 mm to generate a taper reduction ratio of 0.023. A taper pull length of 115 mm is calculated using the parabolic taper shape model for identical taper waist parameters [30]. The taper pull length as a function of diameter reduction for a taper waist length of 30 mm is shown in figure 6.17. The fundamental difference between the two theories is the prediction of a maximum pull length before the taper breaks. The parabolic model predicts a ratio of maximum pull length to taper waist of 5. The simple model makes no prediction of maximum pull length except one that may be arbitrarily set on the basis of a minimum allowed taper diameter. In addition, the taper shape generated using the parabolic model is more realistic than the simple constant volume model as may be seen from figure 4.13. Therefore, the pull length predicted by the parabolic model is likely to be the most accurate.

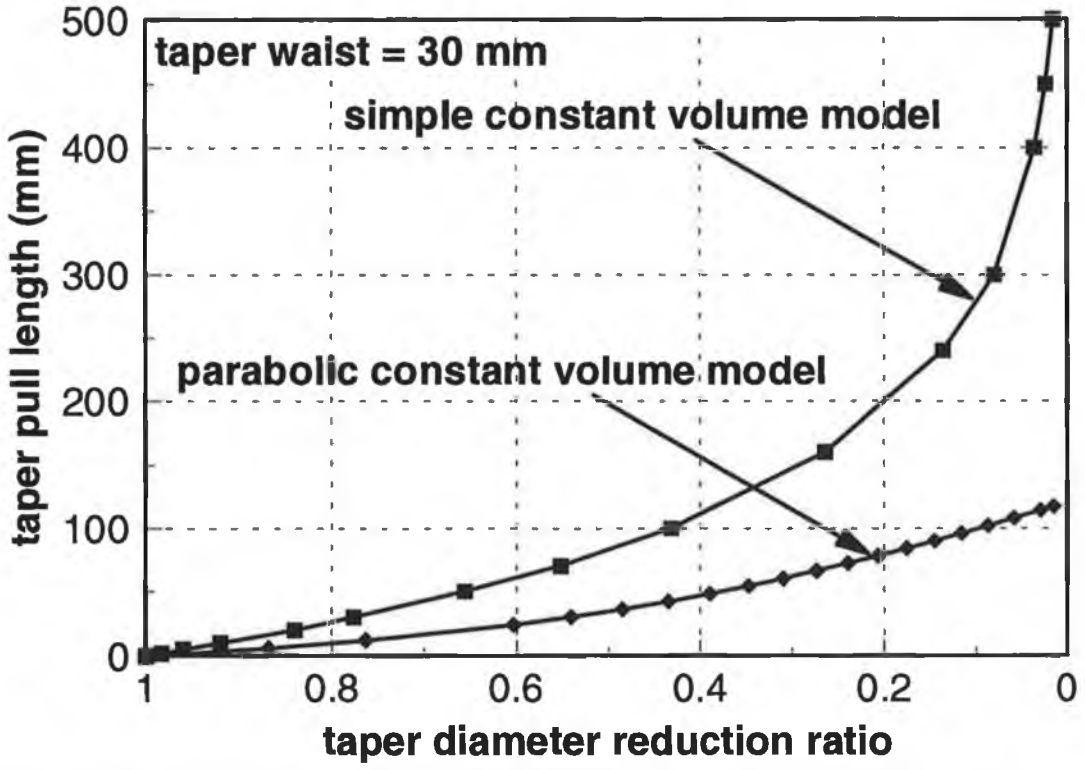

figure 6.17 parabolic vs simple taper shape models used to predict pull length for an adiabatic taper (taper waist 30 mm) as a function of the required diameter reduction ratio.

The calculations outlined in this section indicate that a point sensor can be fabricated from single mode fluoride optical fibre that suffers a 10% loss in throughput @ 3.392 μm when exposed to the LEL of methane at 1 atmosphere. Such a taper would have a minimum detectable concentration significantly lower than the LEL of methane provided that a signal to noise of at least 100 is achieved. The parameters predicted are waist diameter 2.9 μm, waist length 30 mm and taper pull length greater than 10cm. The fluoride fibre tapers pulled in this investigation do not meet the adiabaticity requirements calculated for the single mode fluoride fibre. In addition, the tapers pulled have an evanescent field penetration smaller, by at least 4 orders of magnitude, than the requirements for a viable taper sensor. This explains the tapers lack of sensitivty to gaseous analytes.

6.3.4 Independent taper results.

This section compares the predictions of taper theory with both measured and published experimental results where tapers were used to sense flammable gases. Tai *et al.* [9] published results for methane sensing using multimode silica fibre tapered to monomode and few-mode operation. The sensitivity, waist diameters and lengths quoted are tabulated below along with the predictions of sensitivity from the infinite clad fibre model in the no-core approximation. The fibre parameters n_{core} = 1.515 and n_{clad} = 1 are estimated from the quoted V-numbers for the tapers. The planar approximation uses a guiding layer equal to the taper waist diameter and the extended planar model is limited to the rectangular waveguide approximation of Marcatili (cf. section 3.2) as the tapers are too small for further subdivision.

Waist diameter (μm)	Waist length (mm)	r measured	r (infinite cladding)	r (planar waveguide)	r (extended planar model)
2.8	10	0.12	0.145 HE_{11} 0.01 TE_{01} 0.21 TM_{01} 0.22	0.17 TE_0 0.03 TE_1 0.16 TM_0 0.07 TM_1 0.43	0.21 TE_0 0.12 TE_1 0.3
1.8	10	0.40	HE_{11} 0.52	0.16 TE_0 0.08 TM_0 0.24	0.367 TE_0 0.367

Table 6.2 Measured and predicted sensitivity (quoted as cladding power ratio) from infinite cladding, planar waveguide and extented planar models. Where more than one mode is supported the average of all modes is quoted above the values for individual modes. Data from Tai et al [9]

The agreement between theory and experimental data in the above table is quite good. To estimate the r value where more than one mode is allowed the r values for all the modes are averaged. The infinite cladding model is within 25% of the measured value in both cases. The planar waveguide model shows the largest discrepancy. It under-estimates the single mode taper sensitivity by 100% and overestimates the few-mode taper sensitivity by 40%. The extended planar model is within 10% of the single mode taper value but it over-estimates the few-mode taper sensitivity by 80%. In the extended planar theory using a rectangular approximation, the TE and TM modes are identical and for this reason only the TE modes are quoted. No information is available about the adiabaticity of the tapers pulled and for the local mode predictions to be accurate the tapers must be adiabatic.

Figure 6.18 shows a spectrum of 100% propane obtained using the single mode fibre taper supplied for this work by Le Verre Fluore. The spectrum was recorded using an FTIR spectrometer set at 16cm^{-1} resolution and was averaged 500 times. The peak propane absorption is 13% at 2961 cm^{-1} (3.37 μm). The taper dimensions were measured to be as follows: taper waist length 28 mm, taper waist diameter 15 μm and taper gradient 0.053° over 12 mm [26]. The measured gradient is equivalent to a minimum local taper length scale z_t of 8 mm which is only slightly greater than the beat length z_b of 3 mm. Assuming single mode operation, this taper should be unable to sense any of the flammable gases as the V number in the taper is 16 @ λ = 3.37 μm and the r value of the HE_{11} mode is less than 1 x 10^{-6}. The r value estimated from the experimental data is 0.005. This r value can only be accounted for by assuming that higher order modes are contributing to the sensitivity in the measured spectrum. Some of the power in these modes may be recaptured and delivered to the detector in an abrupt taper, or alternatively, some of the power from the higher order modes may be coupling back into the fundamental mode along the length of the taper.

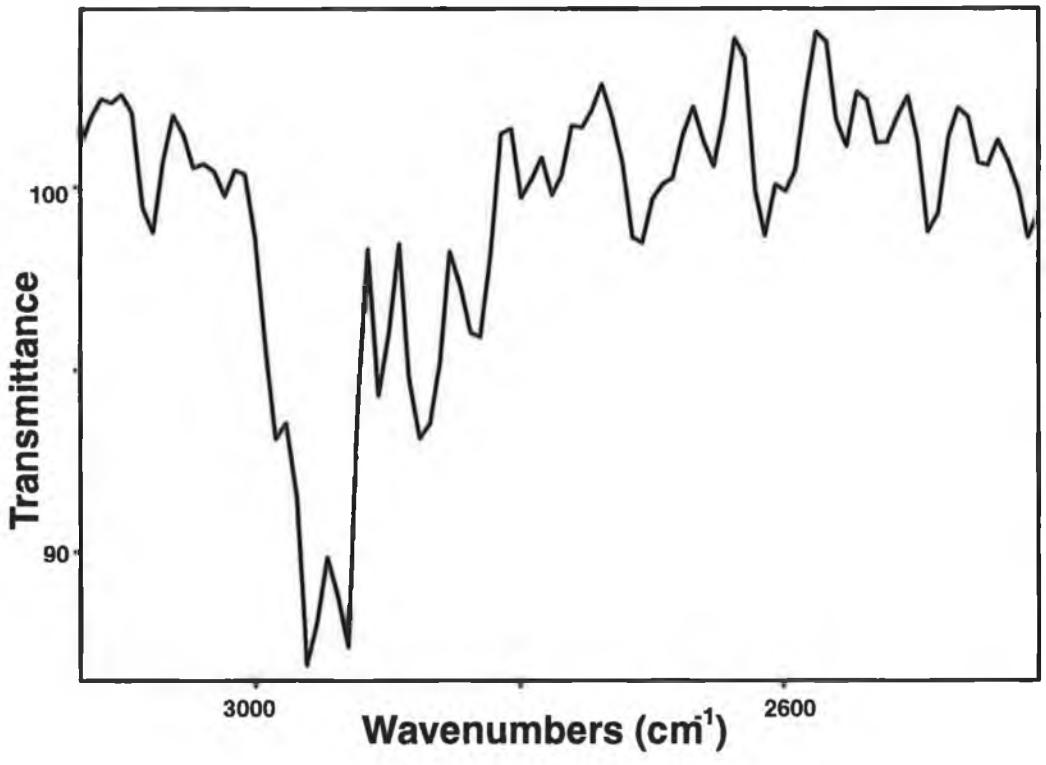

figure 6.18 Propane spectrum obtained with a 11/125 μm single mode fluoride fibre taper supplied by Le Verre Fluore, France.

6.3.5 Conclusion

The previous discussion highlights the sensitivities that may be achieved using tapered fluoride fibres. Although it is possible to fabricate silica tapers with the dimensions required for viable gas sensing, the losses of silica fibre in the mid infrared make them unsuitable for remote sensing. Fluoride fibre tapers with the required dimensions have not been produced to date because of the material problems associated with fluoride fibre.

6.4 Teflon Clad Fibre.

6.4.1 Introduction.

The mechanical stability of the polished fibre block structure and the distributed nature of D-shaped fibre make them attractive as potential gas sensors. However, these sensors have very low sensitivity per unit length to gases and are prone to fouling because of the exposed nature of the sensor. It is possible to achieve high sensitivity with tapers but fluoride fibre tapers are very fragile and difficult to fabricate. Evanescent wave mid-infrared liquid-phase sensors have been reported using bare-core multimode fibres [32,33,34]. Bare-core fibres suffer from the same fouling problems as other evanescent wave sensors. In many cases, short lengths of bare-core fibre are used as sensing elements in enclosed cells with cabled clad-fibre carrying the signal to and from the sensor.

In this section the results obtained using a multimode Teflon clad fibre (Infrared Fiber Systems Inc., USA) as a gas sensor are discussed. In contrast with glass clad fibre the cladding of the fibre is gas permeable and does not have to be removed to allow the gas to interact with the evanescent field. As has already been discussed, the porous overlayer is capable of improving the fibres sensitivity to absorbing media of low refractive index by increasing the penetration depth of the evanescent wave. Another advantage of the Teflon clad sensor is its improved immunity to surface fouling and protection against degradation of the fibre by exposure to water vapour.

Data are presented for two multimode fibres with different core / cladding diameters using different sets of experimental apparatus. A 280/300 μm fibre was investigated using standard components described below. Another set of data was obtained using a novel room temperature mid infrared solid state source with a smaller diameter 200/210 μm fibre. The solid state source will be detailed in section 6.5.

6.4.2 Experimental Apparatus.

Two experimental systems were used to obtain the data in this section. The experimental system for the 200/210 μm fibre LED based measurements is described in section 6.5.2 and depicted in figure 6.26. The experimental system for the 280/300 μm fibre is shown in figure 6.19. Light from a 50 Watt tungsten halogen source is focused onto the input slit of a f/3.9 monochromator using a f = 20 mm IRGN6 lens. The monochromator (Optometrics Inc., USA) is a Fastie-Ebert in-line design with a 2 μm blaze wavelength. The optical signal was modulated by a mechanical chopper (Bentham 218F, Bentham Instruments, Reading UK) and detected using a PbSe detector thermoelectrically cooled to 240K and biased at -100Vdc. A lock-in amplifier (Stanford Research SR510, Stanford Research Systems Inc., USA) was used because of the very small signal to noise ratio of the system.

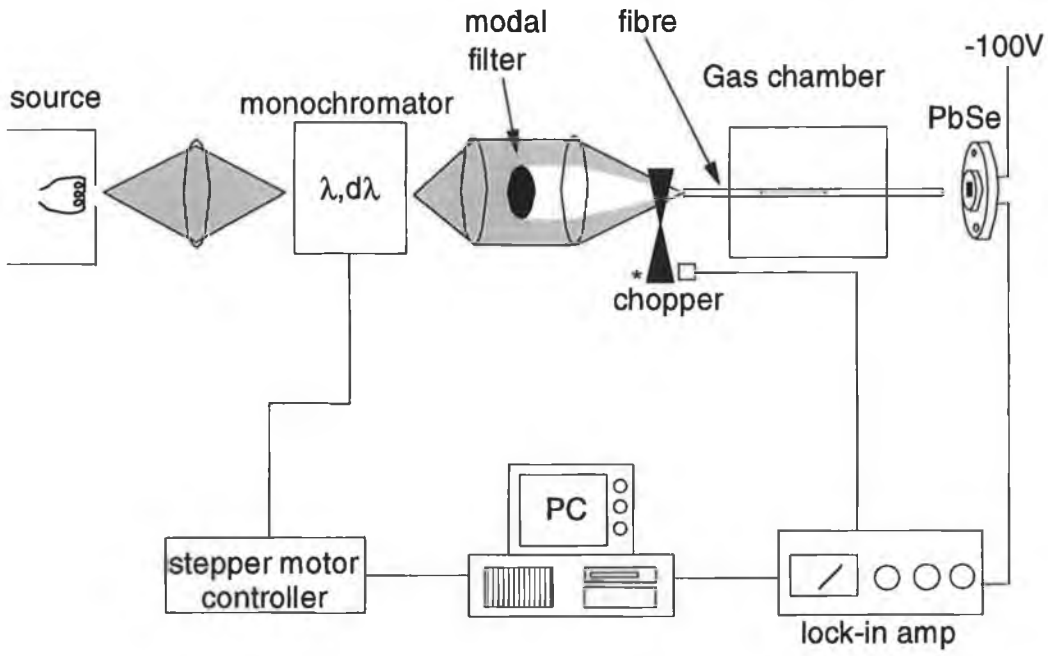

figure 6.19 Incandescent source based experimental system for Teflon fibre gas absorption measurements (system 1)

6.4.3 Experimental measurements (system 1).

The fibre attenuation in the spectral region of interest (3.3 - 3.4 μm) is between 0.8 and 1 dB/m and the fibre NA is specified to be 0.6. Using the known fluoride glass refractive index of 1.5 at 3.4 μm and the relationship NA = $(n^2_{\infty} - n^2_{cl})^{1/2}$, the refractive index of the Teflon cladding is calculated as 1.375. This value agrees closely with a quoted value of 1.376 at 589 nm [35]. The cladding porosity was measured as 42% (98% N_2, 2% He) using a Micrometrics Pulse Chemisorb 2700. Using these figures the increase in evanescent wave absorbance compared to an unclad fiber can be calculated. An absorption coefficient for propane of 900 atm^{-1} m^{-1} at 3.39 μm is used in these calculations [36] which predict evanescent wave absorbances of 0.0287 for gas only and 0.1448 for Teflon and gas mixture. The fibre parameters are n_{core} = 1.5, core radius = 100 μm, sensor active length = 10 cm and the launched NA is 0.58 in both cases. A launched NA of 0.58 is used because it is very close to the maximum allowed NA for the Telon clad fibre. From this calculation it can be seen that the Teflon cladding significantly increases the absorption assuming identical launch conditions. If the calculation is extended to include the higher order modes for the bare-core fibre, which

has a theoretical NA of 1.11, the gap between sensitivities narrows as shown in table 6.3. Launching (parallel to the fibre propagation direction) a light beam of NA greater than 0.8 is difficult and beyond 1 it is not possible.

10 cm interaction length, 100 μm radius, Core index 1.5, λ = 3.39 μm		
Launched NA (from - to)	Teflon clad absorption (NA-0.58 max)	Core only absorption
0 - 0.3	0.0277	0.0071
0 - 0.58	0.1448	0.0287
0 - 0.7	0.1448	0.0443
0 - 0.85	0.1448	0.073

Table 6.3 Bare-core fibre vs Teflon clad fibre gas sensitivity as a function of launch NA

An evanescent wave absorbance spectrum of propane taken with the mechanically modulated tungsten halogen source system (chopper frequency 260 Hz, time constant 1sec) is shown in figure 6.20. To obtain this spectrum lower order modes, corresponding to a launch NA less than 0.45, were not launched into the fibre. They were blocked by means of the modal filter shown in figure 6.19. This enhances the gas absorption signal measured because higher order modes have a greater evanescent penetration into the cladding/analyte. The spectrum has the double peak shape characteristic of propane. A high resolution propane spectrum is included in Appendix E for comparison. The active sensor length is approximately 12 cm. This spectrum was taken after the fibre had been exposed to the gas for more than a half hour. The gas must diffuse fully into the cladding before the measured absorption reaches its maximum. Typical gas diffusion curves are shown in figure 6.21. The two sets of data were taken with the same fibre and show the repeatibility of the diffusion process. The signals recover to their original level after longer exposure to an N_2 atmosphere than shown in the graph.

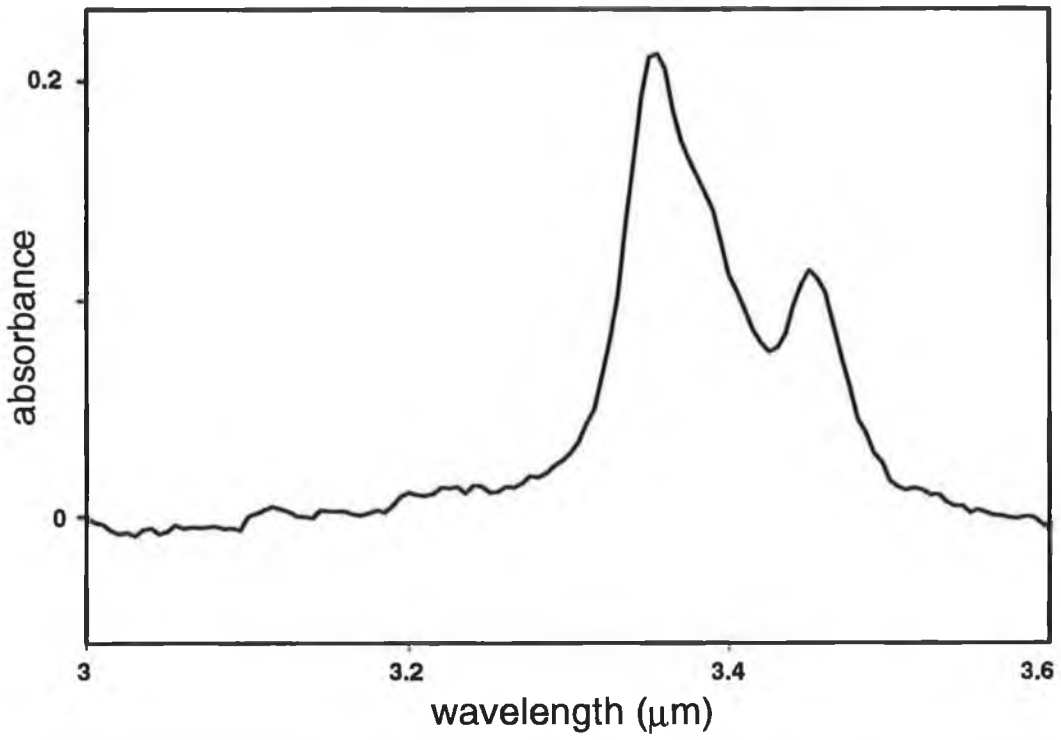

figure 6.20 Evanescent wave propane absorbance spectrum of 280/300 μm Teflon clad Fluoride fibre for 12 cm interaction length

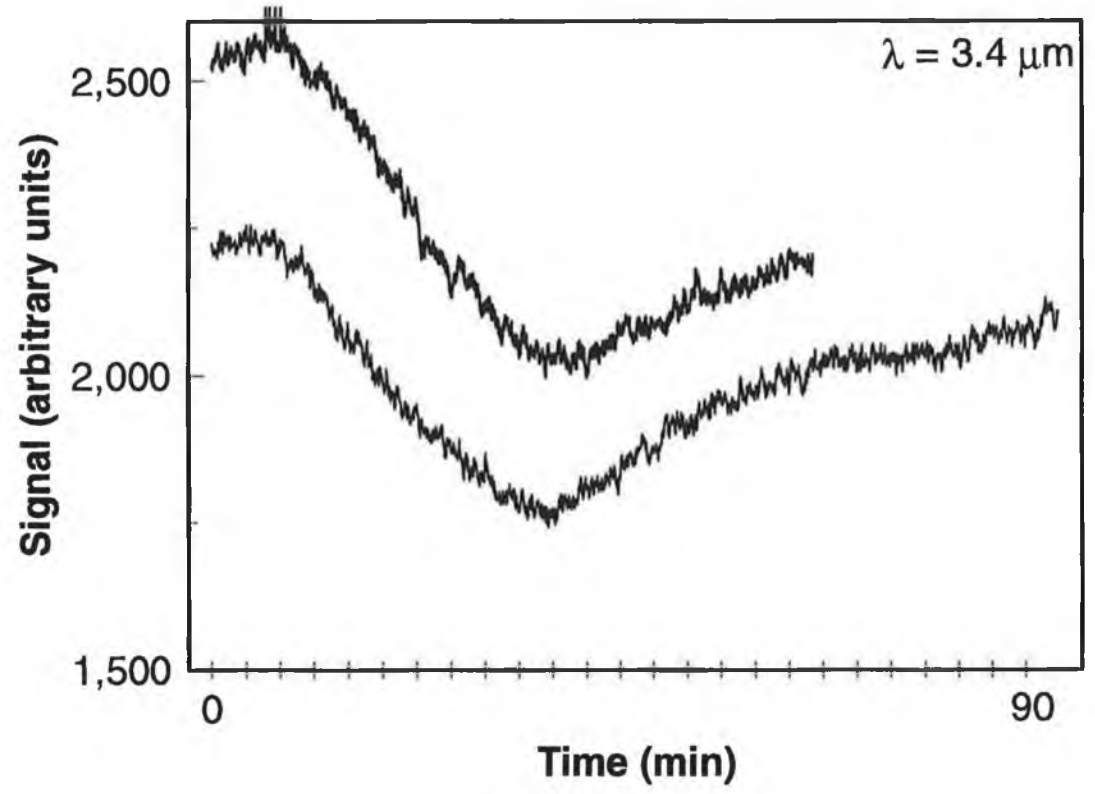

figure 6.21 Teflon clad fibre absorption signal as a function of time in a propane atmosphere at 3.4 μm. Two scans are depicted to show repeatability of diffusion process.

The diffusion properties of the Teflon cladding have been modelled [3] assuming Fickian diffusion in a cylindrical surface. The gas concentration as a function of time and normalised to the concentration at t = ∞ can be expressed by [37]

$$\frac{c(r,t)}{c_\infty} = \sqrt{\frac{b}{r}}\,\mathrm{erfc}\left[\frac{b-r}{2\sqrt{Dt}}\right] \qquad 6.2$$

where D is the diffusion coefficient, r is the radial distance from the core, b is the cladding radius and t is the time elapsed. Equation 6.2 is valid provided $Dt/b^2 < 0.02$. Using equation 6.2 and the exponential decay of the evanescent field in the cladding for each ray angle as explained in section 2.5 the absorbance as a function of time may be calculated. The diffusion coefficient is then varied until the calculated absorption as a function of time matches that of figure 6.21. The diffusion coefficient predicted by this theory is 8.85 x 10^{-14} m^2s^{-1} which is within 15% of the value quoted for propane of 7.7 x 10^{-14} m^2s^{-1} [38].

In Ruddy *et al.* [3] the effect of the modal filtering performed at the fibre input is underestimated. In figure 4 of this paper a theoretical comparison of the absorption for a filtered and unfiltered experiment is shown. In that work the predicted difference in absorbance is negligible (<0.02 absorbance units). However, using the fibre ATR theory of section 2.5 and correcting the number of calculated reflections for the Goos-Haenchen shift at each total internal reflection [39] a much larger effect is predicted. For a launched NA of between 0.45 and 0.58, which is equivalent to the experimental NA launched, an absorbance of 0.36 is predicted. For these calculations an absorption coefficient of 380 atm^{-1} m^{-1} is used. This is equivalent to the propane absorption coefficient of 900 atm^{-1} m^{-1}, corrected for the porosity of Teflon (42%). For a launched NA of between 0 and 0.58 an absorbance of 0.12 is calculated. Therfore the modal filtering employed increases the predicted absorbance by a factor of three or equivalently a difference of 0.24 absorbance units. These predictions are confirmed experimentally in the next section using the mid infrared LED source.

6.4.4 Experimental measurements (system 2)

Figure 6.22 shows two absorption spectra recorded using system 2 which consists of a solid state source and an InSb detector as will be described in section 6.6. The spectra were taken with and without modal filtering and show experimentally the increased response that can be achieved using modal filtering. The smaller absorbance (0.0868) at 3.36 μm was recorded without modal filtering using all power up to a maximum detected NA of 0.38. The second spectrum was recorded with the same maximum NA but all power below an NA of 0.24 blocked. The predicted absorbance at these NA values is 0.101 without filtering and 0.207 with the filter in place (these data are tabulated in Table 6.4). The increase in the measured absorbance using modal filtering is in fact larger than that predicted using simple ATR theory.

launched NA (from - to)	measured absorbance @ 3.36 μm	Predicted absorbance
0 - 0.38	0.0868	0.101
0.24 - 0.38	0.25	0.207

Table 6.4 Predicted and measured response for modal filtered and unfiltered spectra

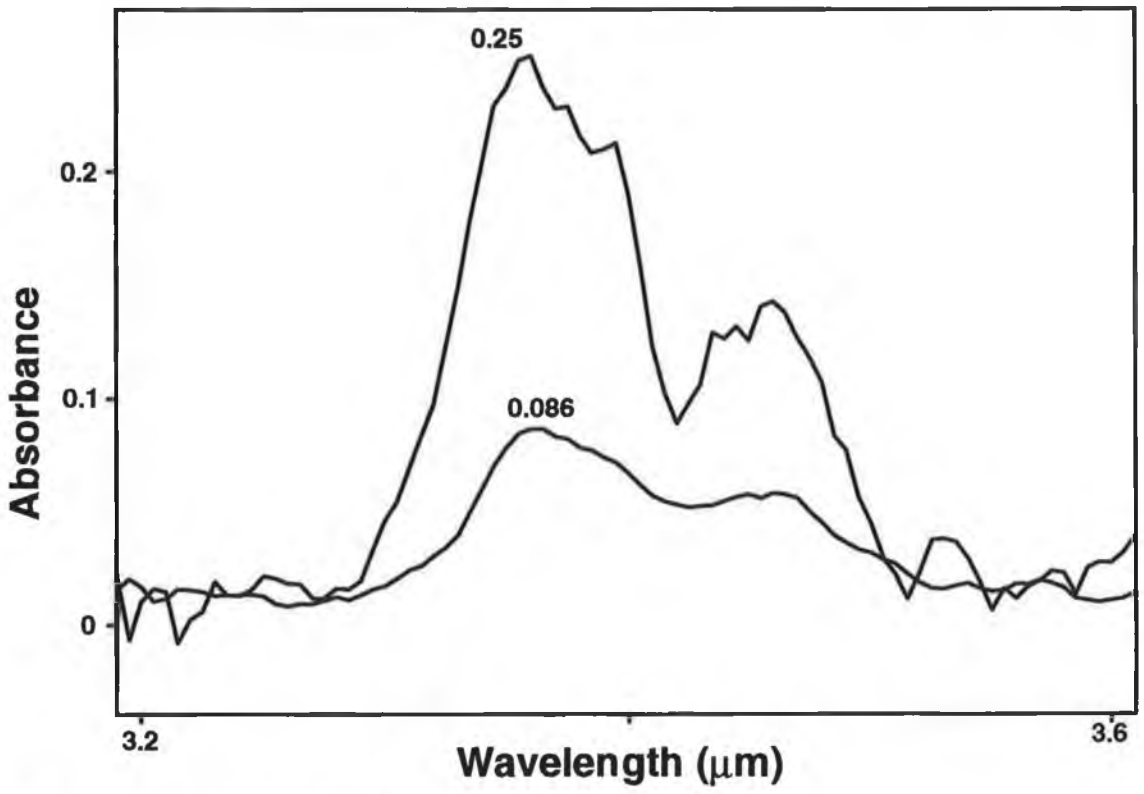

figure 6.22 Absorbance of Propane for 200/210 μm fibre using solid state source.

The increased response achieved with modal filtering has an associated disadvantage. Restricting the range of modes to be analysed reduces the power detected. This can be seen in figure 6.22 where the noise on the spectrum obtained by modal filtering is significantly greater than for the unfiltered spectrum. Figure 6.23 shows the throughput (normalised to 1) and absorbance signal as a function of the range of blocked modes for the Teflon clad fibre. For a given x value, modes from an NA of x to an NA of 0.55 are launched. The power distribution is assumed to be even over all the modes launched and the modes are assumed to be evenly spaced as a function of launch angle. The normalised absorbance signal to noise ratio is also plotted. This gives an indication of how the minimum detectable concentration of the analyte varies with modal filtering. The minimum detectable concentration must generate an absorbance signal at least twice the absorbance noise of the sensor. Contrary to what one might expect there is no increase in the minimum detectable concentration of analyte using modal filtering. This is due to the fact that the absorbance signal ratioed to the noise expressed as an absorbance is a maximum when all modes are launched.

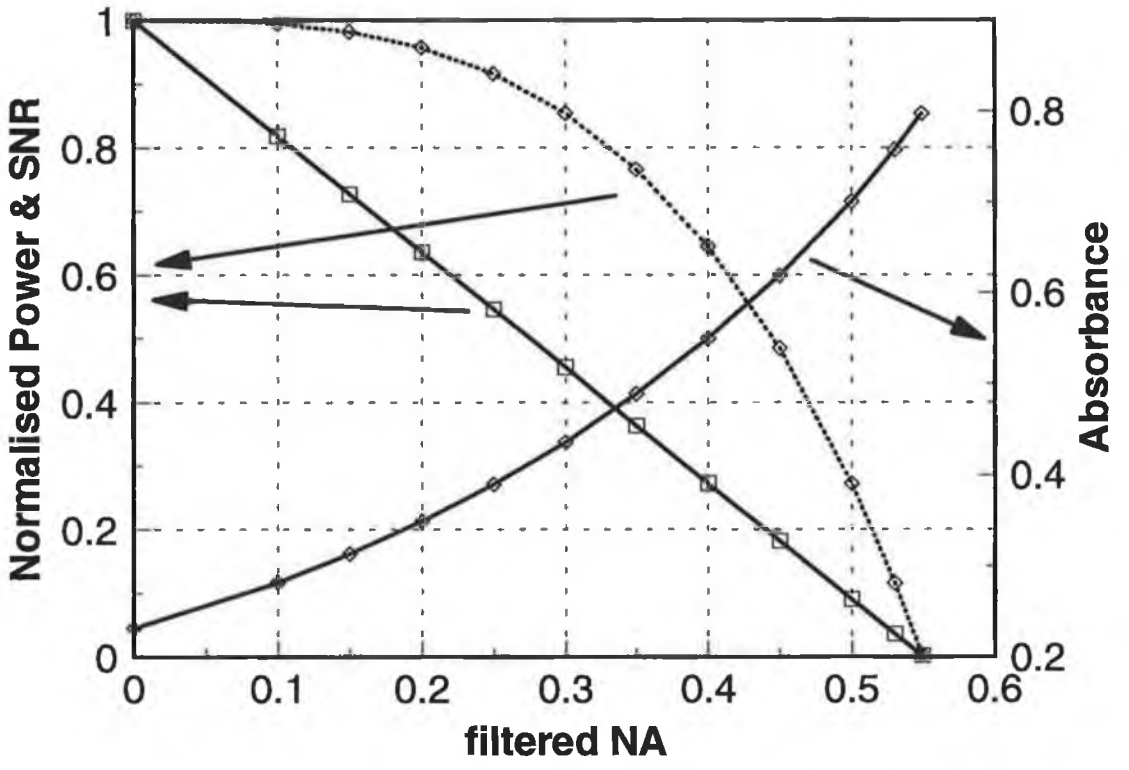

figure 6.23 effect of blocking low order modes on absorbance and absorbance SNR for Teflon clad fiber

To test the validity of the above calculation the minimum detectable concentration over the specified interaction length is calculated for the data in figure 6.22. The measured noise on the spectra are approximately 0.0017 and 0.01 absorbance units for absorbance signals of 0.0868 and 0.25, respectively. The signal to noise ratios are 51 and 25, respectively. The minimum detectable concentration (MDC) is required to be that which generates a signal at least twice the noise level. Therefore the MDC is 3.9% for the unfiltered system and 8% for the filtered system. The MDC per unit length for the unfiltered sensor is less than 1% propane. This overestimates the sensitivity of the sensor because the throughput will decrease with length due to the fibre attenuation and consequently the SNR will decrease.

6.4.5 Conclusion

The Teflon clad multimode fluoride fibre gas sensor is the most sensitive of all of the configurations tested. The predicted MDC of 1% propane per unit length is promising

for a stable and robust evanescent wave senor. In addition, the fibre is less sensitive to surface contamination than either polished or tapered single mode sensors. Furthermore, teflon protects the fibre surface from water attack which would pose a serious problem for any exposed fluoride fibre. The use of a solid state source, discussed in the next section, is also a promising development for mid infrared fibre based gas sensing. Such sources require much less power than the tungsten halogen source or the glowbar source used in the FTIR. High attenuation (1dB/m), however severely limits the use of the Teflon clad fibre for distributed sensing applications. A replacement for the Teflon cladding is therefore required to enable the use of the highly sensitive porous clad structure in practical remote or distributed sensing applications for which optical fibre is suited.

6.5 Solid state mid-IR source.

6.5.1 Introduction

The primary problem to date in the development of fluoride fibre based gas sensors, in particular distributed evanescent wave sensors, is the lack of mid-IR sources suitable for use with optical fibres. High power sources such as glowbars and incandescent lamps, discussed in section 5.2, have large emission areas and cannot be coupled efficiently to multimode optical fibres with core radii of the order of 100 μm or less. Current research [18,19] into distributed gas sensors concentrates on the weaker 1-2 μm absorption band because of the availability of suitable semiconductor devices operating in this region for use with ultra low loss silica fibre. LED's that emit in the mid-IR region are now becoming available and the next section covers the practical use and characterisation of one such device.

6.5.2 Experimental Apparatus.

The experimental system used to test the LED as a source for evanescent wave gas sensing is shown in figure 6.24. To obtain the maximum possible output power from the LED it is necessary to pulse it with a high current at a very low duty cycle. To detect

this fast pulse an InSb detector (Graseby Infrared, USA) coupled to a current sensitive preamp (Ithaco1642) was used as detailed in chapter 5.3.2. The timing was controlled by a voltage controlled oscillator VCO [AD654] driving a one shot monostable [74LS122]. The VCO also drives the data line of a 12 bit analog to digital converter (ADC) PC card to trigger the conversion. The offset between the arrival of the trigger pulse and the triggering of the ADC's sample and hold was controlled in software. The gas chamber, designed in house, is detailed in chapter 5. The monochromator (Optometrics, USA) is blazed for maximum efficiency at 3.5 μm.

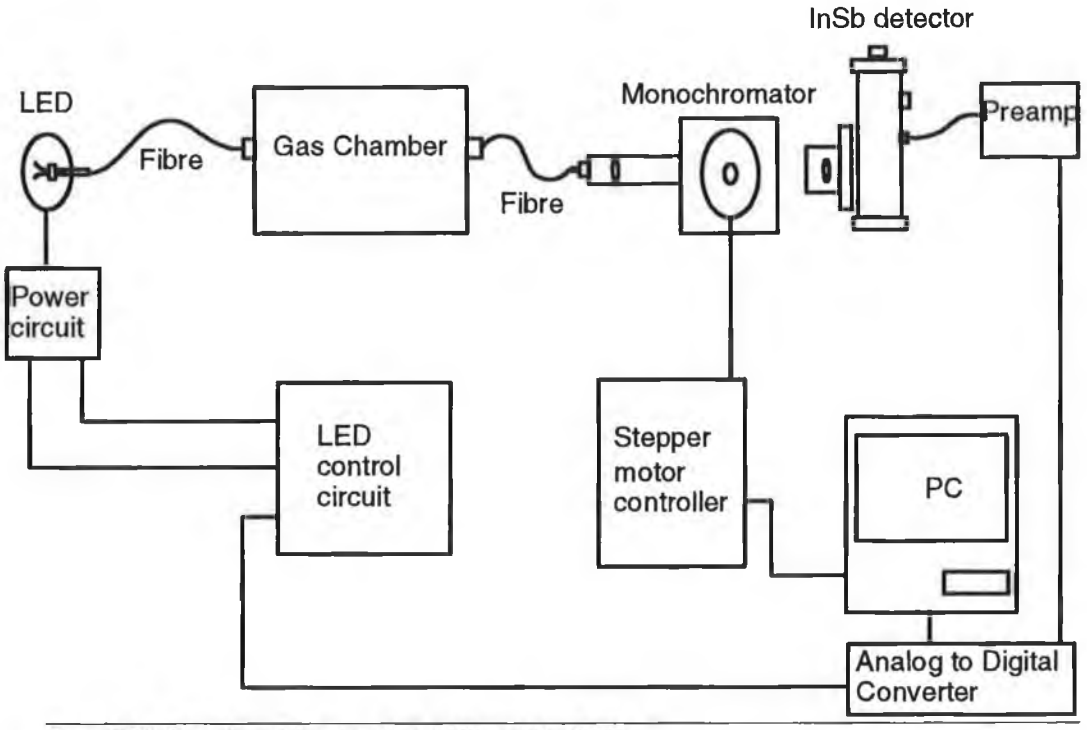

figure 6.24 Experimental system for mid IR emitting LED

6.5.3 Experimental Results

The LED used in this investigation is a room temperature InGaAs device (Mostek Inc., Russia) that has been used for free space flammable gas detection [40]. The LED emits at a central wavelength of 3.31 μm with a bandwidth (full width half max) of 400 nm as may be seen in figure 6.25. The output coincides with the mid IR absorption region of the flammable gases associated with the C-H bond stretching vibration. To obtain the

spectral data the LED is pulsed at 3A at a frequency of 100 Hz and a pulse width of 10 μs. The duty cycle is kept low to negate self heating in the LED.

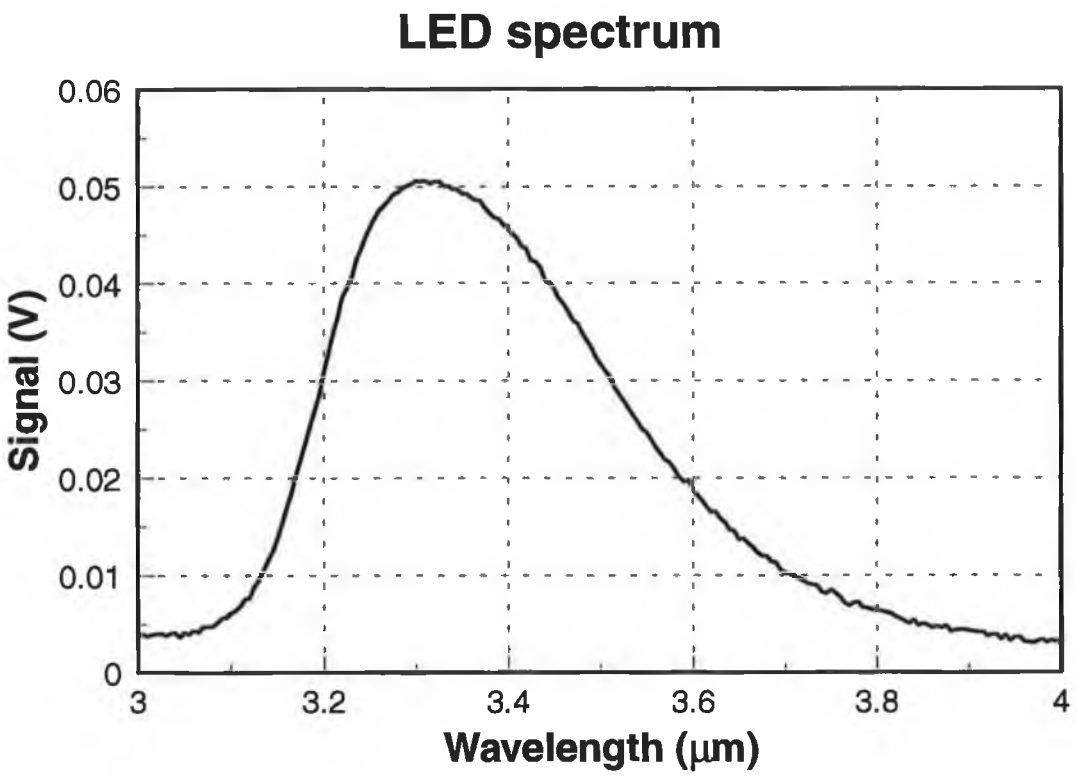

figure 6.25 InGaAs LED spectrum

The 250 μm square emitter of the LED is mounted at the focus of a parabolic reflector as shown in figure 6.26. While this feature was not used in the measurement system when launching into fibres, it is very useful for free space gas detection as a result of the reduced beam divergence of 62 mrad. A profile of the LED output power, measured in a plane perpendicular to the source, at a distance of 120 mm is shown in figure 6.27 and demonstates quite clearly the degree of collimation of the LED output. The lines in the plot represent constant signal intensity (given in μV).

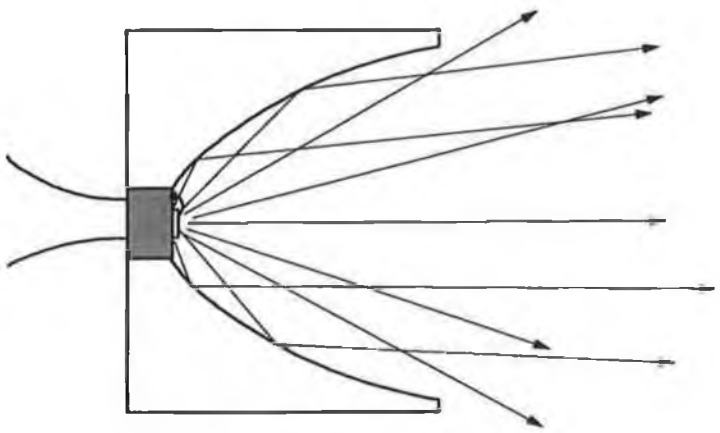

figure 6.26 Cross section of LED through emitter showing collimating effect of parabolic reflector

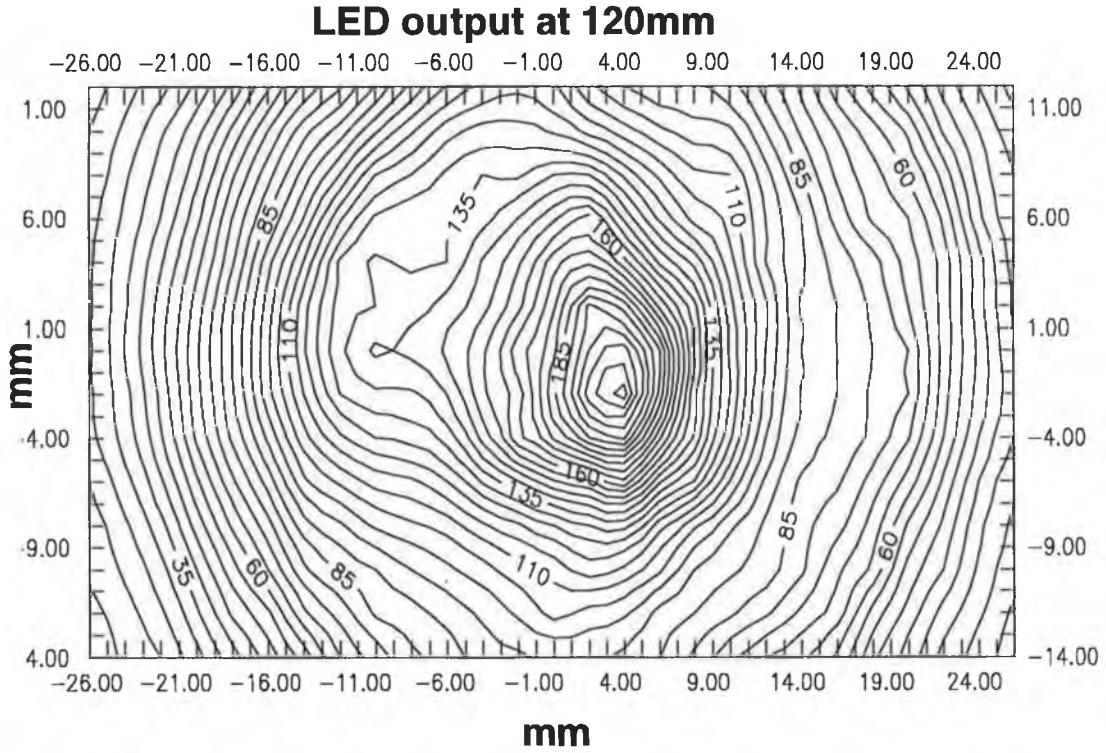

figure 6.27 Output of LED 120 mm from the source in a plane perpendicular to the emission. Lines in the plot represent constant signal intensity in μV.

The total power emitted by the LED was measured by integrating the cross section above and using the average responsivity (A/W) of the InSb detector weighted over the emission of the LED. The total power is between 70 and 100 μW. This is significantly smaller than the output of 5mW quoted by the manufacturer using similar currents and duty cycles. The LED power was launched into the Teflon clad fibre by butt-coupling i.e. no launch optics employed. The total power delivered in this mode by 0.5 m of 200/210 μm Teflon clad fibre to the detector is between 1 and 2 μW. This represents a launch efficiency of 2%. Using a small length of 300/320 μm fibre from the same manufacturer an efficiency greater than 20% was realised. In the first case the emitter is larger than the fibre core and this contributes significantly to the small launch efficiency because butt-coupling was employed to launch the light.

The LED performed without noticeable signal degradation over continuous periods greater than 100 hours. However, if the LED was not used for a long period e.g. a number of months, the LED's were found to fail when pulsed at high currents. The failure of the LED was normally a result of the wire bond becoming detached from the emitter.

6.5.4 Conclusion

The InGaAs LED described here has been used in conjunction with Teflon clad fluoride optical fibre to detect propane gas. The LED has great potential for IR fibre gas and liquid sensing but its output power and coupling efficiency need to be improved. To improve the source for optical fibre applications the emission area must be reduced to minimise the power lost at launch. The LED used is a surface emitting device (SLED). These LED's have larger emitting areas and greater divergence than edge emitting LED's (ELEDs). For fibre operation, increased launch efficiency would be obtained if such a device were fabricated in an edge emitting configuration.

Mid-IR LED's manufactured by Mostek are available for particular wavelength bands over the range of useful operation of fluoride fibre, i.e. from 2 to 5 μm. These mid-IR LEDs have many advantages over other infra-red sources for use with optical fibre because of their small size, low power consumption and low cost. Their low power consumption make them ideal for use in portable battery powered systems. Recent publications show that research is currently being undertaken independently on similar devices [41]. The possibility of cheap laser diodes which are now being fabricated [42,43] from the same materials improves dramatically the prospects for remote or distributed mid-IR optical fibre based sensors.

6.6 Comparison of evanescent wave sensors

Of all the sensors fabricated and evaluated, the only one with which a flammable gas was detected was the Teflon clad multimode fibre. The polished and tapered sensors did not have the sensitivity required to detect flammable gases. The polished fibre sensitivity is inherently small as a result of modal confinement caused by the difference in refractive index between cladding and analyte, and by its short interaction length. The tapered sensor has no such fundamental limitation on its sensitivity to a gaseous analyte. The reason for the inability of fabricated tapers to detect flammable gases was due to the difficulty in fabricating a taper with the required dimensions (cf. section 6.3.3).

A measure of the sensitivity per unit length of an evanescent wave sensor is the ratio of power in the analyte to the total guided power in the waveguide, r. Typical r values are quoted in table 6.5 for each of the sensors discussed in this chapter.

Sensor	r value	interaction length (mm)
Polished	$< 10^{-4}$	10
Tapered	$< 10^{-6}$	5
Teflon clad	0.01	120

Table 6.5 Representative sample of evanescent wave sensors used with corresponding r values and interaction lengths

1. Lewis B., Elbe G.: '**Combustion Flames and explosions of gases**', Academic Press, 1961 Chapter 5.

2. Pruss D.: '**Applications of infrared waveguides in remote gas-spectroscopy**', Proceedings SPIE, 1987, New Materials for Optical Waveguides, Vol. 799, pp. 117-122

3. Ruddy V., McCabe S., MacCraith B. D.:'**Detection of Propane by IR-ATR in a Teflon-Clad Fluoride Optical Fibre**', Applied Spectroscopy, Vol. 44, No 9, 1990

4. McCabe S. MacCraith B. D.: '**Novel mid-IR LED as source for optical fibre evanescent wave gas detection**', Electronics Letters, 1993, Vol. 29, No. 19, pp. 1719-1720

5. Gloge D.:'**Weakly guiding fibres**', Applied Optics, 1971, Vol. 10, pp. 2252-2258

6. Digonnet M.J.F., Feth J.R., Stokes L.F., Shaw H.J.: '**Measurement of the core proximity in polished fiber substrates and couplers**', Optics Letters, 1985, Vol. 10, No. 9, pp. 463-5

7. Zafirova B.S., Panajotov K.P. Andreev A.TZ.: '**Temperature-stable polished fibre-optic coupler**', Optics and Laser Technology, 1992, Vol. 24, No. 6, pp. 345-7

8. Digonnet M.F.J., Shaw H.J.: '**Analysis of a tunable single mode optical fiber coupler**', IEE Transactions on Microwave Theory and Techniques, 1982, Vol. MTT-30, No. 4, pp. 592-600

9. Tai H., Tanaka H., Yoshino T.: '**Fiber-optic evanescent-wave methane-gas sensor using optical absorption for the 3.392-μm line of a He-Ne laser**', Optics Letters, 1987 Vol. 12, No. 6, pp. 437-9

10. 2-propanol, Aldrich Library of Infrared Spectra

11. Harrick N.J.: '**Internal Reflection Spectroscopy**', Harrick Scientific Corporation 1985 pp. 43-44

12. Falco L., Berthou H., cochet F., Scheja B., Parriaux O.: '**Temperature sensor using single mode evanescent field absorption**', Proceedings SPIE, 1985, Fibre Optic Sensors, Vol. 586, pp. 114-9

13. MacCraith B.D., Ruddy V., McCabe S.: '**Suitability of singlemode fluoride fibres for evanescent wave sensing**', Proceedings SPIE, 1991, Vol. 1587, pp. 310-317

14. Falco l. Specha G., Roth P., Parriaux O.: '**Non-ambiguous evanescent-wave fibre refractive index and temperature sensor**', Optica Acta 9186, Vol. 33, No. 12, pp. 1563-1570

15. Lew A., Depeursinge C., Cochet F., Berthou H., Parriaux O.: '**Single-mode fibre evanescent wave spectroscopy**', 2nd International Conference on Fibre Optic Sensors, Stuttgart, 1984, pp. 71-4

16. Vassalo C.: '**Optical waveguide concepts**', Elsevier 1991, Chapter 5.2

17. Unger H.G.: '**Planar Optical Waveguides and Fibres**', Clarendon Press, 1980, Chapter 6.3

18. Vassalo C.: '**Rigorous theory for modes of optical fibres with cladding limited by a plane**', Electronics Letters, 1986, Vol. 22, No. 18, pp. 944-945

19. Muhammad F.A., Stewart G.: '**D-shaped optical fibre design for methane gas sensing**', Electronics Letters, 1992, Vol. 28, No. 13, pp. 1205-6

20. Muhammad F.A., Stewart G.: '**Sensitivity enhancement of D-fibre methane gas sensor using high-index overlay**', IEE Proceedings-J, 1993, Vol. 140, No. 2, pp 115-118

21. Wykes S.J.: '**All fired up over fire detectors**', Physics World, August 1993, p. 20

22. Ruddy V., McCabe S.: '**Detection of Propane by IR-ATR in a Teflon-Clad Fluoride Glass Optical Fibre**', Applied Spectroscopy 1990, Vol. 44, no 9, pp.1461-3

23. Mailhot A.M., Elyamani A., Riman R.E.: '**Reactive atmosphere synthesis of sol-gel heavy metal fluoride glasses**', Journal Material Research, 1992, Vol. 7, No. 6, pp. 1534-1540

24. Snyder A.W., Love J.D.: '**Optical waveguide theory**', Chapman & Hall, 1991, p. 410

25. Rowe C.J., Moore M.W., Wilkinson I.J., Achurch N.E.: '**fused taper couplers in multimode fluorozirconate fibre**', Electronics Letters, 1990, Vol. 26, No. 5, pp. 316-8

26. O'Dwyer K.: '**Development of Infrared evanescent wave fibre sensors using an FTIR spectrometer**', 1993 Master of Science Thesis at Dublin City University.

27. Tai H., Tanaka H., Yoshino T.: '**Fiber-optic evanescent-wave methane-gas sensor using optical absorption for the 3.392 μm line of a HeNe laser**', Optics Letters, 1987, Vol. 12, No. 6, pp. 437-9

28. Black R.J., Gonthier F., Lacroix S., Lapierre J., Bures J.: '**Tapered fibers: an overview**', Proceedings SPIE 1987, Components for fiber optic applications, Vol. 839, pp. 2-19

29. Love J.D., Henry W.M., Stewart W.J., Black R.J., Lacroix S., Gonthier F.: '**Tapered single-mode fibres and devices Part 1: Adiabaticity criterion**', IEE Proceedings-J, 1991, Vol. 138, No. 5, pp. 343-354

30. Burns W.K., Abebe M., Villarruel C.A.: '**Parabolic model for shape of fiber taper**', Applied Optics, 1985, Vol. 24, No. 17, pp. 2753-5

31. table 12-5, from reference 24, p. 256

32. Driver R.D., Leskowitz G.M., Curtiss L.E.: '**Applications of IR transmitting optical fiber in the chemical industry**', Prcoeedings SPIE, 1989, Infrared Fibre Optics II, Vol. 1228, pp. 233-245

33. Heo J., Rodrigues M., Saggase S.J., Sigel G.H., '**Remote fiber-optic chemical sensing using evanescent-wave interactions in chalcogenide glass fibers**', Applied Optics, 1991, Vol. 30, No. 27, pp 3944-3951

34. Katz M., Bornstein A., Schnitzer I, Katzir A.: '**Evanescent wave spectroscopy using chalcogenide glass fiber: theoretical analysis and experiments**', Proceedings SPIE OE Fibres, 1991, Infrared Fiber Optics III, Vol 1591, pp. 236-245

35. Brandrup J.,Immergut E.H.: '**Physical constants of Poly(Tetrafluoroethylene)**', Polymer Handbook 2nd ed., 1975, Wiley & Sons, pp. V29-V36

36. Cullis C.F., Firth J.G.: '**Detection and measurement of hazardous gases**', Science reviews Ltd, 1981, p56, Table 2.6

37. Crank C.: '**The mathematics of Diffusion**', Clarendon Press 1975, p. 73, eqn. 5.24

38. Brandrup J., Immergut E.H.: '**Polymer Handbook**' Wiley and Sons, 1975, Vol. III, p. 236

39. Lee D.L.: '**Electromagnetic principles of integrated optics**', Wiley& Sons, 1986, chapter 3.

40. Zotova N.V., Karandashov S.A., Matveev B.A., Pentsov A.V., Slobodchikov S.V., Smirnova N.N., Stus N.M., Talalakin G.N., Markov I.I.: '**Optoelectronic sensors based on narrow band A^3B^5 alloys**', Proceedings SPIE 1991, Chemical, Biochemical and Environmental Sensors III, Vol. 1587, pp. 334-345

41. Dobbelaere W., de Boeck J., Bruynseraede C., Mertens R., Borghs G.: '**InAsSb light emitting diodes and their applications to infra-red gas sensors**', Electronics Letters, 1993, Vol. 29, No. 10, pp. 890-1

42. Aidaraliev M., Zotova N.V., Karandashev S.A., Matveev B.A., Stus N.M., Talalakin G.N.: '**Low-threshold long wave lasers (λ=3.0-3.6 μm) based on III-V alloys**', Semiconductor Science and Technology, 1993, Vol. 8, No. 8, pp. 1575-1580

43. Baranov A.N., Danilova T.N., Ershov O.G., Imenkov A.N., Sherstnev V.V., Yakovelv Yu.P.: '**Long wavelength InAsSb/InAsSP lasers for the spectroscopty of methane (λ = 3.2-3.4 μm)**', Soviet Technical Physics Letters, 1992, Vol. 18, No. 11, pp. 725-6

Chapter 7 Conclusion

In this work the evanescent wave sensitivity of a number of types of single-mode and multi-mode optical fibre structures have been investigated for mid-IR flammable gas sensing using zirconium fluoride optical fibres. Experimental results and theoretical models are presented for side-polished, tapered and porous clad fibres and their merits for evanescent wave sensing discussed. In addition, a novel solid state room temperature operating source has been evaluated for use with infrared transmitting optical fibre. Evanescent wave sensing of flammable gases has been demonstrated using this source with multimode Teflon clad fibre.

The sensitivity of side-polised fibre to gases was found to be limited due to confinement of the modal field by the asymmetric refractive index discontinuity inherent in the sensor structure. The use of porous overlayers has been proposed to overcome this problem. The ideal material for such a porous layer is a microporous fluoride sol-gel glass. Such a coating would enhance sensitivity shown while maintaining the low-loss characteristics of fluoride fibres in the mid-infrared. The loss induced in side-polished single-mode fibre as a function of the remaining cladding layer thickness exhibited oscillations. These were not predicted by theory and an explanation remains to be found.

The tapering of fluoride fibres was investigated and tapers were fabricated using a stepper motor and resistive wire heater taper pulling rig. However, these tapers did not have the required dimensions for gas sensing as they were not of a sufficiently small diameter in the taper waist region. The difficulty in attaining these criteria is due to the thermal and mechanical properties of fluoride glass. The parameters for an adiabatic taper with a commercially viable sensitivity were calculated from waveguide theory.

This calculation showed that the pulled tapers did not meet these criteria and further development of the tapering technique is necessary. The calculations indicate the potential sensitivity of fluoride optical fibre tapers to gaseous analytes.

Multimode Teflon-clad fluoride fibre was used in evanescent mode to detect flammable gas with an extrapolated limit of detection of better than 1% propane in air per meter of active sensor. The Teflon cladding has a porosity of approximately 42%. The potential of the porous cladding technique is demonstrated by the sensitivity achieved with this fibre. The sensitivity is calculated to be at least 5 times greater than the equivalent unclad fibre based on this porosity measurement. In addition to enhancing the sensitivity, a porous cladding can also act as a barrier to larger molecules that may foul the sensor.

Evanescent wave gas sensing using fluoride fibre has been investigated thoroughly and a practical sensor configuration demonstrated. Wider acceptance of this technique for gas sensing requires new materials and optical sources. Both of these may be available soon in the form of fluoride sol-gel glass and mid-IR laser diodes. The prospect of mid-IR laser diodes is very exciting for the development of distributed evanescent wave sensors which is the goal of much of the research into optical fibre based evanescent wave sensing.

List of Publications & Conference Presentations

1. McCabe S., MacCraith B.D.: '**Novel mid-IR LED as source for optical fibre evanescent wave gas detection**', Electronics Letters, 1993, Vol. 29, No. 19, pp.1719-1720
2. Ruddy V., McCabe S., MacCraith B.D.: '**Detection of Propane by IR-ATR in a Teflon-clad Fluoride Optical Fibre**', Applied Spectroscopy, 1990, Vol. 44, No. 9, pp. 1461-1463
3. MacCraith B.D., Ruddy V., McCabe S.: '**Suitability of single mode fluoride fibres for evanescent wave sensing**', Proceedings SPIE, 1991, Chemical, Biochemical and Environmental Fibre Sensors, Vol. 1587, pp 310-317
4. MacCraith B.D., Ruddy V., McCabe S.: '**Evanescent wave sensing using fluoride optical fibres**', Applied Optics and Opto-Electronics, Sept. 1990, Nottingham.
5. McCabe S.: '**Gas sensing using Infra-red Optical Fibres**', IOG-90, Third annual meeting, June 1990, Dublin City University
6. Farrell D., O'Dwyer K., McCabe S., MacCraith B.D., Ruddy V.: '**Sensing of chemical species using evanescent wave interactions on FTIR coupled infra-red transmitting optical fibres**', IOG-92, April 1992, University College Dublin.

APPENDIX A

A.1 Details of planar waveguide software.

Equation 3.16 reproduced below as A.1 shows the fundamental relationship between the amplitude coefficients of two adjoining layers.

$$\begin{pmatrix} 1 & 1 \\ -p_{j+1} & p_{j+1} \end{pmatrix}\begin{pmatrix} A_{j+1} \\ B_{j+1} \end{pmatrix} = \begin{pmatrix} e^{-p_j d_j} & e^{p_j d_j} \\ -p_j e^{-p_j d_j} & p_j e^{p_j d_j} \end{pmatrix}\begin{pmatrix} A_j \\ B_j \end{pmatrix} \qquad \text{A.1}$$

Expanding A.1 to relate the substrate (j = 0) and superstrate (j = n) coefficients gives

$$\begin{pmatrix} 1 & 1 \\ -p_n & p_n \end{pmatrix}\begin{pmatrix} A_n \\ B_n \end{pmatrix} = \overbrace{\begin{pmatrix} e^{-p_{n-1} d_{n-1}} & e^{p_{n-1} d_{n-1}} \\ -p_{n-1} e^{-p_{n-1} d_{n-1}} & p_{n-1} e^{p_{n-1} d_{n-1}} \end{pmatrix}\begin{pmatrix} \frac{1}{2} & -\frac{1}{p_{n-1}} \\ \frac{1}{2} & \frac{1}{p_{n-1}} \end{pmatrix}}^{M_{n-1}} M_{n-2} \cdots$$

$$\cdots M_1 \overbrace{\begin{pmatrix} \frac{1}{2} & -\frac{1}{p_o} \\ \frac{1}{2} & \frac{1}{p_o} \end{pmatrix}}^{M_o}\begin{pmatrix} A_o \\ B_o \end{pmatrix} \qquad \text{A.2}$$

M_1 to M_{n-1} may be simplified to

$$\begin{pmatrix} \cosh(p_j d_j) & \sinh(p_j d_j) \\ p_j \sinh(p_j d_j) & \frac{1}{p_j}\cosh(p_j d_j) \end{pmatrix} \qquad \text{A.3}$$

A.1.1 Program flow chart.

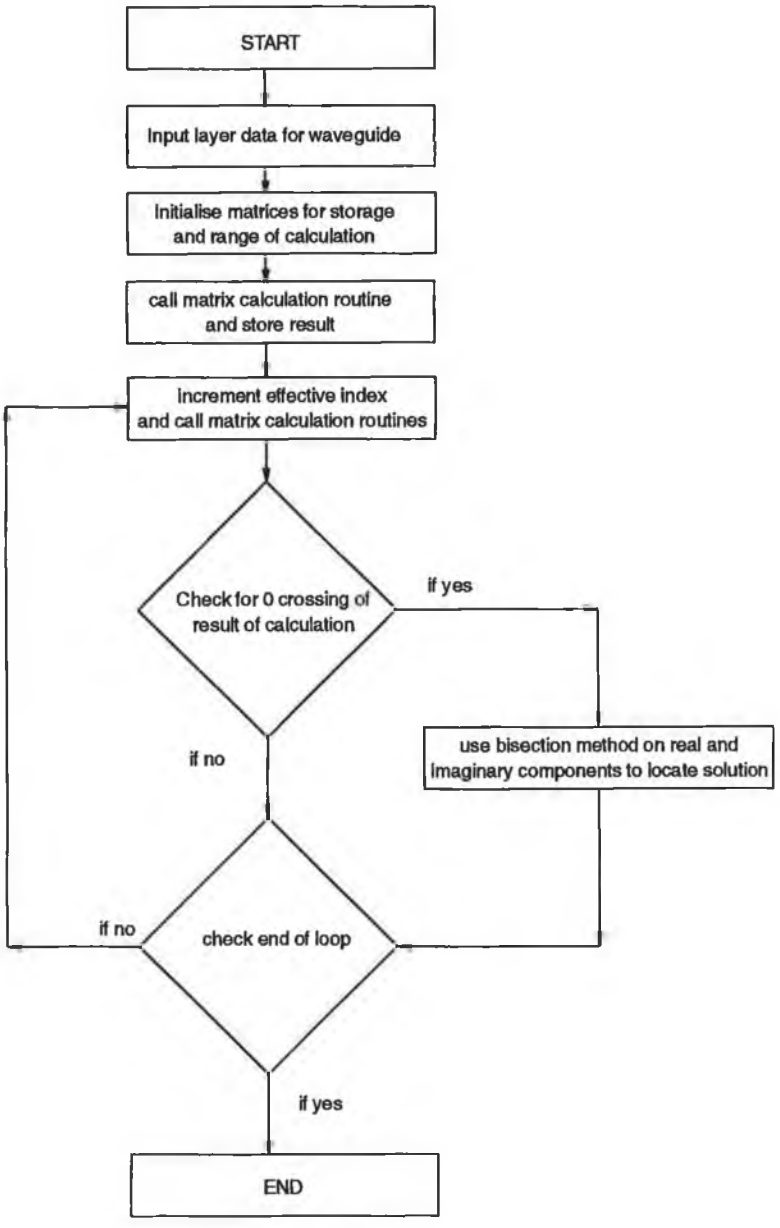

A.2 D-shape & finite clad fibre software.

The routines used for the bessel functions in these programs are from reference 1. For the integer order functions simple polynomial expansions are used. To calculate the derivatives the recurrence relations are used.

$J_o(x)$	equations 9.4.1 & 9.4.3
$J_1(x)$	equations 9.4.4 & 9.4.6
$I_o(x)$	equations 9.8.1 & 9.8.2
$I_1(x)$	equations 9.8.3 & 9.8.4
$K_o(x)$	equations 9.8.5 & 9.8.6
$K_1(x)$	equations 9.8.7 & 9.8.8
$J'(x)$	equations 9.1.27
$I'(x)$ & $K'(x)$	equations 9.6.26

The matrix determinant routine for the D-shaped program is taken from reference 2 and uses the routine LUDDCMP.C. The matrix determinant for the weakly guided model is calculated explicitly. The matrix determinant for the finite clad fibre is taken from Unger (see Appendix B).

1. M. Abramowitz, J. A. Stegun.: 'Handbook of Mathematical Functions', National Bureau of Standards.

2. 'Numerical Recipes in C': Mathematical library.

APPENDIX B

B.1 Characteristic equation for finitely clad fibre from Unger.

$$\left(Z_1^{(H)}+Z_2^{(H)}\right)\left(n_1^2 Z_1^{(E)}+n_2^2 Z_2^{(E)}\right)=$$

$$m^2N^2\left\{\frac{Z_1^{(H)}Z_1^{(E)}}{\left(u^2B\,Y_m\right)^2}+\frac{W_o^2}{(n_2vcB_3W_1)^2}\left[\left(Y_m+\frac{W_2}{vW_o}\right)\left(n_1^2Y_m+n_2^2\frac{W_2}{vW_o}\right)-\left(\frac{mN}{(u^2B)}\right)^2\right]-\frac{2}{B\,B_3(ucv^2W_1)^2}\right\}$$

where

$$Z_1^{(H)}=Y_m\left(1+vcU_m\frac{W_o}{W_1}\right)$$

$$Z_1^{(E)}=Y_m\left[1+\left(\frac{n_3}{n_2}\right)^2vcU_m\frac{W_o}{W_1}\right]$$

$$Z_1^{(H)}=\left(cU_mW_2-\frac{W_3}{v}\right)W_1$$

$$Z_2^{(E)}=\left[\left(\frac{n_3}{n_2}\right)^2cU_mW_2-\frac{W_3}{v}\right]/W_1$$

$$W_o=I_m(vc)K_m(v)-I_m(v)K_m(vc)$$

$$W_1=I_m(v)K_m'(vc)-I_m'(vc)K_m(v)$$

$$W_2=I_m(vc)K_m'(v)-I_m'(v)Km(vc)$$

$$W_3=I_m'(vc)K_m'(v)-I_m'(v)k_m'(vc)$$

$$Y_m=\frac{J_m'(u)}{uJ_m(u)}\qquad;\qquad U_m=\frac{K_m'(wc)}{wcK_m(wc)}$$

$$B = \frac{\left(\frac{\beta}{k_o}\right)^2 - n_2^2}{n_1^2 - n_2^2} \quad ; \quad B_3 = \frac{\left(\frac{\beta}{k_o}\right)^2 - n_3^2}{n_2^2 - n_3^2}$$

$$u = a\left(n_1^2 k_o^2 - \beta^2\right)^{1/2}$$

$$v = a\left(\beta^2 - n_2^2 k_o^2\right)^{1/2}$$

$$w = a\left(\beta^2 - n_3^2 k_o^2\right)^{1/2}$$

B.2 Characteristic equation for infinitely clad fibre

$$(Y_m + X_m)\left(n_1^2 Y_m + n_2^2 X_m\right) = \frac{m^2 N^2}{(u^2 B^2)^2}$$

where

$$X_m = \frac{K_m'(v)}{vK_m(v)}$$

and all other parameters are defined in B.1.

APPENDIX C

C.1 Zirconium Fluoride Glass fibre information

Data supplied by Le Verre Fluore	
Wavelength (μm)	Refractive index
1.0	1.51524
1.2	1.51365
1.4	1.51236
1.6	1.51116
1.8	1.50998
2.0	1.50877
2.5	1.50544
3.0	1.50154
3.6	1.49594
3.8	1.49385
4.0	1.49162
Measured @ 20°C	

Table C.1 refractive index vs wavelength for fluoride

Refractive index of ZBGA Fluoride glass	
Wavelength (μm)	Refractive index
3.23890	1.49384
3.30360	1.49347
3.41150	1.49204
3.41990	1.49211
3.55240	1.49081
Journal Lightwave Tech., Vol. 7, No. 8 [3]	

Table C.2 refractive index vs wavelength for fluoride

C.1.1 Sample Data from 11/125 μ m fibre supplied by Le Verre Fluore.

- Fibre Type IR GUIDE SM 11-125
- Core / clad material ZFG
- Coating material Polyacrylate
- Coating diameter 250 μm
- Attenuation [1 - 4.2 μm] < 1dB/m
- NA 0.15
- λ_c 2.22 μm

C.1.2 Calculated and inferred parameters

Fibre V number @ 3.392 μm = 1.5

Using the refractive index quoted by Le Verre Fluore as the core index at 3μm (≅ 1.5) and using the quoted NA gives a cladding index of approximately 1.493. These values are used in calculations in the body of the thesis for fibres with a quoted NA of 0.15.

Where an NA of 0.12 was quoted for a fibre the core and cladding indices used are 1.495 and 1.49 respectively. This was predominantly the case for early batches used in side-polishing experiments.

APPENDIX D

D.1 Sample of software: IR LED Data collection[4] (LED.PRJ)

D.1.1 header files

GPRINTF.H // graphics version of printf() function (taken from bgidemo program)

```
int gprintf( int *xloc, int *yloc, char *fmt, ... );
```

GGETS.H // graphics version of gets() function.

```
int ggets(int, int, int, char *);
```

LED.H // grouped header for LED.C, FILES.C, SCREEN.C,, POLL.C

```
#define AVERAGE 1
#define SCAN 0
#define MONITOR 1
#define NOT_DEFINED -1

#include <dir.h>
#include <stdio.h>
#include <time.h>
typedef struct {    char filename[MAXPATH];
                    char dir[MAXDIR];
                    char f_status;
                    FILE *f_ptr;
                    double position[3];
                    double scan_data[3];
                    double signal[2];
                    time_t time_data[3];
                    int averaging[3];
                    char choice;
          } ctrl;

int mouse_menu(int *);
void interrupted(ctrl *);
void monitor(ctrl *);
void scan(ctrl *control);

#define START_WAVELENGTH        control->scan_data[0]
#define END_WAVELENGTH          control->scan_data[1]
#define SCAN_STEP_SIZE          control->scan_data[2]
#define DATAFILENAME            control->filename
#define DATADIR                 control->dir
#define CURRENT_POSITION        control->position[0]
#define NEW_WAVELENGTH          control->position[1]
#define OLD_WAVELENGTH          control->position[2]
#define SIGNAL                  control->signal[0]
#define SIGNAL_DISPLAY          control->signal[1]
#define MONITOR_WAVELENGTH      control->scan_data[0]
#define SCAN_TIME               control->scan_data[1]
#define NUMBER_SAMPLES          control->averaging[0]
#define DELAY                   control->scan_data[2]
#define START_TIME              control->time_data[0]
#define END_TIME                control->time_data[1]
#define CURRENT_TIME            control->time_data[2]
#define FILE_POINTER            control->f_ptr
#define FILE_STATUS             control->f_status
#define CHOICE                  control->choice

/* for files.c */
void file_setup(ctrl *);
```

[4] Programs written and compiled in the Turboc Ver 2.0 IDE. TCC & TASM were used to compile SMOUSE.C to an object file for linking under the IDE.

```
int exists(ctrl *);
void increment(char *);
void open_file(ctrl *);
void close_file(ctrl *);

/* for screen.c */
void open_screen_display(void);
int status_choice(int,int);
typedef  struct {   int limits[2];
                    int graph_limits[4];
                    int graph_box[4];
                    int colours[6];
                    int text[4];
                    int menu[4];
        } disply;

#define MAXX                display->limits[0]
#define MAXY                display->limits[1]
#define LEFTX               display->graph_limits[0]
#define RIGHTX              display->graph_limits[1]
#define BOTTOMY             display->graph_limits[2]
#define TOPY                display->graph_limits[3]
#define BACKGND             display->colours[0]
#define GRAPH               display->colours[1]
#define MENU                display->colours[2]
#define STATUS              display->colours[3]
#define TEXT                display->colours[4]
#define TITLE               display->colours[5]
#define TEXTHEIGHT          display->text[0]
#define TEXTWIDTH           display->text[1]
#define TEXTBOX             display->text[2]
#define MENULEFT            display->menu[0]
#define MENUTOP             display->menu[1]
#define MENUWIDTH           display->menu[2]
#define MENUSIZE            display->menu[3]
#define LEFT                display->graph_box[0]
#define TOP                 display->graph_box[1]
#define  HEIGHT             display->graph_box[2]
#define WIDTH               display->graph_box[3]
#define SETTINGS_POS 24

void data_area_setup(ctrl *);
void plot(ctrl *);
void terminate_screen(void);
void display_filename(ctrl *);

/* for smouse.c from smouse.h  */
int  mouseinit(void);
void mouseon(void);
void display_mouse(void);
void hide_mouse(void);
void mouseshape(int);
void mousemaxmin(disply *);
void mousesetpos(int,int);
int readcharacter(void);
int mousebutton(int);
void mousebuttoninfo(int *,int *,int *);

 /*  gedit.h  */
#define ON 1
#define OFF -1
int   gedit(int, int, char *, int, int, int, int);

 /*  adc.h  */
#define BASE        800
#define COUNTER0    0     /*8253 counter timer*/
#define COUNTER1    1
#define COUNTER2    2
#define CTRL8253    3
#define ENABLE      3
#define PORTA       4     /*8255 input output ports*/
#define PORTB       5
#define PORTC       6
#define CTRL8255    7
#define DISABLE     7
#define DACALSB     8     /*7801 digital to analog converter*/
#define DACAMSB     9
#define DACBLSB     10
#define DACBMSB     11
#define LOADDAC     12
#define a12bit      16    /*574 analog to digital converter*/
#define a8bit       17
#define ADCMSB      18
#define ADCLSN      19
#define TESTEOC     20
#define CHANSEL     24
#define BUSY        1           /*analog to digital EOC status value*/
#define EOC         0
float poll(ctrl *);
float get_data(void);

 /*  stepper.h  */
#define LPT_STAT    union l_s
#define LPT_PINS    union l_p
#define SEND        0
#define INIT        1
```

```
#define PSTAT       2
#define LPT1        0
#define CALIB       -1
#define NORM        0
#define FULL        0
#define HALF        1
#define FORWARD     1
#define REVERSE     0
#define SLOW        300
#define FAST        5
#define MEDIUM      150
#define FULL_HALF   0x01
#define DIRECTION   0x04
#define MOTOR_CLK 0x02
#define END_STOP    0x 2 / biosprint out of paper line */

int         stepper(int, int, int, unsigned);
double      goto_wavelength(ctrl *,double, char);
double      find_zero(ctrl *);
```

D.1.2 program files

LED.C // main menu program including wavelength scan and monitor programs

```
#include <stdio.h>
#include <stdlib.h>
#include <conio.h>
#include <ctype.h>
#include <time.h>
#include <dir.h>
#include <string.h>
#include <dos.h>
#include <math.h>
#include <process.h>
#include <graphics.h>
#include "led.h"

void    main(void)   {
    char temp[50];
    int y;
    ctrl *control;

    control = (ctrl *)malloc(sizeof(ctrl));
    CHOICE = NOT_DEFINED;
    START_WAVELENGTH = NOT_DEFINED;
    END_WAVELENGTH = NOT_DEFINED;
    SCAN_STEP_SIZE = NOT_DEFINED;
    SIGNAL_DISPLAY = 1;
    NUMBER_SAMPLES = 20;

    open_screen_display();
    file_setup(control);
    do{
    switch (mouse_menu(&y)) {
        case 27:
        case 'Q': terminate_screen();
                  exit(0);
                  break;
        case 0:   if (CHOICE == NOT_DEFINED) break;
                  itoa(START_WAVELENGTH,temp,10);
                  hide_mouse();
                  gedit(160,y,temp,10,10,EGA_BLACK,EGA_WHITE);
                  display_mouse();
                  START_WAVELENGTH = atoi(temp);
                  break;
        case 1:  if (CHOICE == NOT_DEFINED) break;
                  itoa(END_WAVELENGTH,temp,10);
                  hide_mouse();
                  gedit(160,y,temp,10,10,EGA_BLACK,EGA_WHITE);
                  display_mouse();
                  END_WAVELENGTH = atoi(temp);
                  break;
        case 2:  if (CHOICE == NOT_DEFINED) break;
                  itoa(SCAN_STEP_SIZE,temp,10);
                  hide_mouse();
                  gedit(160,y,temp,10,10,EGA_BLACK,EGA_WHITE);
                  display_mouse();
                  SCAN_STEP_SIZE = atol(temp);
                  break;
        case 3:
                  break;
        case 4:  itoa(NUMBER_SAMPLES,temp,10);
                  hide_mouse();
                  gedit(160,y,temp,10,10,EGA_BLACK,EGA_WHITE);
                  display_mouse();
                  NUMBER_SAMPLES = atoi(temp);
                  break;
        case 5:  sprintf(temp,"%f",SIGNAL_DISPLAY);
                  hide_mouse();
                  gedit(160,y,temp,10,10,EGA_BLACK,EGA_WHITE);
```

```
                display_mouse();
                SIGNAL_DISPLAY = atof(temp);
                break;
        case 6:
                break;
        case 7:  if (CHOICE == NOT_DEFINED || START_WAVELENGTH == NOT_DEFINED ||
                    END_WAVELENGTH == NOT_DEFINED || SCAN_STEP_SIZE ==NOT_DEFINED)
                break;
                data_area_setup(control);
                if (CHOICE == SCAN) scan(control);
                else if (CHOICE == MONITOR) monitor(control);
                break;
        case 8:
                break;
        case 9:         CHOICE = status_choice(2,0);
                break;
    }
    } while (1);
}

void interrupted(ctrl *control) {
    switch(toupper(getch())) {
    case 27:
    case 'Q': if (CHOICE ==SCAN) END_WAVELENGTH = CURRENT_POSITION;
                else SCAN_TIME = CURRENT_POSITION;
                break;
    case '+':  if (CHOICE == SCAN) break;
                CURRENT_POSITION = 0;
                break;
    default :  putch(7);
    }
}

void scan(ctrl *control) {
    open_file(control);
    fprintf(FILE_POINTER,"\\s%f\n\\e%f\n\\w%f\n",START_WAVELENGTH, END_WAVELENGTH,
                                                SCAN_STEP_SIZE);
    fputs("\\xWavelength (nm)\n\\yDetector signal (arb units)\n",FILE_POINTER);
    CURRENT_POSITION = goto_wavelength(control,0.0, CALIB);
    NEW_WAVELENGTH = START_WAVELENGTH;
    for (;NEW_WAVELENGTH <= END_WAVELENGTH; NEW_WAVELENGTH += SCAN_STEP_SIZE){
        CURRENT_POSITION = goto_wavelength(control,NEW_WAVELENGTH, NORM);
        SIGNAL = poll(control);
        fprintf(FILE_POINTER,"%f\n",SIGNAL);
        plot(control);
        if (kbhit()) interrupted(control);
    }
    close_file(control);
}

void monitor(ctrl *control) {
    open_file(control);
    fprintf(FILE_POINTER,"\\s0.0\n\\e%f\n\\w%f\n", SCAN_TIME, DELAY);
    fputs("\\xTime (s)\n\\yDetector signal (volts)\n",FILE_POINTER);
    if (MONITOR_WAVELENGTH > 0) {
        CURRENT_POSITION = goto_wavelength(control,0.0, CALIB);
        NEW_WAVELENGTH = MONITOR_WAVELENGTH;
        goto_wavelength(control,NEW_WAVELENGTH, NORM);
    }
    MONITOR_WAVELENGTH = 0.0;
    time(&START_TIME);
    do {
        CURRENT_POSITION = difftime(time(&CURRENT_TIME),START_TIME);
        SIGNAL = poll(control);
        fprintf(FILE_POINTER,"%f\t%f\n",CURRENT_POSITION,SIGNAL);
        plot(control);
        delay(DELAY);
        if (kbhit()) interrupted(control);
    } while(CURRENT_POSITION < SCAN_TIME);
    close_file(control);
}
```

FILES.C *// file handling routines, generates unique filename with date*

```
#include <stdio.h>
#include <stdlib.h>
#include <string.h>
#include <dir.h>
#include <dos.h>
#include <ctype.h>
#include <conio.h>
#include <math.h>
#include <time.h>
#include "led.h"
struct date today;

void file_setup(ctrl *control) {
    static    char drive[MAXDRIVE], file[MAXFILE], ext[MAXEXT];

    FILE_POINTER = NULL;
    strcpy(DATAFILENAME,"F:\\LED\\DATA\\UNTITLED.DAT");
```

```
    FILE_STATUS = NOT_DEFINED;
    getdate(&today);
    fnsplit(DATAFILENAME,drive,DATADIR,file,ext);
    file[0] = 48+today.da_day/10;
    file[1] = 48+(int)fmod((double)today.da_day,10.0);
    file[2] = 48+today.da_mon/10;
    file[3] = 48+(int)fmod((double)today.da_mon,10.0);
    file[4] = '9';   file[5] = '3';   file[6] = '0';   file[7] = '1';
    file[MAXFILE-1] = '\0';
    fnmerge(DATAFILENAME,drive,DATADIR,file,ext);
    while (exists(control)) {
        increment(file);
        fnmerge(DATAFILENAME,drive,DATADIR,file,ext);
    }
    display_filename(control);
}

int exists(ctrl *control) {
    struct ffblk ffblk;
    return(!findfirst(DATAFILENAME,&ffblk,0)); }
    void increment(char *filename) {
    if (filename[7] < 57) filename[7]++;
    else {
        filename[6]++;
        filename[7] = 48;
    }
}

void open_file(ctrl *control) {
    chardrive[MAXDRIVE], file[MAXFILE], ext[MAXEXT];

    fnsplit(DATAFILENAME,drive,DATADIR,file,ext);
    getdate(&today);
    while (today.da_day != atol(file)/1000000l) {
        file[1]++;
        if (file[1] > 48+9) {
            file[1] = '0';
            file[0]++;
        }
        if (atol(file)/1000000l > 31) {
            file[0] = '0';
            file[1] = '1';
        }
        file[6] = '0';
        file[7] = '1';
        fnmerge(DATAFILENAME,drive,DATADIR,file,ext);
    }
    while (exists(control)) {
        increment(file);
        fnmerge(DATAFILENAME,drive,DATADIR,file,ext);
    }

    display_filename(control);
    fnmerge(DATAFILENAME,drive,DATADIR,file,ext);
    FILE_POINTER = fopen(DATAFILENAME,"wt");
}

void close_file(ctrl *control) {
    fclose(FILE_POINTER);
    FILE_POINTER = NULL;
}
```

STEPPER.C // monochromator stepper motor drive software (uses LPT1)

```
#include <dos.h>
#include <bios.h>
#include <stdlib.h>
#include <stdio.h>
#include <math.h>
#include <conio.h>
#include "led.h"

double   goto_wavelength(ctrl *control,double new_wavelength, char calib)
{
    static double old_wavelength;
    int steps;
    if (calib == CALIB) new_wavelength = find_zero(control);
    else {
        steps = (new_wavelength-old_wavelength)*16;
        new_wavelength = old_wavelength + (double)steps/16;
        steps = stepper(steps, FORWARD, HALF, FAST);
    }
    old_wavelength = new_wavelength;
    return(new_wavelength);
}

int stepper(int n_steps, int dir, int full, unsigned dlay)  {
    int loop = 0, status;
    static union {
        struct    {    unsigned int full :1;
                       unsigned int clock :1;
                       unsigned int dirn :1;
```

```
                        unsigned int :5;
            }   op_pin;
            int op_pins;
        } p;
        p.op_pin.dirn = dir;
        p.op_pin.full = full;
        biosprint(SEND, p.op_pins, LPT1);

        for (; loop < 2*n_steps; loop++) {
            p.op_pin.clock ^= 0x01;
            status = biosprint(SEND, p.op_pins, LPT1);
            if (!(status & END_STOP)) break;
            delay(dlay);
        }
        return((loop-1)/2);
}

double find_zero(ctrl *control)  {
        double  max = 0, current;
        int  pos = 0, loop = 0;
        while (stepper(100, REVERSE, FULL, FAST) > 1);
        stepper(115, FORWARD, FULL, FAST);
        for (; loop < 9; loop++) {
            stepper(8, FORWARD, FULL, FAST);
            current = fabs(poll(control));
            gotoxy(2,20);
            if (current > max) {
                max = current;
                pos = loop;
            }
        }
        stepper(8*(loop - pos) , REVERSE, FULL, FAST);
        return(0.0);
}
```

SCREEN.C // graphics screen handling routines

```
#include <stdio.h>
#include <stdlib.h>
#include <graphics.h>
#include <string.h>
#include <conio.h>
#include <dir.h>
#include <dos.h>
#include <time.h>
#include <ctype.h>
#include "led.h"

dsply *display;

void open_screen_display(void) {
        int graphmode,graphdriver,loop;
        char *menu[] = {"scan Start","scan End","scan sTep","","Point average","siGnal","new Filename",
                        "staRt","Autoscale","Data type"};
        display = (dsply *)malloc(sizeof(dsply));
        detectgraph(&graphdriver,&graphmode);
        if (graphdriver == HERCMONO) registerbgidriver(Herc_driver);
        if (graphdriver == VGA) registerbgidriver(EGAVGA_driver);
        if (registerbgifont(triplex_font) < 0) exit(1);
        if (registerbgifont(gothic_font) < 0) exit(1);
        if (registerbgifont(sansserif_font) < 0) exit(1);
        if (registerbgifont(small_font) < 0) exit(1);
        initgraph(&graphdriver,&graphmode,"");
        mouseinit();
        display_mouse();

        MAXX   = getmaxx();
        MAXY   = getmaxy();
        BACKGND = LIGHTGRAY;
        STATUS  = MAGENTA;
        TITLE   = BLUE;
        MENU    = WHITE;
        GRAPH   = LIGHTRED;
        TEXT    = BLACK;
        TEXTHEIGHT = textheight("H")+4;
        TEXTWIDTH  = textwidth("H");
        TEXTBOX    = TEXTHEIGHT;
        MENUSIZE   = 10;
        MENULEFT   = 20;
        MENUTOP    = 5;
        MENUWIDTH  = 230;
        setbkcolor(BACKGND);
        setlinestyle(SOLID_LINE,0,NORM_WIDTH);
        setfillstyle(SOLID_FILL,TITLE);
        bar(0,0,MAXX,TEXTBOX);
        setlinestyle(SOLID_LINE,0,NORM_WIDTH);
        setfillstyle(SOLID_FILL,MENU);
        bar(0,TEXTBOX,MAXX,TEXTBOX*2);
        setfillstyle(SOLID_FILL,STATUS);
        bar(0,MAXY-TEXTBOX-2,MAXX,MAXY);
        setcolor(TEXT);
        outtextxy(230,2,"LED – [untitled]");
```

```
    outtextxy(100,TEXTHEIGHT+2,"FILE      MODE      DATA      QUIT     START");
    setcolor(DARKGRAY);
    setfillstyle(SOLID_FILL,WHITE);

    for (loop = MENUTOP;loop < MENUTOP+MENUSIZE;loop++) {
        bar3d(MENULEFT,TEXTBOX*loop-2,140,TEXTBOX*(loop+1)-2,0,0);
        bar3d(150,TEXTBOX*loop-2,MENUWIDTH+MENULEFT,TEXTBOX*(loop+1)-2,0,0);
        outtextxy(MENULEFT+5,TEXTBOX*loop,menu[loop-MENUTOP]);
    }
    mouseinit();
    display_mouse();
}

void data_area_setup(ctrl *control) {
    char xaxis[20];
    LEFT = 300;
    TOP = 100;
    HEIGHT = 300;
    WIDTH = 300;
    setcolor(DARKGRAY);
    setlinestyle(SOLID_LINE,0,THICK_WIDTH);
    setfillstyle(SOLID_FILL,EGA_WHITE);
    bar3d(LEFT-20,TOP-10,LEFT+WIDTH+10,TOP+HEIGHT+20,0,0);
    setcolor(EGA_RED);
    setlinestyle(SOLID_LINE,0,NORM_WIDTH);
    bar3d(LEFT,TOP,LEFT+WIDTH,TOP+HEIGHT,0,0);
    if (CHOICE == SCAN) strcpy(xaxis,"Wavelength (nm)");
        else strcpy(xaxis,"Time (s)");
    outtextxy(LEFT+(WIDTH-textwidth(xaxis))/2,TOP+HEIGHT+TEXTHEIGHT-2,xaxis);
    outtextxy(LEFT-8,TOP+HEIGHT+2,itoa(START_WAVELENGTH,xaxis,10));
    outtextxy(LEFT+WIDTH-16,TOP+HEIGHT+2,itoa(END_WAVELENGTH,xaxis,10));
    outtextxy(LEFT-16,TOP+HEIGHT-7,"0");
    outtextxy(LEFT-16,TOP-2,itoa(SIGNAL_DISPLAY,xaxis,10));
    settextstyle(DEFAULT_FONT,VERT_DIR,1);
    outtextxy(LEFT-TEXTHEIGHT/2,TOP+HEIGHT*.4,"Signal (Volts)");
    settextstyle(DEFAULT_FONT,HORIZ_DIR,1);
}

void plot(ctrl *control) {
    int xx,y;
    xx = LEFT+((CURRENT_POSITION-START_WAVELENGTH) /(END_WAVELENGTH - START_WAVELENGTH))
*(double)WIDTH;
    if (SIGNAL>SIGNAL_DISPLAY) y = TOP;
        else y = (TOP+HEIGHT)-(int)(SIGNAL/SIGNAL_DISPLAY*(double)HEIGHT);
    if (SIGNAL<0) y = TOP-HEIGHT;
    setcolor(EGA_RED);
    rectangle(xx-1,y+1,xx+1,y-1);
}

void terminate_screen(void) {
    hide_mouse();
    closegraph();
}

int mouse_menu(int *y) {
    int button,x,item;
    do {
        mousebuttoninfo(&button,&x,y);
    } while(!button && !kbhit());
    if (button == 2) return('Q');
    if (button == 1 && (x>20 && x<250) && (*y>MENUTOP*TEXTBOX && *y<(MENUTOP+MENUSIZE) *TEXTBOX)) {
        item = (*y-MENUTOP*TEXTHEIGHT)/TEXTHEIGHT;
        *y = (item+MENUTOP)*TEXTHEIGHT;
    }
    if (!button) {
        switch(toupper(getch())) {
            case 27:
            case 'Q': item='Q';break;
            case 'S': item=0; break;
            case 'E': item=1; break;
            case 'T': item=2; break;
            case 'P': item=4; break;
            case 'G': item=5; break;
            case 'F': item=6; break;
            case 'R': item=7; break;
            case 'A': item=8; break;
            case 'D': item=9; break;
        }
    *y = (item+MENUTOP)*TEXTHEIGHT;
    }
    return(item);
}

int status_choice(int n, int offset) {
    static char *choice[] = {"Scan","Monitor"};
    int button,x,y,item=0;
    setcolor(WHITE);
    outtextxy(20,MAXY-TEXTBOX,"CHOOSE ");
    for (x = offset; x < n; x++)
        outtextxy(100+100*x,MAXY-TEXTBOX,choice[x]);
    do {
        do {
            mousebuttoninfo(&button,&x,&y);
        } while(!button && !kbhit());
        if (button == 1 && (x>100 && x<100*(1+n)) && y>MAXY-TEXTBOX)
        item = x/100;
```

```
            if (lbutton) {
                switch (toupper(getch())) {
                    case 'S':item = 1;
                             break;
                    case 'M':item = 2;
                             break;
                }
            }
        } while (litem);

        hide_mouse();
        setfillstyle(SOLID_FILL,STATUS);
        bar(0,MAXY-TEXTBOX-2,MAXX,MAXY);
        display_mouse();
        if (offset == 0) {
            setcolor(DARKGRAY);
            setfillstyle(SOLID_FILL,WHITE);
            bar3d(150, TEXTBOX*(MENUTOP+9)-2, MENUWIDTH+MENULEFT, TEXTBOX* (MENUTOP+10)-2, 0,0);
            outtextxy(160,(MENUTOP+9)*TEXTHEIGHT,choice[item-1]);
        }
        return(item-1);
}

void display_filename(ctrl *control) {
        char temp[50];
        setcolor(WHITE);
        setlinestyle(SOLID_LINE,0,NORM_WIDTH);
        setfillstyle(SOLID_FILL,TITLE);
        bar(0,0,MAXX,TEXTBOX);
        sprintf(temp,"LED -- [%s]",DATAFILENAME);
        outtextxy((MAXX-textwidth(temp))/2,2,temp);
}
```

SMOUSE.C // mouse handling routines

```
/*  Mouse handling routines....using interrupt 33h     (note must install mouse to use)
    pass value in ax as below ;
    ax  0       :get mouse status and initialise
                :status returned in ax  0 => not installed  0ffffh=> otherwise
                :number of buttons returned in bx
        1       :show mouse cursor
        2       :hide mouse cursor
        3       :get mouse position and button status
                :xpos in cx
                :ypos in dx
                :buttons pressed returned in bx as follows
                :           left - 01b
                :           right- 10b
                :           both - 11b
        4       :put mouse at defined pos
                :           xpos - cx
                :           ypos - dx
        8       :set limits to mouse movements (vertical)
                :           min  - cx
                :           max  - dx
        9       :assign a shape to the mouse
                :     es - contains array data segment
                :     dx - segment offset to data
                :     bx - xpos hot spot
                :     cx - ypos hot spot
*/

#include <dos.h>
#include <math.h>
#include <bios.h>
#include "led.h"

void mousebuttoninfo(int *button, int *xpos, int *ypos) {
    _AX = 3;
    asm int 33h;
    asm mov ax,bx;
    *button=_AX;   /* 1 = left  2 = right 3 = both  */
    *xpos =_CX;
    *ypos =_DX;
}

int mousebutton(int button) {
    _AX = 6;
    _BX = button;
    asm int 33h;
    return(_AX);
}

void display_mouse(void)  {
    _AX = 1 ;
    asm int 33h; }
    int mouseinit(void) {
    _AX = 0;
    asm int 33h;
    return (_AX);
}
```

```
void hide_mouse(void) {
      _AX = 2 ;
      asm int 33h;
}

void mousemaxmin(dsply *display) {
      _AX = 7;
      _CX = 0;
      _DX = MAXX;
      asm int 33h;
      _AX = 8;
      _CX = 0;
      _DX = MAXY;
      asm int 33h;
}

void mouseshape(int type) {
static unsigned hand[32]={      0xF9ff,0xE1FF,0xE9FF,0xE9FF,    0xE9FF,0xE849,0xE800,0x8924,
0x0924,0x0986,0x0DFC,0x2FFC,
                                0x3FFC,0x3FFC,0x0000,0x8001,    0x0C00,0x1200,0x1200,0x1200,
0x1200,0x13B6,0x1249,0x7249,
                                0x9249,0x9001,0x9001,0x8001,    0x8001,0x8001,0x8001,0x7FFE     };
static unsigned check[32]={     0xFFF0,0xFFE0,0xFFC1,0xFF83,    0xFF07,0x060F,0x001F,0x8037,
0xC07F,0xE0FF,0xF1FF,0xFBFF,
                                0xFFFF,0xFFFF,0xFFFF,0xFFFF,    0x0003,0x0006,0x000C,0x0018,
0x0030,0x0060,0x70C0,0x3980,
                                0x1F00,0x0E00,0x0400,0x0000,    0x0000,0x0000,0x0000,0x0000     };
static unsigned larrow[32]={    0xFE3F,0xFC7F,0xF87F,0xF0FF,    0xE0FF,0xC000,0x8000,0x0000,
0x8000,0xC000,0xE0FF,0xF0FF,
                                0xF87F,0xFC7F,0xFF3F,0xFFFF,    0x0080,0x0100,0x0300,0x0600,
0x0E00,0x1C00,0x3FFF,0x7FFF,
                                0x3FFF,0x1C00,0x0E00,0x0600,    0x0300,0x0100,0x0080,0x0000     };
      unsigned far *ptr;
      hide_mouse();
      _AX = 9;
      _BX = 1;
      _CX = 1;
      if(type==1) ptr=hand;
      if(type==2) ptr=check;
      if(type==3) ptr=larrow;
      if(type==4) mouseinit();
      else {
            _ES = (unsigned)FP_SEG(ptr);
            _DX = (unsigned)FP_OFF(ptr);
            asm int 33h;
      }
      display_mouse();
      display_mouse();
}

void mousesetpos(int x, int y) {
      _AX = 4;
      _CX = x;
      _DX = y;
      asm int 33h;
}
```

POLL.C *// polls input from LED driver to start Analog to Digital conversion*

```
#include <stdio.h>
#include <stdlib.h>
#include <dos.h>
#include "led.h"

int status = EOC;

float poll(ctrl *control) {
      int loop,dely;
      float d=0.0,b=0.0;
      outportb(BASE+CTRL8255,155);
      outportb(BASE+CHANSEL,0);
      for (loop=0;loop<NUMBER_SAMPLES;loop++) {
            while ((inportb(BASE+PORTC) & 2));   /* simplist way to register correct transition without using interrupts */
            while (!(inportb(BASE+PORTC) & 2));
            for (dely=0;dely<=31;dely++);
            outportb(BASE+a12bit,0);
            d+=get_data();          /* get on signal */
            while (!(inportb(BASE+PORTC) & 2));
            while ((inportb(BASE+PORTC) & 2));
            for (dely=0;dely<=31;dely++);
            outportb(BASE+a12bit,0);
            b+=get_data();          /* get off signal (background) */
      }
      return((d-b)/(float)NUMBER_SAMPLES);
}

float get_data(void) {
      while ((inportb(BASE+TESTEOC) & 1) != 1);
      return( (inportb(BASE+ADCMSB)*16 + inportb(BASE+ADCLSN)/16)/409.6 -5);
}
```

APPENDIX E

E.1 High resolution spectra of gases referenced in the text.

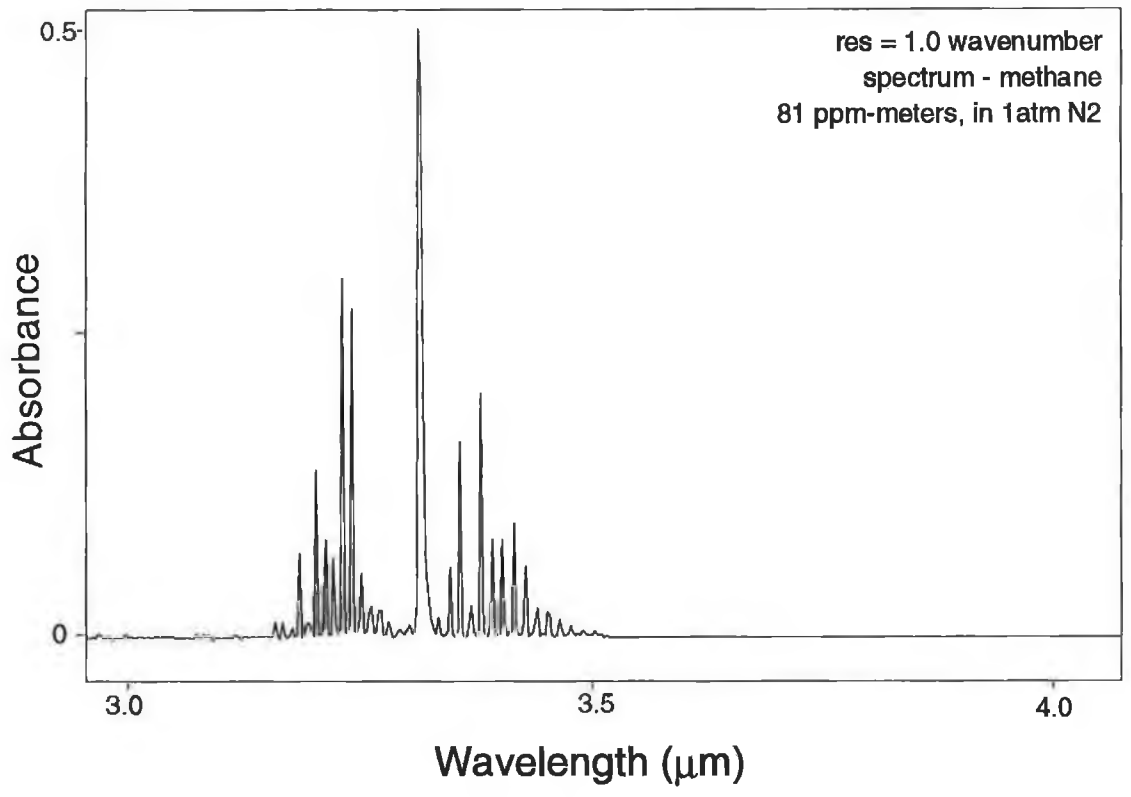

figure E.1 Spectrum of methane from 3-4 μm taken at 1cm^{-1} with Bomem MB120 FTIR

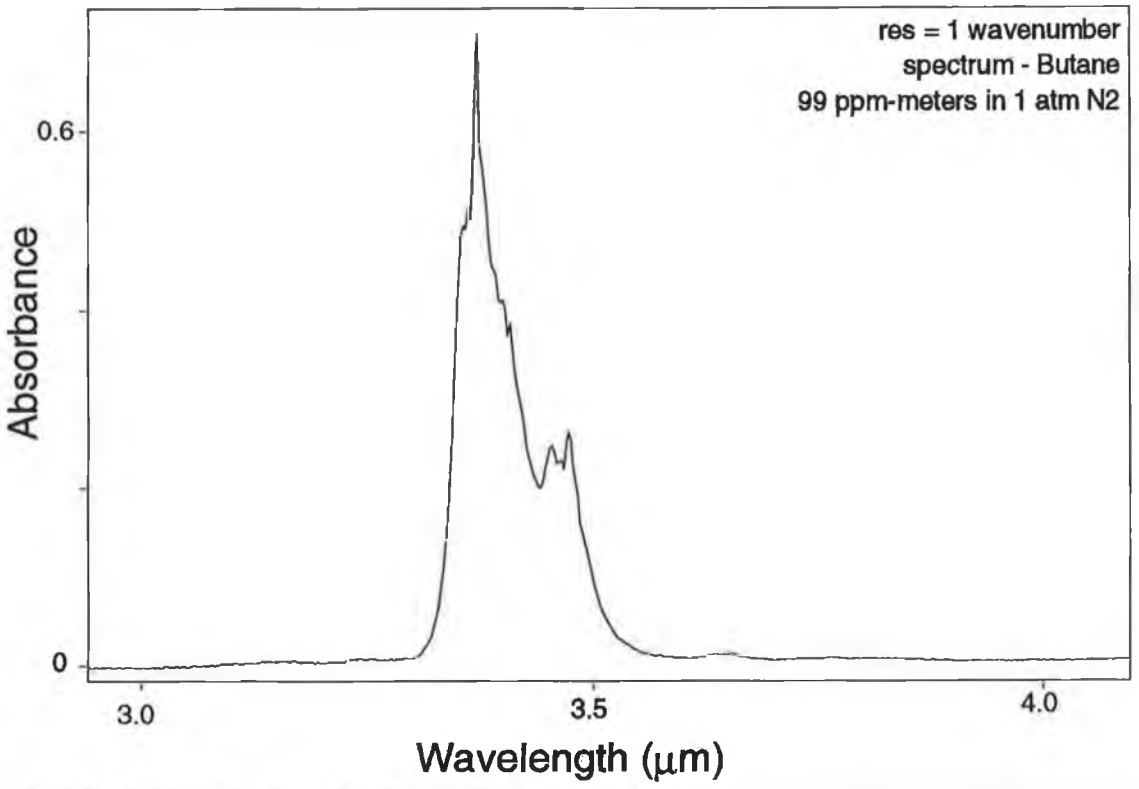

figure E.2 Spectrum of Butane from 3-4 μm taken at $1cm^{-1}$ resolution.

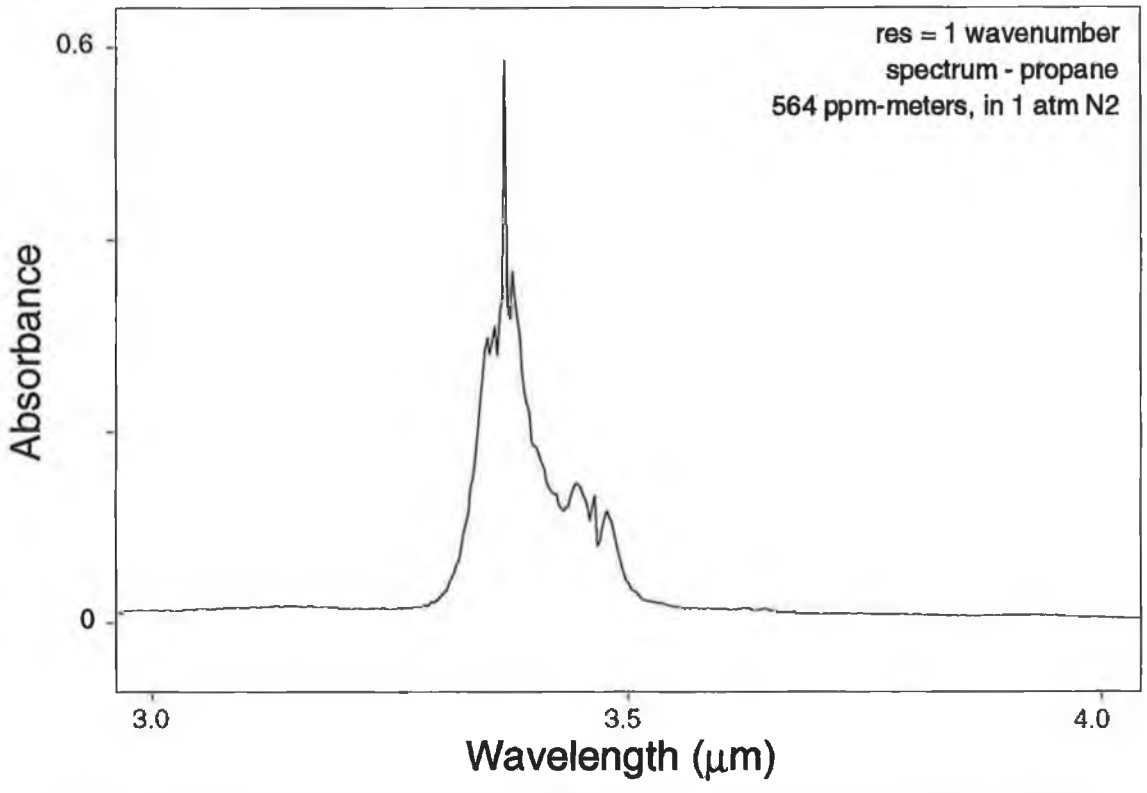

figure E.3 Spectrum of Propane from 3-4 μm taken at $1cm^{-1}$ resolution.

E.2 Miscellaneous spectra and data.

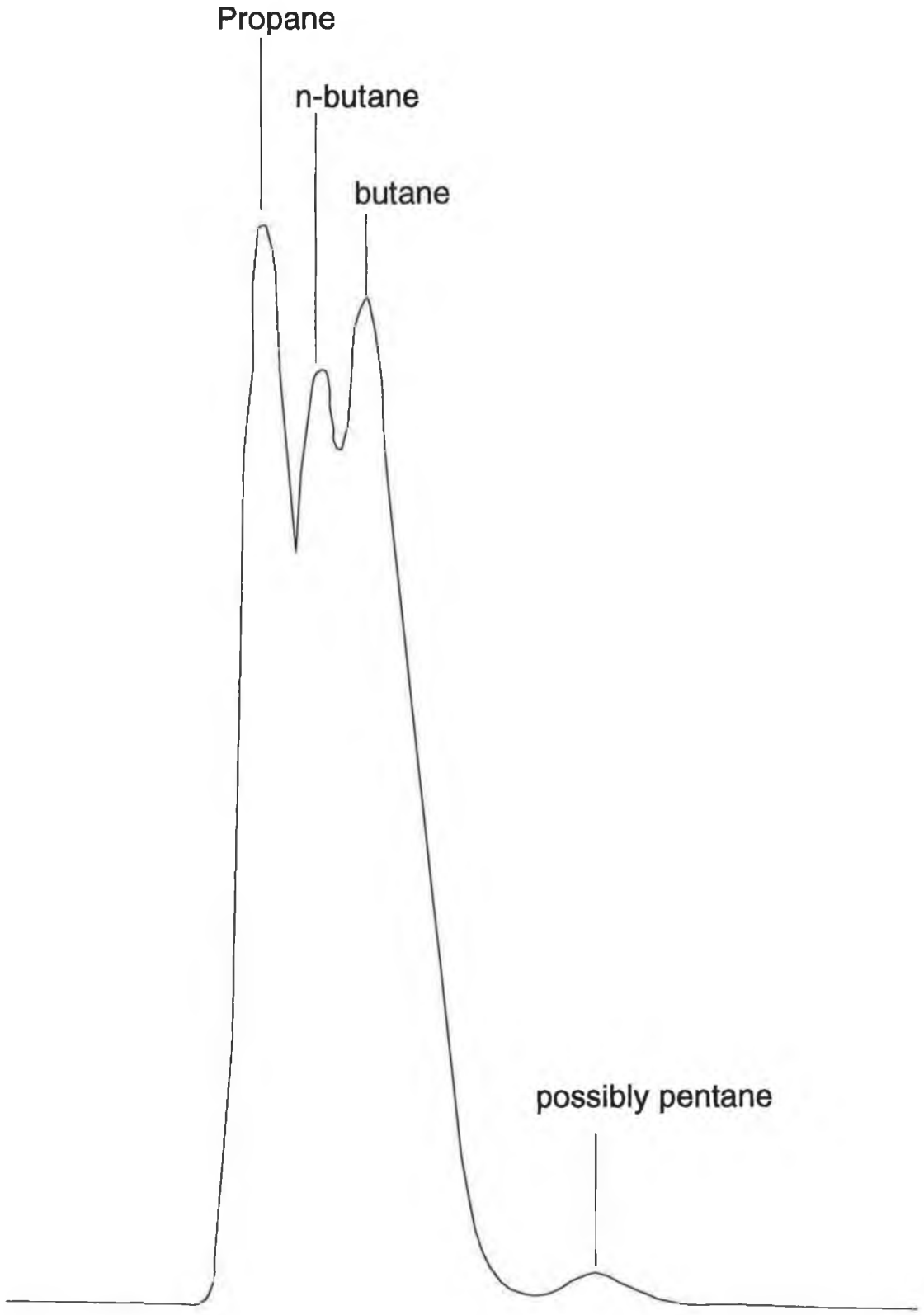

figure E.4 HPLC trace of the gas composition of the butane / propane gas cylinder used.